RARE MOLECULE BIOMARKER DETECTION USING DIELECTROPHORESIS SPECTROSCOPY

A Dissertation
Submitted to the Graduate Faculty
of the
North Dakota State University
of Agriculture and Applied Science

By

Fleming Dackson Gudagunti

In Partial Fulfillment of the Requirements
for the Degree of
DOCTOR OF PHILOSOPHY

Major Department:
Electrical and Computer Engineering

April 2021

Fargo, North Dakota

North Dakota State University
Graduate School

Title

RARE MOLECULE BIOMARKER DETECTION USING DIELECTROPHORESIS SPECTROSCOPY

By

Fleming Dackson Gudagunti

The Supervisory Committee certifies that this ***disquisition*** complies with North Dakota State University's regulations and meets the accepted standards for the degree of

DOCTOR OF PHILOSOPHY

SUPERVISORY COMMITTEE:

Dr. Ivan T. Lima Jr
Chair

Dr. David Anthony Rogers

Dr. Dharmakeerthi Nawarathna

Dr. Roberto Gomes

Approved:

April 12, 2021
Date

Dr. Benjamin D. Braaten
Department Chair

ABSTRACT

According to the American cancer society, 1.9 million new cancer cases and 608,570 cancer deaths are projected to occur in the United States. There is a fundamental technology gap that prevents the availability of tools for the diagnosis of cancer and genetic diseases as well as the genetic predisposition to developing certain diseases such as diabetes, and cardiovascular disease. The prognosis of several types of cancer can be done through blood tests to detect the concentration level of the respective biomarkers.

However, detecting biomarkers is still difficult with existing methods such as ELISA, Surface Plasmon resonance, and PCR techniques. The existing techniques have drawbacks due to complicated and time-consuming protocols, thus requiring the presence of an expert to handle complex and expensive pieces of equipment. Therefore, there is a need to develop a cost-effective transduction mechanism for biomarker detectors that could be used for cancer screening at the point-of-care preferably using as a single finger-prick blood droplet from the patients that have the combination of high sensitivity, high specificity, and low complexity to detect cancer at an early stage.

To address the limitations on the current techniques for biomarker detection, we developed a label-free automated real-time image processing technique based on dielectrophoresis (DEP) spectroscopy that is an effective transduction mechanism of a biosensor for the disease biomarker detection.

A substantial change in the negative DEP force applied to functionalized polystyrene microspheres (PM) was observed to both the concentration level of the disease biomarker and the frequency of the electric field produced by interdigitated gold microelectrode. The velocity of repulsion of the PM attached to the disease biomarker from the electrode was determined using a

side illumination and automated software using a real-time image processing technique that captures the Mie scattering from the PM. Since negative DEP spectroscopy is an effective transduction mechanism for the detection of the cutoff levels of disease biomarker, it has the potential to be used in the early-stage diagnosis and the prognosis of cancer.

ACKNOWLEDGMENTS

Thanks to Jesus, the merciful and the passionate, for providing me the opportunity to step into the excellent world of science.

Without the guidance of Dr. Ivan Lima, this work would not exist. I extend my gratitude for his wisdom and kindness as a professor and a mentor. I am thankful for his help in viewing difficult problems from every angle and to come up with novel solutions. He has taught me to understand the value of true learning and cross-functional communication. I thank Dr. Dharmakeerthi Nawarathna as he has shown immense generosity of his time and resources toward my projects.

I profusely thank my committee member Dr. David Rogers and Dr. Roberto Gomes for being integral parts of my committee and providing me with valuable suggestions, support, guidance, and goodwill.

I thank Dr. Benjamin Braaten for providing me an opportunity to serve the department as instructor of the courses ENGR 311 and ENGR 312.

I thank the Department of Electrical and Computer Engineering for providing me with financial support. I want to thank Laura D. Dallmann for taking care of all the little things and all the paperwork.

I would like to thank Jeffrey Erickson for his continuous technical support and inventory management throughout my Ph.D. studies. I would also like to acknowledge Gregory Strommen, Fredrick haring, and Dr.Gregory Cibuzar for fabricating the interdigitated electrode arrays that I used in my research.

I would like to recognize my colleagues Syed Abdul Mannan Kirmani, Logeeshan Velmanickam, Vidura Jayasooriya and Srilakshmi Gundlakunta for their interest and encouragement in my research.

My family has faithfully cared for me throughout my life. I am fortunate to know that I can always rely on my family especially my mother Rosebell Grace Prema. Thank you for encouraging me to strive for excellence in all that I do.

DEDICATION

To my smart and stunning wife, Vathsalya Moses, who selflessly serves others from a compassionate heart. You strengthen my motivation and sharpen my character. I have found greater worth in your companionship.

TABLE OF CONTENTS

LIST OF TABLES

LIST OF FIGURES

LIST OF ABBREVIATIONS

AC.....Alternating current

ADT .....Advanced dicing technologies

AFG.....Arbitrary function generators

ALD .....Atomic Layer Deposition

ANSI .....American National Standards Institute

APM.....avidin functionalized polystyrene microspheres

BSA.....Bovine serum albumin

CA.....Carbohydrate antigen

CAD .....Computer-aided design

CEA.....Carcinoembryonic antigen

CHX .....Cycloheximide

CM .....Center of mass

CMS .....Combinatorial Materials Science

CSV.....comma-separated values

CVI.....C for Virtual Instrumentation

DC.....Direct current

DEP .....Dielectrophoresis

DI .....Deionized water

DNA.....Deoxyribonucleic acid

EDTA.....Ethylenediaminetetraacetic acid

EGFR .....Estimated glomerular filtration rate

ELISA .....Enzyme-linked immunosorbent assay

FDA.....Food and Drug Administration

GAPDH.....Glyceraldehyde-3-Phosphate Dehydrogenase

GOS.....Glasgow Outcome Scale

HMDS.....Hexamethyldisilazane

HPRT.....Hypoxanthine-guanine phosphoribosyltransferase

IDE.....Integrated development environment

IVI.....Interchangeable Virtual Instruments Foundation

LED.....Light-emitting diode

MAQ.....Mapping and Assembly with Quality

MB.....Megabyte

MFC.....Microsoft Foundation Class Library

MOQ.....Minimum order quality

NDEPS.....Negative dielectrophoresis spectroscopy

PBS.....Phosphate-buffered saline

PC.....Personal computer

PCR.....Polymerase chain reaction

PIDE.....Pearl shaped interdigitated electrode

PM.....Polystyrene microspheres

RAM.....Random access memory

RFLP.....Restriction Fragment Length Polymorphism

RGB.....Red, green and blue

RNA.....Ribonucleic acid

SNP.....Single-nucleotide polymorphism

SOAP.....Short Oligonucleotide Analysis Package

SYBR.....Synergy Brands

TE.....Tris-EDTA

TERT.....Telomerase Reverse Transcriptase

TS.....Thymidylate synthase

USB.....Universal Serial Bus

UVC.....USB video class

VISA.....Virtual Instrument Software Architecture

WFNS.....World Federation of Neurosurgical Societies score

YES.....Yield engineering systems

1. INTRODUCTION

In 2020, 1.8 million new cancer cases and six hundred cancer deaths were projected to occur in the United States [1]. Early diagnosis of cancer is important as detecting symptomatic patients as early as possible will have the best chance for successful treatment [2], [3]. The early diagnosis of cancer can be performed from the saliva, serum, and blood sample of the patient [2], [4]. These cancer biomarkers can be used in the development of new precision medicine drugs, such as targeted therapy and immunotherapy, designed to target specific features in cancer cells, potentially reducing the damage to healthy cells [2], [4].

The term biomarkers refers to an indication of a biological state observed externally for a patient. Medical signs stand in contrast to medical symptoms, which are limited to those indications of health or illness perceived by patients themselves [5]–[9].

Researchers have defined the term biomarkers over the years in their literature with very little deviance. In 1998, the National Institutes of Health Biomarkers Definitions Working Group defined a biomarker as "a characteristic that is objectively measured and evaluated as an indicator of normal biological processes, pathogenic processes, or pharmacologic responses to a therapeutic intervention [10]–[14]."

Some of the biomarkers can be a protein, a specific enzyme, specific hormone concentration, an explicit gene distribution, or the concentration of a biological substance. These parameters are the initial set of indicators from the human body for its heath, physiological assessments such as disease diagnosis, effects of environmental exposures, etc. Thus, the biomarker can be used as a measurement of a parameter in the biological sample and then classify the patients accordingly. The first set of biomarkers whose measurements are recorded based on their physiological parameters of the patients using vitals such as blood pressure,

electrocardiograms, event monitoring, or stress test of the patient. The second set of biomarkers include the test results based on imaging techniques such as mammography, computed tomography scans, magnetic resonance imaging, or even X-ray measurements. The other set of biomarkers are the questionnaire-based clinical assessment. These objective assessments include the answers given by the patients to the questions asked by the nurse to the patient such as the World Federation of Neurosurgical Societies score (WFNS) [15] or Glasgow Outcome Scale (GOS)[16].

The third and effective set of biomarkers are those whose measurements are made from the protein concentration, gene transcripts in the biological fluids such as blood, urine, or tissue sample extracted from the patients.

The identification of the biomarkers is based on relevance and validity. Relevance refers to the ability to deliver clinically appropriate information and validity refers to its efficiency. Biomarkers can be used for patient evaluation in several medical scenarios, as well as approximating peril of disease, screening for occult primary cancers, distinguishing benign from malignant findings or one type of malignancy from another, determining prognosis and prediction for patients who have been diagnosed with cancer, and monitoring status of the disease, either to detect recurrence or determine response or progression to therapy [17], [18]. Determination of a patient's risk of developing malignancy is helpful if risk reduction strategies (such as lifestyle changes, prophylactic surgery, or chemoprevention) or screening are effective. Applying these strategies to high-risk groups is much more efficient than wholesale application to the entire population [6], [7]. Biomarkers have been identified that can be used to determine an individual's risk of developing cancer. Besides, this biomarker quantification technique needs to be simple and easy to perform in clinics, hospitals, and other point-of-care settings. Some of the biomarkers are found to occur in serum in remarkably stable forms, highlighting the significance of biomarkers

for early-phase cancer diagnostics and screening [14], [18]–[20]. Many biomarkers are FDA approved and it is essentially new and simple techniques are used to detect the same. To accomplish this need, we are proposing a low-cost, high throughput, high sensitive, and user-friendly lab-on-a-chip device technique to detect the biomarkers from serum in point-of-care settings.

1.1. Current State of the Art and Challenges

In our research we have studied two forms of biomarkers, namely:

- Protein-based biomarker
- Gene expression-based biomarkers.

1.1.1. Protein biomarker

Detection of biomarkers is important in the diagnosis and prognosis of life-threatening diseases like pancreatic ductal adenocarcinoma, acute myocardial infarction, lung cancer, prostate cancer, and oral cancer [9]. Unlike the conventional techniques, the biomarkers mostly are non-invasive techniques [21]. For example, pancreatic cancer is one of the most fatal forms of cancer malignancies in humans. The surgical procedure remains the only remedial action for this distressing ailment. The average five-year survival rate is 6% with less than one year of average survival time for the patients in the metastasis condition [22], [23]. Hence it is vital to diagnose this condition at its early stage. Biomarkers are one of the best methods in early diagnosis. The fluctuations of the levels of biochemical molecular biomarkers can be nucleic acids, peptides, carbohydrates, or proteins. Biomarkers act as an effective tool in the diagnosis and prognosis in comparison to other methods [7], [24], [25]. The biopsy is excruciating at times and has adverse effects on the body. The imaging techniques like magnetic resonance imaging, computed

tomography, ultrasound, and other optical imagining are not effective in diagnosing cancer at the early stages.

For example, carbohydrate antigen CA 19-9 is a protein biomarker that can be used in the detection of pancreatic cancer [25], [26]. CA 19-9 is currently the only biomarker that is approved by the U.S. Food and Drug Administration (FDA) for the monitoring of pancreatic cancer. A detailed literature review of pancreatic cancer was conducted by and they demonstrated various cutoff levels of CA 19-9 used as a screening tool in asymptomatic patients for the Diagnosis of Pancreatic Cancer. The predictive value of CA 19-9 in the diagnosis of pancreatic cancer rises with its increase in level. Steinberg et al. showed that the percentage of pancreatic cancer incidence level is 72% with CA 19-9 over 37 U/mL [27]. However, when the concentration of CA 19-9 exceeds 1000 U/mL, the probability of incidence of pancreatic cancer rises to more than 97%.

1.1.2. Gene expression-based biomarkers

Genetic markers are used to follow the inheritance patterns of chromosomal regions from generation to generation and are used in identifying the genetic variants associated with human disease [28]. The most common genetic variations are single nucleotide polymorphism (SNP), which is due to the differences in single base substitution. In every DNA sequence, SNP represents a difference in a single nucleotide [29]. SNP may replace a single nucleotide with another nucleotide [30]. Previous research has shown that SNP predicts an individual's risk of developing certain diseases such as cardiovascular disease, type 2 diabetes mellitus [31], autoimmune disease, Alzheimer's disease [32], cancer, and an individual's response to certain drugs [33]–[37]. These small differences can be used to track an individual's susceptibility to environmental factors such as toxins [38]. Since SNPs are stable over generations, they are excellent genetic markers. It is important to explore the role of SNPs in the genetic analysis of the disease as they would enable

the identification of complex diseases and genetic disorders [38]. Even though SNPs are an important factor in genetic variation [39], [40], detecting SNPs is still expensive and time-consuming with existing techniques.

In any living organism, messenger ribonucleic acid is a vital and functional constituent in the DNA present in cells. Messenger RNA (mRNA) serves as a sensitive biomarker in the prognosis and diagnosis of diseases as it holds a key connection between genome and proteome as it carries the information from the DNA to initiate the protein synthesis [41]. Some of the cell regulatory pathways are controlled by mRNA such as cell cycles, chromatin modifications, and cell adhesions, [42] and these regulatory pathways can be affected by different mRNA expression caused by activation mRNA degradation, point mutation, among others, leading to cause several diseases including cancer [41], [43], [44].

However, detecting protein and nucleotide-based biomarkers is still difficult with existing methods such as ELISA, Surface Plasmon resonance, and PCR techniques. The existing techniques have drawbacks due to complicated and time-consuming protocols, thus requiring the presence of an expert to handle complex and expensive pieces of equipment. Therefore, there is a need to develop a cost-effective transduction mechanism for biomarker detectors that could be used for cancer screening at the point-of-care preferably using as a single finger-prick blood droplet from the patients that have the combination of high sensitivity, high specificity, and low complexity to detect cancer at an early stage.

To address the limitations of the current techniques for biomarker detection, we developed a label-free automated real-time image processing technique based on dielectrophoresis (DEP) spectroscopy that is an effective transduction mechanism of a biosensor for the disease biomarker detection.

1.2. Electrokinetics

The study of the motion of microparticles with or without charge in a suspended medium under the influence of an electric field is called electrokinetics [45]–[47].

An electric double layer is formed at the solid-liquid interface when a charged particle is suspended in an ionic solution. This is a layer surrounding particles at the dispersed phase including those ions adsorbed on the surface of the particles and a countercharged dispersion medium [48].

The electric double layer consists of the following:

1. Surface charge: These are the charged ions that are adsorbed on the particle surface.
2. Stern layer: These are the counter ions with charges opposite to the surface charge. These are attracted towards the particle surface and are closely attached to the surface by the electrostatic force. The electric potential drops linearly across this layer. A layer of weakly bound ions is formed beyond the stern layer but within a distance corresponding to Debye length [49].
3. Diffuse layer: This is a thin film that is formed adjacent to the particle with free ions with a higher concentration of counterions. The potential drops exponentially across this layer.

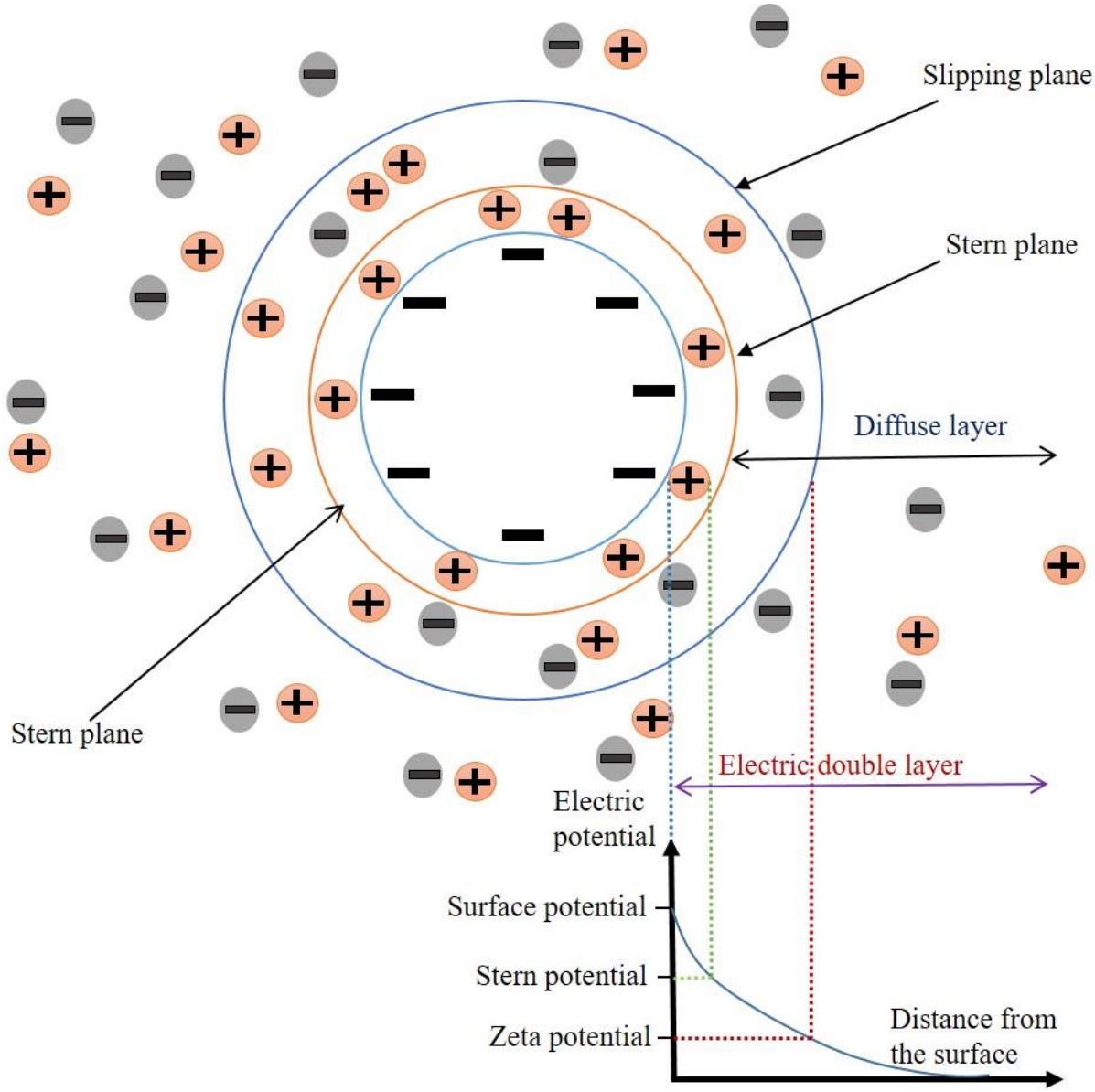

Figure 1.1: Diagram of electric double layer

The diffuse layer and the bulk electrolyte solution are separated by an interface called a slip plane. The potential at this plane is called the zeta potential. As shown in figure 1.1 the charged surface is electrically screened beyond the Debye length away from the diffuse layer. The Debye length, L_d is given by [50]

$$L_d = \sqrt{\varepsilon_o \varepsilon_m kT \Big/ 8\pi N_0 Z^2 q^2}$$

where ε_o is the permittivity of the free space, ε_m is the relative permittivity of the medium, k is the Boltzmann constant, T is the absolute temperature, N_0 is the bulk concentration of ions in the electrolyte, Z is the valence of the electrolyte and q is the charge on an electron.

1.2.1. Dielectrophoresis

Dielectrophoresis is an electrokinetic phenomenon that acts on dielectric particles in a conductive solution in the presence of a inhomogeneous electric field [51]. The term dielectrophoresis was coined by Pohl in 1951 from a Greek work "phorein, an effect in which the particle is carried due to its dielectric properties [52].

Pohl defined this effect as "the motion of suspensoid particles relative to that of the solvent resulting from polarization forces produced by an inhomogeneous electric field." A dielectric (or dielectric material) is an electrical insulator that can be polarized by the application of an electric field. When a dielectric particle is placed in an applied electric field the electrical charges do not pass through them due to their insulator characteristics, but these electric charges deviate marginally from their equilibrium positions. Due to this, a dielectric polarization is caused on the dielectric materials [53], [54].

Exposing a polarizable particle to an electric field will induce electrical charges on the particle. These induced electrical charges will then act upon the dipole to align them parallel to the applied electric field. If this electric field is non-uniform, a net force will be imposed due to uneven Coulomb forces acting upon the dipole. Based on the particle's polarizability in comparison with that of the suspending medium, the particle can move towards or off the region of the applied electric field. This motion is called DEP [55], [56].

If the particle is polarized more than the surrounding medium, then it experiences a net force towards the high electric field region and will be attracted towards the right electrode as

shown by the figure labelled positive dielectrophoresis in figure 1.2. This is known as positive DEP. If the particle is polarized less than the surrounding medium, then it moves toward the low electric field region on the left electrode as shown by the figure labelled positive dielectrophoresis in figure 1.2. This process is known as negative DEP [57]. This is depicted in figure 1.2.

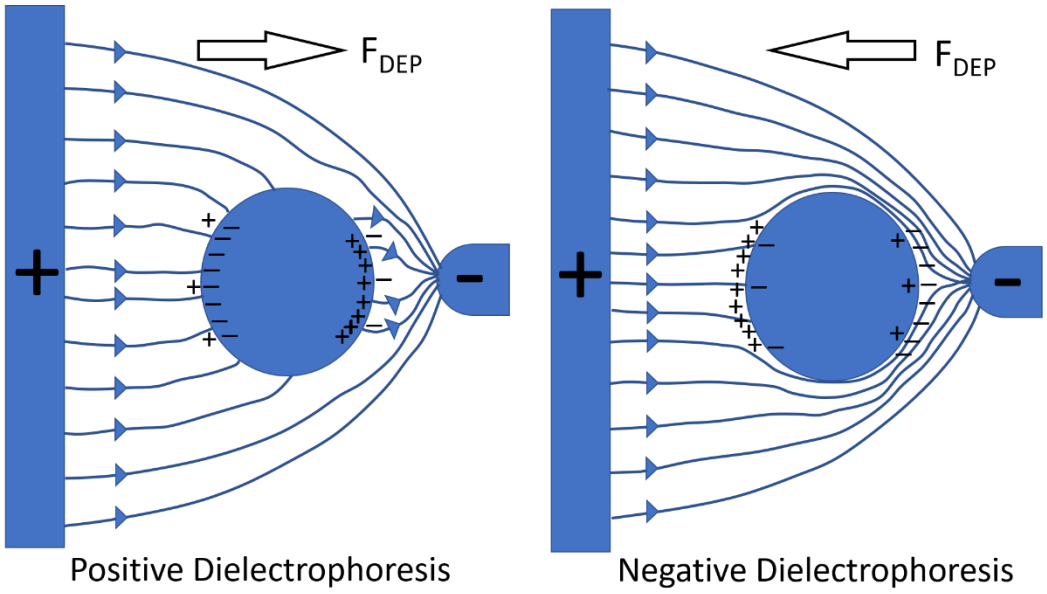

Figure 1.2: DEP effect acting upon dielectric particle in a non-uniform electric field. The left figure depicts the particle is experiencing positive DEP and the right figure depicts the particle is experiencing a negative DEP effect.

The DEP force can selectively segregate, concentrate, or refine target molecules or particles from a complex sample by either attracting them to or repelling them from the electrodes. The translational forces produced due to attraction or repulsion are due to the interactions of the dipole moment of the particles with the applied non-uniform electric field [57].

The time-averaged DEP force on a spherical particle of radius r is given by

$$\langle F_{DEP} \rangle = 2\pi\varepsilon_m r^3 Re[K_{\mathrm{CM}}(\omega)]\nabla E^2,$$

Where,

$$K_{\mathrm{CM}}(\omega) = \frac{\varepsilon_p^* - \varepsilon_m^*}{\varepsilon_p^* + 2\varepsilon_m^*}$$

is the Clausius–Mossotti factor, which is the effective polarizability per unit volume of the particle, ε_m is the permittivity of the medium, ε_m^* is the complex permittivity of the medium, ε_p^* is the complex permittivity of the particle, ∇E is the electric field gradient.

The polarizability of the spherical particle is as:

$$\alpha = 4\pi r^3 \varepsilon_m Re[f_{CM}(\omega)]$$

Where r is the radius of the spherical dielectric particle, ε_m is the permittivity of the suspending medium, ω is the radial frequency of the applied electric field, and $\boldsymbol{Re}\{f_{CM}(\omega)\}$ is the real part of the Clausius-Mossotti factor (CM) and for the spherical particle, is defined as:

$$f_{CM}(\omega) = \frac{\varepsilon_p^* - \varepsilon_m^*}{\varepsilon_p^* + 2\varepsilon_m^*}$$

where ε_p^* is the complex permittivity of the dielectric particle and ε_m^* is the complex permittivity of the suspending medium. The complex permittivity is given by $\varepsilon^* = \varepsilon - j(\frac{\sigma}{\omega})$ with σ the real conductivity, ε the real permittivity, and $j = \sqrt{-1}$ and ω the angular frequencies [49], [56], [58]–[72].

Deviations in the CM factor change the value of α and consequently differ the DEP force. In the case of the sphere, the real part of the CM factor is theoretically bounded between –1/2 and 1. Positive DEP occurs when $Re[f_{CM}(\omega)] > 0$ and negative DEP occurs when $Re[f_{CM}(\omega)] < 0$. If $Re[f_{CM}(\omega)]$ becomes zero under certain conditions then the DEP force acting on the polarized particles also becomes zero [59], [66]–[71]. The frequency at which zero DEP force occurs is called crossover frequency (f_{CO}), which is represented as:

$$f_{CO} = \frac{1}{2\pi\varepsilon_0}\sqrt{\frac{(\sigma_m - \sigma_p)(\sigma_p + 2\sigma_m)}{(\varepsilon_p - \varepsilon_m)(\varepsilon_p + 2\varepsilon_m)}}$$

where σ is the real conductivity and ε is the real permittivity, and sub-index p, m are the particle and medium respectively [59], [66], [73]. It has been validated that f_{co} depends on the conductivity (σ_p) of the particle at low frequencies (< 1MHz) [74]. The conductivity (σ_p) of the homogeneous dielectric spherical particle is the sum of bulk conductivity ($\sigma_{p,\text{bulk}}$) and surface conductance (K_S), which is given as:

$$\sigma_p = \sigma_{p,\text{bulk}} + \frac{2K_S}{r}$$

where r is the radius of the spherical particle. Based on the material of the particle, the bulk conductivity ($\sigma_{p,bulk}$) can be negligible. Thus, surface conductance (K_S) provides a leading impact to the conductivity of the particle [59], [66], [71], [73].

Dielectrophoresis has been widely used in applications directed towards biomedical and biotechnology sciences. DEP was first used in the biomedical field to study the cells and their response towards the DEP force in understanding their physicochemical properties. Later this technology was used in cell sorting, tissue engineering, and biosensors.

DEP has also been used to characterize and manipulate biological particles such as blood cells, stem cells, neurons, pancreatic β-cells, bacteria, and yeast, DNA, Viruses, proteins, chromosomes, and cell viability [75].

DEP has been used in drug delivery assessment and analysis. Drugs such as Gefitinib (ZD1839), Cycloheximide (CHX), Cisplatin and docetaxel, and Terbinafine and insulin are used in drug treatment assessments and drug screening using DEP [75].

DEP has been used in several DNA studies due to its advantages in isolation and separation of small particles. Some of the DEP investigations of DNA include DNA transfection, the discovery of circulating cell-free DNA from plasma, detection of DNA from whole blood,

characterization to immobilized DNA, cancer cell-free DNA isolation, and trapping DNA single-DNA molecule [75].

DEP is a cost-effective, rapid, precise, and label-free analytical diagnostic and screening technique. DEP offers several benefits in isolating, trapping, separating, concentrating, and fractionating bioparticles down to the nanoscale [49], [51], [76]–[80] when compared with other methods, such as magnetic separation [81]–[84].

2. DEP SPECTROSCOPY APPLICATION

We developed an image processing software that will track the motion of the particles along the concentric lines using the Microsoft foundation classes application using visual C++ that is compatible with the Microsoft Windows operating system. Visual C++ will allow the user in creating, debugging, and executing applications as well as the applications that target the .NET framework.

The application that we developed uses a USB class camera from which the images processed in the application are being captured. In our experiments, we used a Proscope 5 megapixel microscope compliant camera. The application captures the live video and the time-lapse images from the Proscope camera. As the images are being captured, the application also does real-time image processing. Real-time image processing provides the complete pixel information from each time-lapse image.

The application was designed to make it user-interactive using dialog boxes. We have used CDialog class which acts as an interface for managing the boxes used in the application. This is a two-phase process that includes constructing the dialog object and then creating a dialog window. Using the inbuilt MFC's CWinapp we created the codes that were generated.

Multiple dialog boxes were then added to the application wizard to create features that will be used to determine the DEP spectroscopy. The home screen of the application has the following buttons:

1. Set Box Coordinates
2. Start Experiment
3. Stop Experiment
4. Delete Results

5. Save Image
6. Save Result
7. Autosave Settings
8. FreqGen Settings

The home screen has the following check buttons:

1. Auto Image Capture
2. Autosave Results

The image of the home screen looks as below:

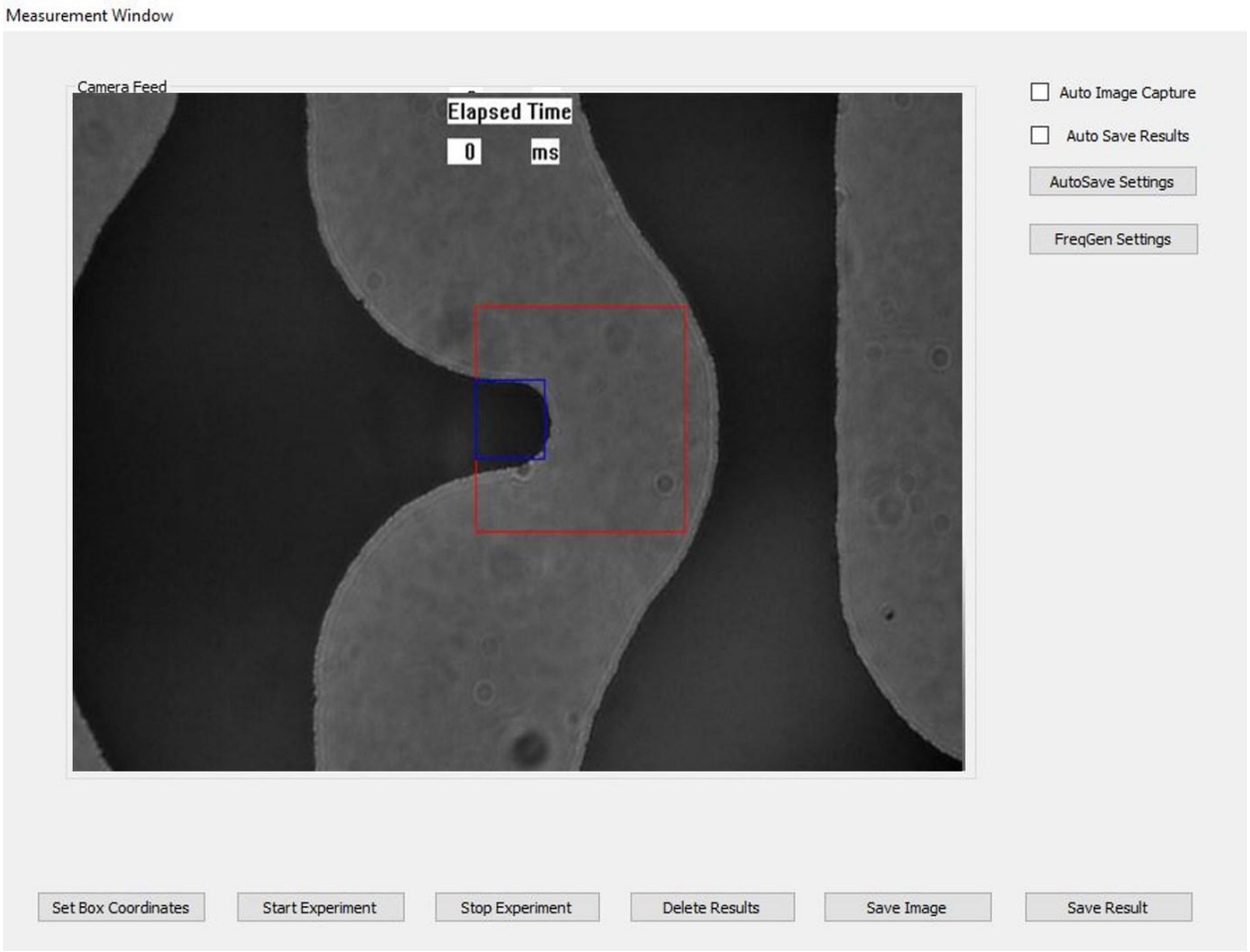

Figure 2.1: DEP spectroscopy application Home screen displaying the live greyscale video feed

Set box coordinates: this button lets us set the height, width, angle, and coordinates of the boxes in the *X* and *Y*-axis. The region of interest used in the experiment will be set using this dialog box. The application lets us set eight boxes in which four of the boxes can be tilted at any angle. The dialog is as shown below:

Figure 2.2: Box coordinates setting dialog window

Start Experiment: Clicking this button triggers the application to begin. Commands are sent to the function generator if it is connected to the computer, the timer starts, and the real-time image processing begins.

Stop Experiment: Clicking this button stops the application and saves the results obtained until this button is clicked. Clicking this button sends the command to reset the timer and write results into the comma-separated value (CSV) files.

Delete Results: Clicking this button erases all the results present in the written CSV file. Clicking this button does not produce any effect if there is no data written into the CSV file.

Save Image: Clicking this button saves the current image from the live video stream. This command is independent of the other modules. Once this button is clicked, the current image is

saved directly into the output folder. An arbitrary number of images can be independently saved using this button. Each time this button is pressed, the loop will increment the image number before saving the image in the output folder with the image number in the file name.

Save Result: Clicking this button saves the image shown on the screen.

Autosave Settings: Clicking this button redirects the user to another dialog box that lets the user control the time interval to capture the time-lapse images and the time interval to process and write the image information. We have used time intervals in multiples of 40 ms. This time interval was selected based on the processing speed of the hardware, interfacing time with the function generator, and the frame rate of the video stream. The Autosave Setting dialog box is shown in figure 2.3.

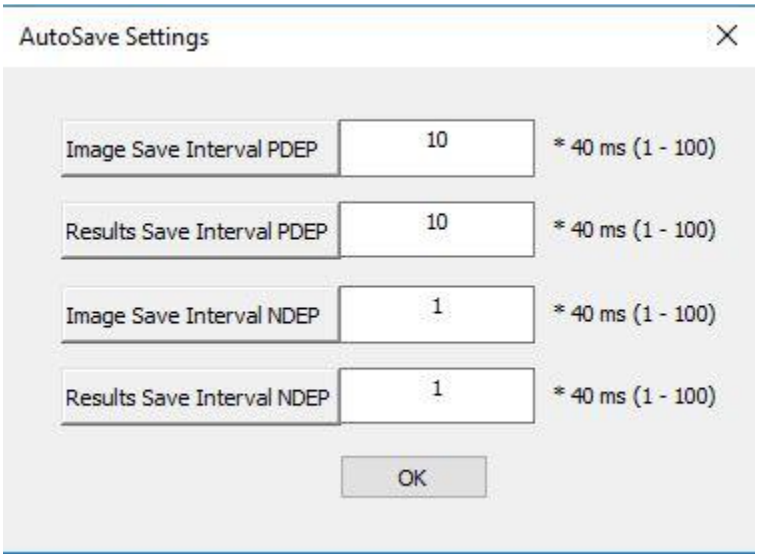

Figure 2.3: Autosave Setting dialog box

Function Generator Setting:

This button prompts a new dialog box that will let the user control the parameters to be set in the function generator. The dialog lets the user set the address of the function generator to communicate with the application. The peak to peak voltage, the starting frequency, stop frequency, increments in the frequency, the period of the frequency signal before switching can be

set in this dialog. The dialog lets us two radio buttons in which the user can select if the application starts with the frequency to produce either positive or negative frequency. We have included a check box called simulate frequency. Once this box is checked, the application emulates the action of the function generator, which can be used during the testing of the application. The settings dialog box is as shown in figure 2.4.

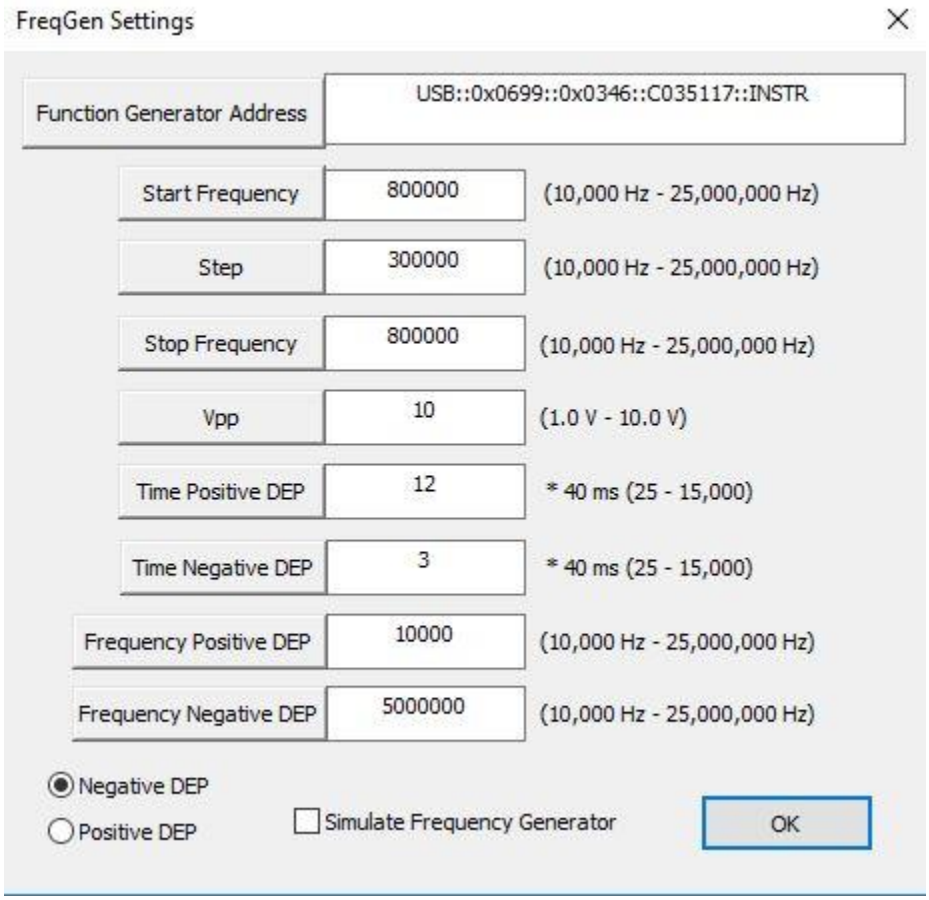

Figure 2.4: Function Generator Settings dialog window

In this research, we have used the AFG3000 series Tektronics function generator that was connected to the computer using a USB cable. The first step involves the installation of the Tektronics function generator in the windows operating system. The next step was to establish the communication between the function generator and the application. To do so we have used Virtual Instrument Software Architecture (VISA) software. This is an industry-standard communication

protocol that provides communication with the instrument that is in connection with the PC using several communication buses. In our case, as we used the Tektronics function generator we had to use TekVISA which is a VISA version of Tektronics. This is comprised of a communication driver, USB test, and measurement class driver which acts as an instrument connection manager, instrument communication logger, and instrument communication tool.

The algorithm was initially developed by Syed Kirmani. The application had a few drawbacks such as high execution time (80 minutes to evaluate four frequencies) and higher storage to save the file (each set needed 480 MB of storage). This resulted from the images captured being saved in the RGB format in the hard drive of the computer during the image acquisition. This problem was addressed in the revised algorithm. The algorithm captures and saves each image in the RAM of the computer, and once the process is complete the results and images will be dumped into the hard drive. The execution time for the revised algorithm is 60 seconds for the four frequencies. The resulting file is now reduced to 3.15 MB. The flowchart of the algorithm is as shown in figure 2.5.

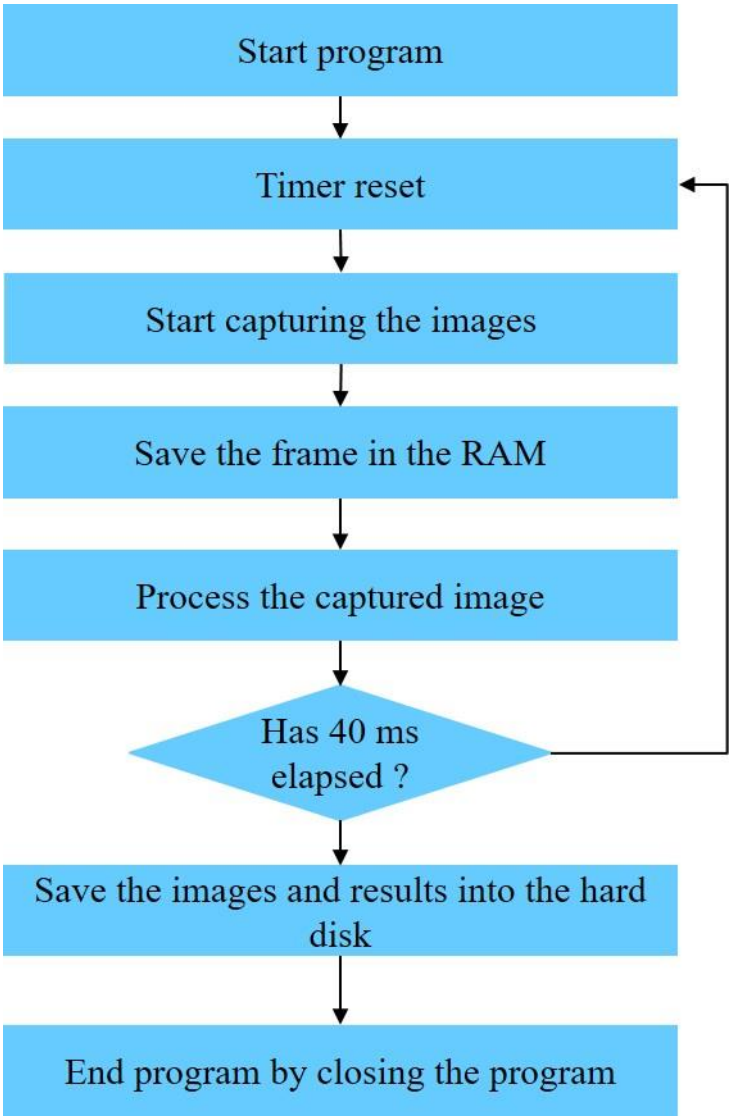

Figure 2.5: Flowchart of the DEP spectroscopy application

However, the Visual C++ environment is not compatible with the Tektronics user commands. Thus, we used Interchangeable Virtual Instrument (IVI) drivers that are compliant with MFC in Visual C++. In this software, we used a LabWindows™/CVI, which is an ANSI C integrated development environment (IDE) by National Instruments that was compatible with the Tektronics drivers.

The application creates the output files in the same folder in which the DEP spectroscopy app exists. The output file is saved in CSV format. The image pixels are stored in the memory as a single unsigned character array.

The image pixel is as shown below:

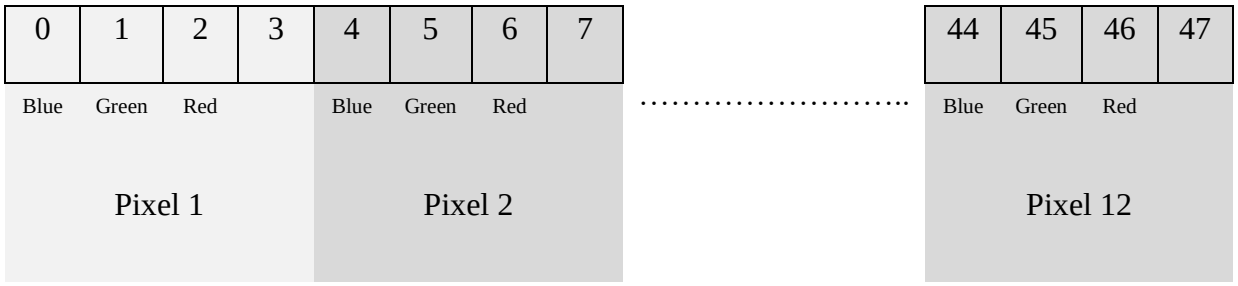

Figure 2.6: Image pixel storage format

The image pixel plotted on the screen are arranged as shown in Figure. 2.7:

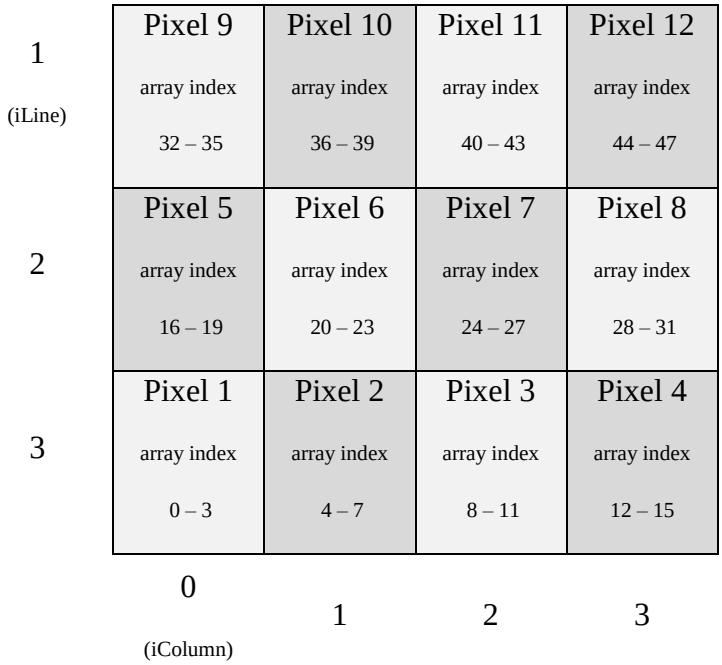

Figure 2.7: Pixels observed on the screen

Each of the pixel information for the rows and columns will be added using the equation:

$$\text{Index} = (\text{Image}_Y - \text{iLine}) \times \text{Image}_X + \text{iColumn}$$

Here iLine represents the rows and iColumn represents the column.

The calculation of the image intensity based on the pixel information is done by raster scanning through rows and columns. The electrode tip is curved and the sample movement from the tip of the electrode follows an elliptical pattern. Then observing the patterns of the bead movement, we decided it is best to have a radial scan over the row to column-based scan. The pattern followed an ellipse-like tracking of the beads. The figures are as shown in figure 4.

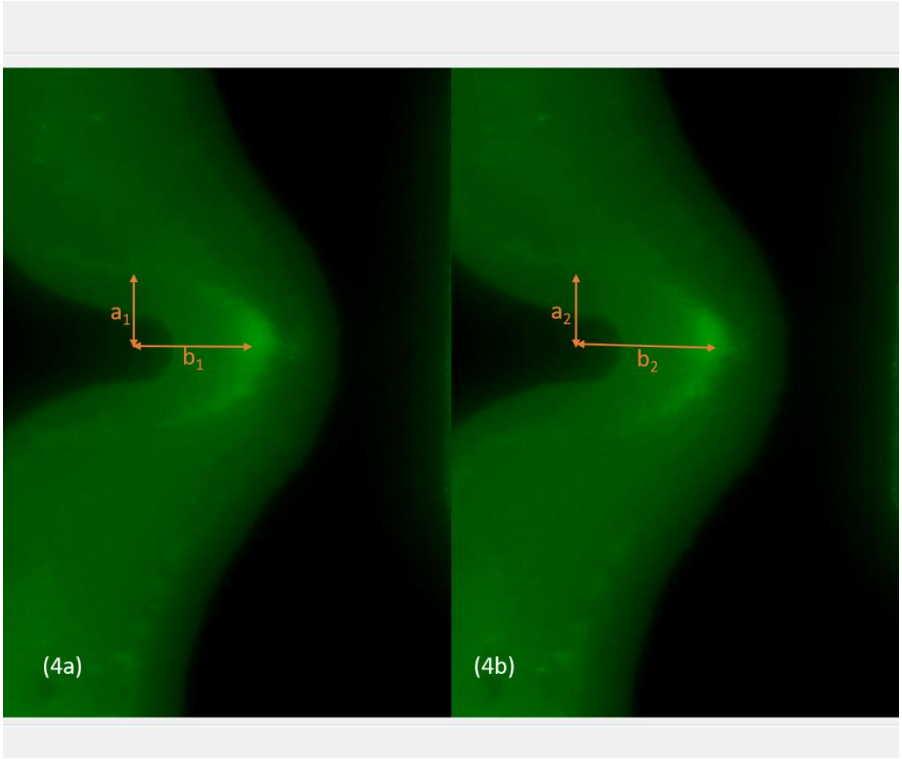

Figure 2.8: PM distribution pattern, which follows an elliptical pattern, where *b* is the major axis and *a* is the minor axis. (a) at *t* = 40 ms. (b) at *t* = 80 ms.

The ratio of *b*/*a* was consistently equal to 1.5. The pattern had to be radial so we decided to start from the center position where *a* and *b* are placed.

The dynamic radius would be, $r = \sqrt{(Y_2 - Y_1)^2 + (X_2 - X_1)^2}$

With an angle of

$$\theta = tan[\frac{(Y_2 - Y_1)}{(X_2 - X_1)}$$

Since we use b = 1.5 aThe raster scan in this application calculates and records the pixel information of the image based on the above equation, thus making this efficient as it only tracks and records the bins of the bead motion as shown in figure 2.8.

3. NUCLEOTIDE IDENTIFICATION IN DNA USING DIELECTROPHORESIS SPECTROSCOPY[1]

3.1. Introduction

Genetic markers are used to follow the inheritance patterns of chromosomal regions from generation to generation and are used in identifying the genetic variants associated with human disease [28]. The most common genetic variations are single nucleotide polymorphism (SNP), which is due to the differences in single base substitution. In every DNA sequence, SNP represents a difference in a single nucleotide [29]. SNP may replace a single nucleotide [30] (A, T, G, and C) with any other nucleotide. Previous research has shown that SNP predicts an individual's risk of developing certain diseases such as cardiovascular disease, type 2 diabetes, autoimmune disease, cancer, and the individual's response to certain drugs [31]–[33], [85], [86]. These small differences can be used to track an individual's susceptibility to environmental factors such as toxins [34]. Since SNPs are stable over generations, they are excellent genetic markers. It is important to explore the role of SNPs in the genetic analysis of the disease as they would carve out the identification of complex diseases and genetic disorders [35]. Even though SNPs are an important factor in genetic variation [36], [37], detecting SNPs is still expensive and time-consuming with existing techniques.

SNP genotyping can be performed with DNA sequencing methods [38]. The same gene of different samples is aligned, compared with the help of PCR amplification, and analyzed for resequencing to detect SNPs.

[1] This chapter was extracted from a published article in Micromachines (F. D. Gudagunti, L. Velmanickam, D. Nawarathna, and I. T. Lima, "Nucleotide identification in DNA using dielectrophoresis spectroscopy," Micromachines, vol. 11, no. 1, 2020, doi: 10.3390/mi11010039). Conceptualization, I. T. Lima and F. D. Gudagunti; Formal analysis, F. D. Gudagunti and L. Velmanickam; Investigation, F. D. Gudagunti and L. Velmanickam; Methodology, F. D. Gudagunti, L. Velmanickam, D. Nawarathna and I. T. Lima; Project administration, I. T. Lima; Writing—original draft, F. D. Gudagunti; Writing—review & editing, L. Velmanickam, D. Nawarathna and I. T. Lima.

The sequencing alignment helps detect the locations of the nucleotides that experience SNPs with high accuracy. There are few sequencing methods such as Sanger sequencing, qPCR, 454 pyrosequencing, Illumina, Ion Torrent, and Endpoint PCR methods [87]. Although these sequencing techniques have low error rates, those pieces of equipment are expensive [39], [88]. Another method for SNP detection is Restriction Fragment Length Polymorphism (RFLP). The difference in the length of homologous DNA sequences from differing locations broken by a specific restriction enzyme is illustrated in gel electrophoresis [89], [90]. This method is also expensive and complex since it needs a strong binding framework [90].

Mapping and Assembly with Quality (MAQ) maps shotgun reads that can build the assemblies by using value-based scores to derive genotype calls of the consensus sequence of a diploid genome. This technique is based on the Bayesian statistical model that includes error probability and mapping qualities from the quality scores of the sequence. Although minimum order quality (MOQ) [91] is efficient and highly sensitive, the high probability sequencing errors make it less reliable than other methods.

The program Short Oligonucleotide Analysis Package (SOAP) is a resequencing tool that references the raw sequencing reads and the consensus sequence for the genome sequence to be tested. A comparison is done on the consensus sequence with the reference to identify SNPs. This method [92] incorporates the data quality, alignment, and recurring experimental errors, making this method complex and with large acquisition time.

TaqMan PCR is a fast and reliable tool for genotyping. There are few applied biosystem instruments like real-time PCR which are available for the processing of TaqMan SNP Genotyping assays. The endpoint read can be performed on such applied biosystems as real-time PCR. The results from this method are highly accurate and are reproducible, although the biosystem involved

is expensive and time-consuming. The amplification of the alleles is done using two pairs of primers. This process involves overlapping of the primer pairs so that it matches the pairs but not to the alternative allele for the SNP [93], [94].

Another SNP genotyping method is high-resolution electrophoresis (sequencing gel). The method is based on allele-specific ligation. The ligation occurs when the probe is situated towards the sequence that matches the template. Thus, the genotype is based on the presence or absence of the ligated product. Low throughput, time-consuming, and high cost are a few disadvantages of this method [95], [96].

To address the limitations on the current techniques for SNP detection, we developed a label-free automated technique based on dielectrophoresis (DEP) spectroscopy [97]–[99] that is an effective transduction mechanism of a biosensor for SNP detection.

3.2. Material and Methods

3.2.1. Sample preparation

The sample preparation consists of the following steps:

- Step 1: Streptavidin attachment to biotinylated polystyrene microspheres (PM). Biotinylated PM with 750 nm diameter was purchased from Spherotech Inc. The first step in the preparation of samples consists of binding the biotinylated PM with the antigen Streptavidin purchased from Vector Labs Inc. Biotin acts as a conjugate to the protein Streptavidin and they form a strong bond with very high affinity. This process is done first by adding a 3 µL Streptavidin solution into a 10 µL biotinylated PM solution at 70°F in a centrifuge tube to have 100% binding, according to the manufacturer recommendation. The total volume was set to 400 µL by adding 0.01× phosphate-buffered saline (PBS) solution with a conductivity of 0.01 S/m. Then, the

sample was uniformly mixed using a vortex machine and left on a shaker for 20 min for the Streptavidin–biotin-binding process. After 20 min, the tube was centrifuged at 5000 rpm for 14 min to remove the unbound Streptavidin molecules and the buffer.

- Step 2: Biotinylated DNA attachment to the biotinylated PM + Streptavidin. Each Streptavidin molecule can bind up to 4 biotin molecules [45]. One binding site of each Streptavidin molecule is used to bind that Streptavidin molecule with the PM. The remaining three Streptavidin binding sites bind with three biotinylated DNA. First, 3 µL of biotinylated DNA purchased from The Midland Certified Reagent Company was added into 397 µL of 0.01× Tris-EDTA to have 100% binding of the biotinylated DNA with all the Streptavidin molecule binding sites, according to the manufacturer requirement. Then this sample was added into the solution with Streptavidin–biotin PM and uniformly mixed using a vortex machine. After that, the sample was kept on a shaker for 20 min at 70°Ffor the biotinylated DNA to bind with the Streptavidin molecules of the PM. After 20 min, the tube was centrifuged at 5000 rpm for 14 min to remove the unbound DNA antibody molecules and the buffer.
- Step 3: Finally, 200 µL of 0.1× TE buffer was added to the centrifuge tube and mixed uniformly. 10 µL of this sample solution was pipetted on to the microelectrodes and used for each experiment.

The DNA sequence with a change in the last nucleotide is as follows:

- 5’-(biotin) TGTTGTGCGA-3’
- 5’-(biotin) TGTTGTGCGT-3’
- 5’-(biotin) TGTTGTGCGG-3’
- 5’-(biotin) TGTTGTGCGC-3’

The DNA sequence with a change in the second last nucleotide is as follows:

- 5'-(biotin) TGTTGTGCAC-3'
- 5'-(biotin) TGTTGTGCTC-3'
- 5'-(biotin) TGTTGTGCCC-3'.

To measure the drift velocity of the dielectric particle due to DEP, we developed a software package using Microsoft foundation classes in visual C++ in the Windows operating system. The software interacts and controls with the USB video class (UVC) standard compliant microscope camera, Tektronix AFG series function generators, and the pearl-shaped interdigitated electrode. This application captures and displays time-lapse images from the sequence of video frames recorded at 25 frames per second by the UVC standard-compliant microscope camera. With the application controlling the function generator the frequency is swept at low and high values so to apply the positive and negative DEP. The experimental setup is as shown in figure 3.1.

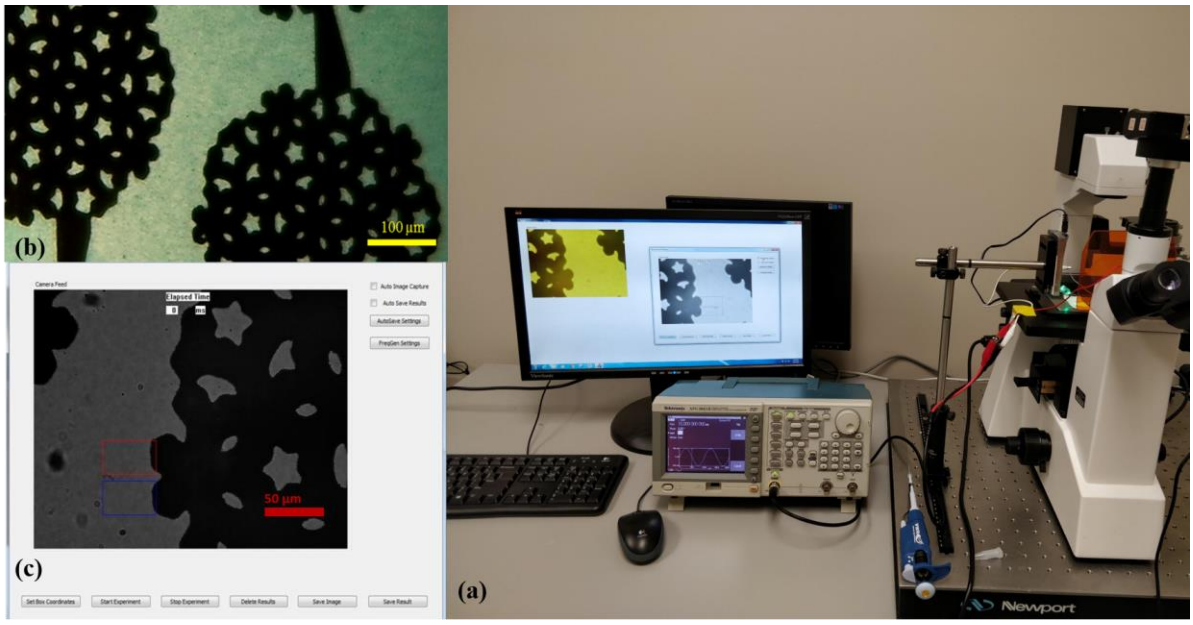

Figure 3.1: SNP sensor prototype: (a) Experimental setup. (b) Interdigitated electrodes were used in the experiments. The electrode is visible as the darker region in the picture. Scale bar indicates 50µm. Multi-colored hollow rectangles depict the regions of interest for measurements and analysis. (c)The interface of Microsoft Windows application for dielectrophoresis (DEP) spectroscopy.

The microscope camera extracts the pixel information of the live video using a real-time image processing algorithm. The region of interest to observe the DEP effect is set by placing rectangular boxes (as shown in figure 3.1c) in which the pixel and color information is extracted and with this data, the drift velocity as a function due to DEP force as a function of the frequency of the electric field is calculated using the algorithm. The time-lapse images captured for the calculation of the drift velocity can be set to desired time intervals. The least possible capture time that can be set is 40 ms due to the processing speed of the hardware and the frame rate in which the video is captured.

3.2.2. Pearl-shaped interdigitated electrode

The direction of movement for the dielectric particle due to DEP depends upon the relative polarizability of the particle and the medium and on the presence of a large gradient of the electric field intensity produced by electrodes [98]. In the experiments, we used pearl-shaped interdigitated electrodes designed and fabricated at North Dakota State University. The initial design of the electrode was drawn to scale using AutoCAD and then validated its electric field gradient using COMSOL Multiphysics. The electrode was fabricated on a commercially available glass wafer with standard fabrication procedures involving photolithography, metal sputtering, and lift-off procedures using 1000 Å thick gold film in the microfabrication facilities at North Dakota State University. Using COMSOL we verified the maximum electric field of the electrode was 1.8×10^4 V/m and the gradient of the electric field intensity was high as 3×10^{12} V^2/m. We observed no variation on the root mean square of the electric field and the electric field gradient produced by this electrode to a frequency ranging from several kHz to a few MHz. The same electric field is applied to the particle and the medium in all frequency range and thus, making the DEP depend only on the real part of the Clausius-Mossotti factor [100].

3.2.3. Dark-field illumination set up

A custom-made dark-field illumination setup is built using a 10 mm green LED light mounted at 45° on the optical post assemblies. The setup was designed based on the principle of dark field microscopy, in which the object is illuminated against a dark background. The illumination setup consists of resistors and a Led in series connection. We have used XICON 5W 100 Ω in series with 3.2V, 10mm diameter with the domed top LED with a dominant wavelength of 516 nm. The circuit is as shown below.

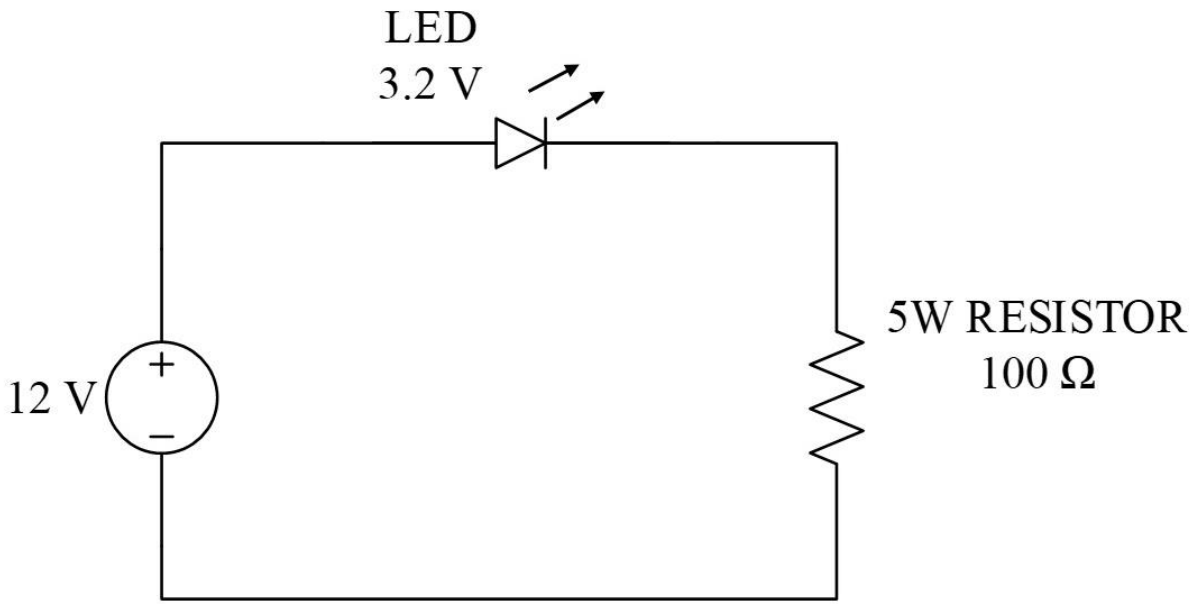

Figure 3.2: Circuit diagram of dark-field illumination set up

The LED was mounted on a heat sink which acts as a passive heat exchanger that transfers heat generated by the LED, dissipating the heat away from the sample and thereby allowing the regulation of the LED's temperature at optimum levels. The LED was placed 0.5 – 1 cm away from the sample placed on top of the electrode. The LED was mounted at an angle of 45°. This angle of incidence reduces the amount of light collected by the camera that does not result from light scattering from the PM.

If a particle or a liquid molecule in our case interacts with an electromagnetic wave, the charges of the particle will be in oscillatory motion due to the electric field incident wave. These charges would radiate back the electromagnetic energy in various directions which are called scattering.

When 10 µL of the assay was pipetted on the surface of the electrode, a portion of the light scattered from the antigen-bound PM is collected by the objective of the microscope, resulting in a sharp image of the antigen-bound PM. Since the diameter of the antigen-bound PM is of the same order as the wavelength of the green LED (565 nm), the antigen-bound PM appears very bright on a dark background due to Mie scattering.

Mie scattering was formulated by Gustav Mie to describe the light scattering on colloidal gold particles suspended in water. For Mie scattering on suspended particles to occur, the particles should have a diameter similar to or less than the wavelength of the incident light [101]. The scattered light is proportional to the diameter of the particle, which in our case consists of the PM. Since the size of the particles used is comparable to the wavelength of the source, the photons emitted by the source experience Mie scattering. The angular dependency defines the intensity of the scattering with smaller particles which we have used in our experiments.

The sample was pipetted on the surface of the electrode. The side illumination makes the light scatter from the biotin bound PM and part of the scattered light was captured on the microscope camera, resulting in the image of the PM. The diameter of the biotin functionalized PM was of the same order as the wavelength of the green LED, making the biotin bound PM appear much brighter than the background due to Mie scattering.

3.2.4. Frequency sweep and real-time image processing

The drift velocity was measured from the point of application of positive DEP to the negative DEP at the applied frequency. Positive DEP is used to attract the PM to the convex edge of the electrodes. That was done through the application of a low frequency such as 10 kHz to the electrodes. Negative DEP was used to repel the PM from the convex edge of the electrodes to enable drift velocity measurements, which were produced with frequencies on the order of hundreds or thousands of kHz. This process enables an indirect measurement of the negative DEP force, since the DEP force was proportional to the drift velocity due to the viscosity of the solution. The custom-made software was programmed to sweep a set of the alternating frequency generating positive and negative DEP. The experiments were run at a minimum frequency of 500 kHz and a maximum of 2 MHz in linear steps with 10 V peak-to-peak.

A preliminary set of experiments were conducted to determine the choice of time intervals for the application of negative and positive DEP [102]. The time interval set for the positive DEP was set to 1000 ms and for the negative DEP, it was set to 40 ms per frequency measurement. With the application of positive DEP for 1000 ms at 10 kHz, the PM accumulates on the convex edges of the interdigitated electrodes. The software automatically switches the frequency to a higher value after 1000 ms, inducing a negative DEP effect for 40 ms. The cycle repeats with the application of positive DEP and the following frequency that produces negative DEP along until the stop frequency is reached. The system acquires the frames at 0 ms and 40 ms after the application of a frequency that produces negative DEP to measure the average drift velocity of the PM. The function generator used in the experiments is a Tektronix AFG series that is controlled by the computer via a USB port. The software allows the user to set the time intervals for the application of both positive and negative DEP effects and enables the user to choose the sequence

of frequencies to be used in the experiments to measure the negative DEP spectrum. To improve the computational speed, the image acquisition data is saved into the RAM of the computer until the stop frequency is reached when the images are transferred to the hard drive.

The negative DEP spectrum is measured indirectly through the average drift velocity of the PM as a function of the frequency since the drift velocity is proportional to the negative DEP force. The choice of the negative DEP spectrum, as opposed to the positive DEP spectrum, results from the easier measurement of the former when compared with the latter because the PM is clustered near the convex edge of the electrode before negative DEP is applied. Moreover, there is a significantly larger frequency range that produces negative DEP on the PM that we used when compared to the frequency range that produces positive DEP.

3.3. Results

We validated our method to detect SNP using DEP spectroscopy experiments with our custom-made image processing software for observation and data acquisition. The validation of our method is as shown in figure 3.3. The initial frequency is set to 10 kHz to produce positive DEP (< 50 kHz) and the sweeping frequency from 500 kHz to 2 MHz produces negative DEP (> 250 kHz). Figure 3.3.a clearly shows the application of positive DEP and its effects of attraction of PM on the edge of the electrodes up to 0 ms, when negative DEP is applied. Figure 3.3.b shows the position of the PM band while it is being repelled away from the electrodes due to negative DEP at 40 ms. We developed a system that can calculate the drift velocity of the PM layer to indirectly measure the negative DEP force as a function of the applied frequency.

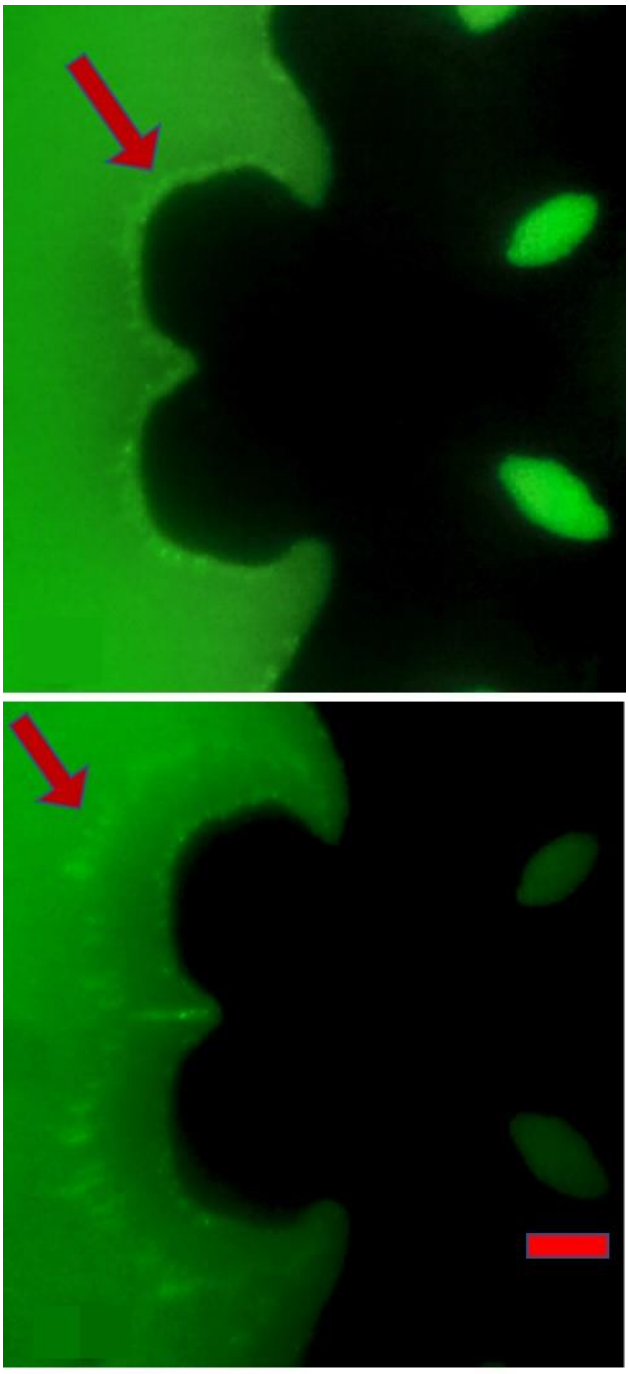

Figure 3.3: Experimental Demonstration of negative DEP effect through time-lapse images captured through DEP spectroscopy application. The electric field is changed from 10 kHz to 500 kHz with 10 Vp-p at t = 0 ms. (a) t = 0 ms and (b) t = 40 ms. The ssDNA sequence used for this is 5'-(biotin) TGTTGTGCGA-3'. The interdigitated electrode is visible as the darker region in the picture. The bright layer visible on the edge of the electrode is formed by the accumulation of the sample. The scale bar indicates 25 µm.

The region of interest, which is depicted as the rectangular box in figure 3.1.c, is processed to extract the position of the PM band as a function of the time while a frequency that produces negative DEP is applied. Figure 3.4 represents the light intensity of the images captured shortly after the application of negative DEP and 40 ms later. The average location of the PM is the center of mass x_{CM} of the light intensity curves. The difference in the center of mass of the curves results from the movement of the PM band due to the application of a frequency that produces negative DEP. The center of mass is an effective way to measure the location of the PM band to determine the velocity of the PM band. The formula used to calculate the center of mass of the light intensity curve is given by

$$x_{\mathrm{CM}} = \frac{\sum_{i=1}^{N} I_i \, x_i}{\sum_{i=1}^{N} I_i}$$

$I_i$is the value of the light intensity at the distance x_i from the convex edge of the electrode.

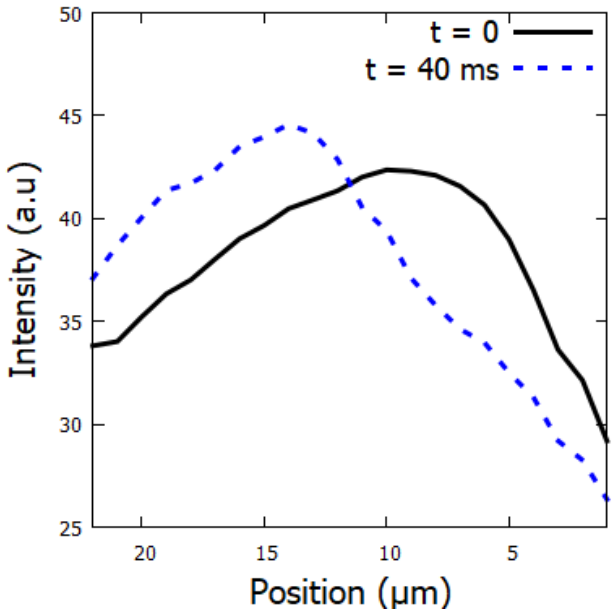

Figure 3.4: Light intensity as a function of the pixel position at t = 0 ms, when negative DEP is applied, and at t = 40 ms for the ssDNA sequence 5'-(biotin) TGTTGTGCGA-3' in 10 µL. The convex edge of the electrode is located on the right side of the PM layer, as shown in figure 3.3.

A relationship was observed between the drift velocity of the PM functionalized with ssDNA, which is proportional to the negative DEP force, as a function of frequency and the change in the single nucleotide in the last and the second-to-last nucleotide. The ssDNA sequences considered in these experiments were 5'-(biotin) TGTTGTGCGA-3' and its variations in the last and the second-to-last nucleotide. Experiments were repeated with fourteen frequencies from 1120 kHz to 1380 kHz to obtain the negative DEP spectra with higher resolution. A clear dependence was observed between the negative DEP spectrum and the nucleotide sequence. The resulting DEP spectra are shown in figures 3.5 and 3.7. Each DEP spectrum curve shown in these figures requires only 68 seconds to be obtained during the experiments. Figure 3.6 shows a higher resolution spectrum for change in the last nucleotide and Figure 3.8 shows the high-resolution spectrum for change in the second-to-last nucleotide over the same frequency range shown in figure 3.7.

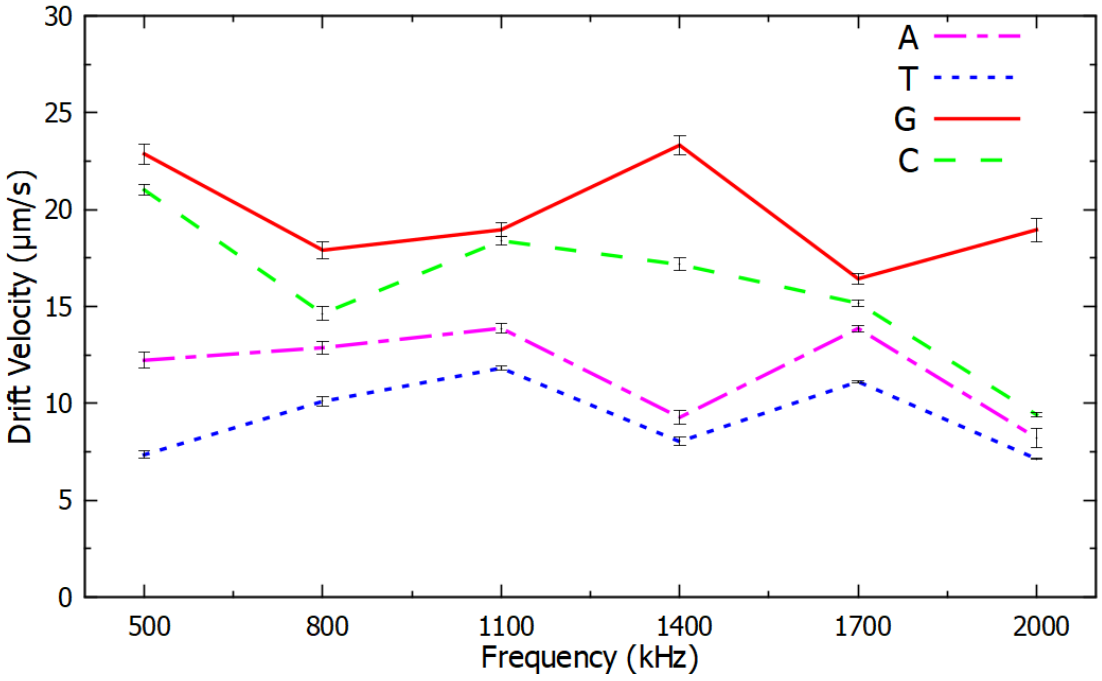

Figure 3.5: Negative DEP spectra for different nucleotides at the end of ssDNA sequences. All the other nucleotides are the same in the ssDNA sequences. The error bars show the confidence interval in a single measurement that was calculated using six measurements per frequency.

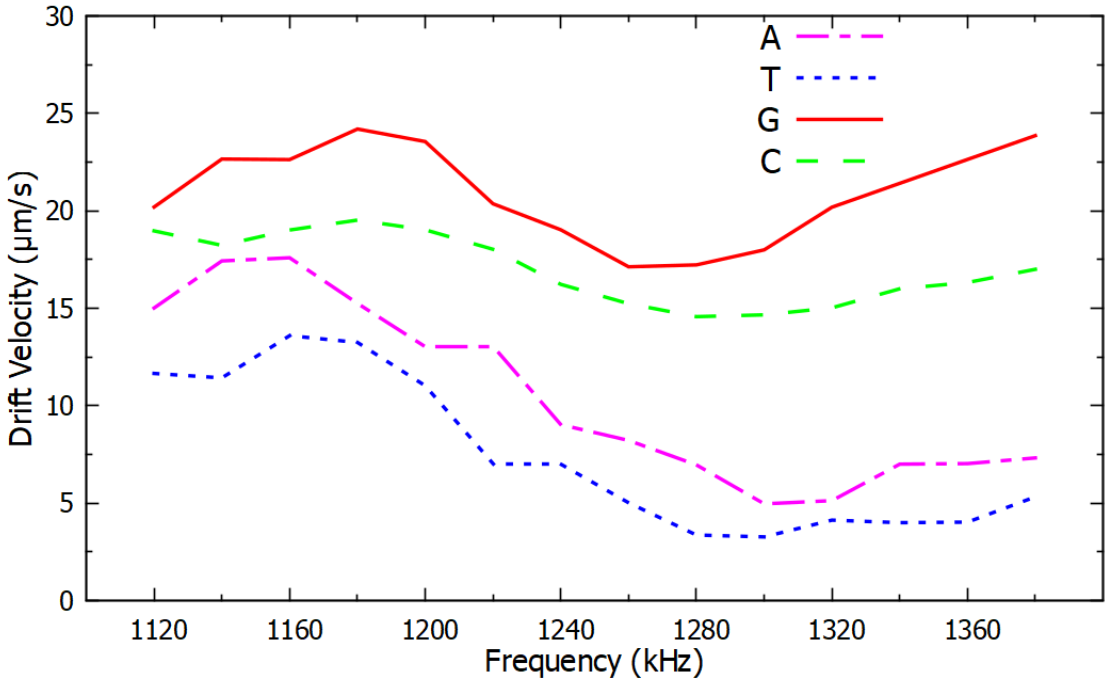

Figure 3.6: High-resolution negative DEP spectra from 1120 kHz to 1380 kHz for the same ssDNA sequences used in figure 3.5.

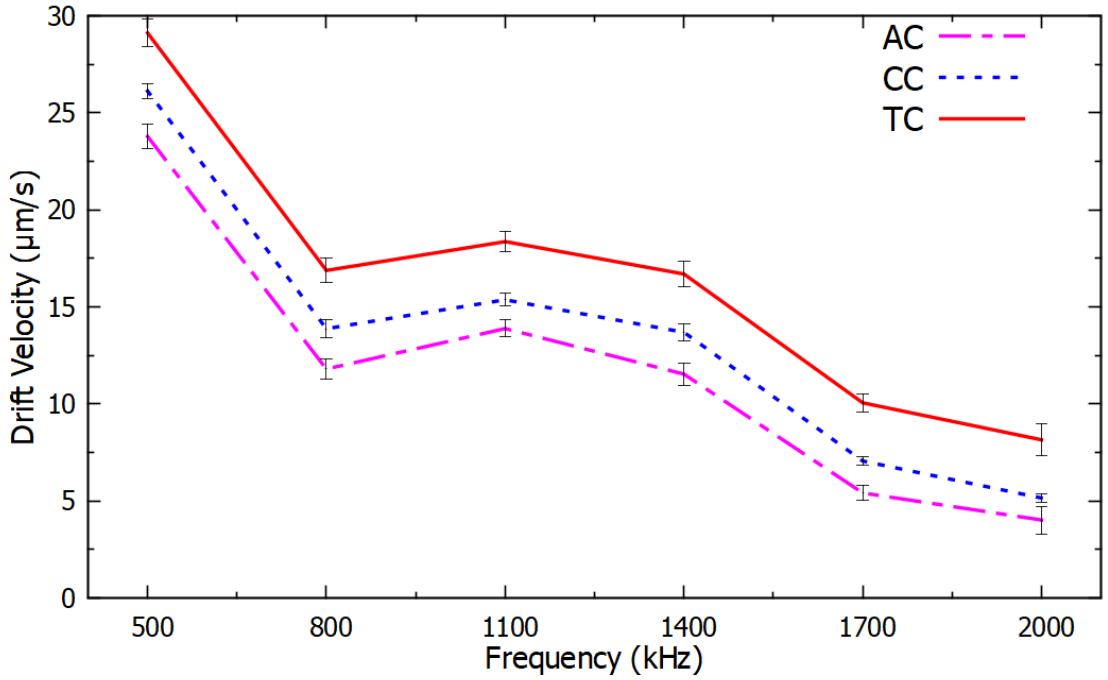

Figure 3.7: Negative DEP spectra for different nucleotides adjacent to the last nucleotide of ssDNA sequences. All the other nucleotides are the same in the ssDNA sequences. The error bars show the confidence interval in a single measurement that was calculated using six measurements per frequency.

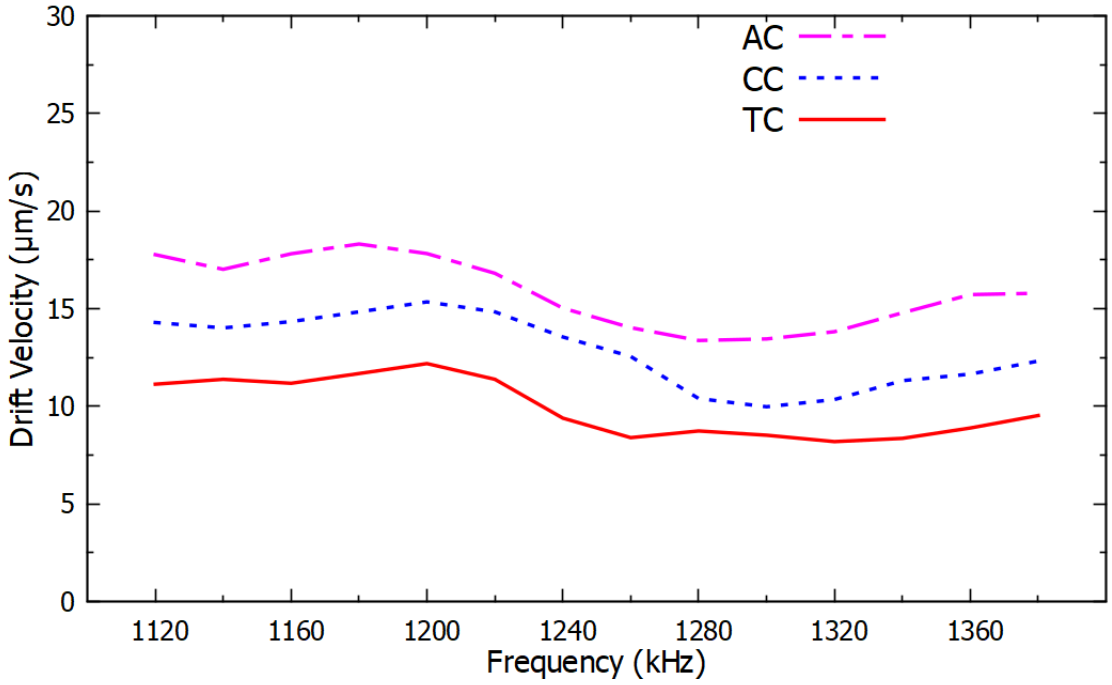

Figure 3.8: High-resolution negative DEP spectra from 1120 kHz to 1380 kHz for the same ssDNA sequences used in Figure 3.7.

The difference in the negative DEP spectra shown in figures 3.5, 3.6 3.7 and 3.8 results only from changes in a single nucleotide of the ssDNA sequence. All the other parameters and conditions were not changed throughout the experiments. The narrow error bars shown with plus and minus one standard deviation for a single measurement calculated with six measurements in figures 3.5 and 3.7 are indications of the high accuracy and repeatability of the measurements. Since there was no overlap in the confidence intervals of different curves in figures 3.5 and 3.7, a single measurement is sufficient to determine the type of the last and the second-to-last nucleotide of these ssDNA sequences. Therefore, these results demonstrate the potential use of this method as a label-free transduction mechanism for SNP detection in the last and the second-to-last nucleotides in ssDNA sequences.

With the experiments using the pearl-shaped electrodes, we observed that it was challenging to place the region monitored by the image processing algorithm in the correct location

to measure the velocity of the PM band, and the PM band spreads significantly during negative DEP due to the electrode layout, reducing the accuracy in the measured position of a biotinylated PM band. To address these limitations, we redesigned the electrode layout. The new electrode is explained in section 4.2.1.2. The DEP effect under the new electrode is shown in figure 3.9.

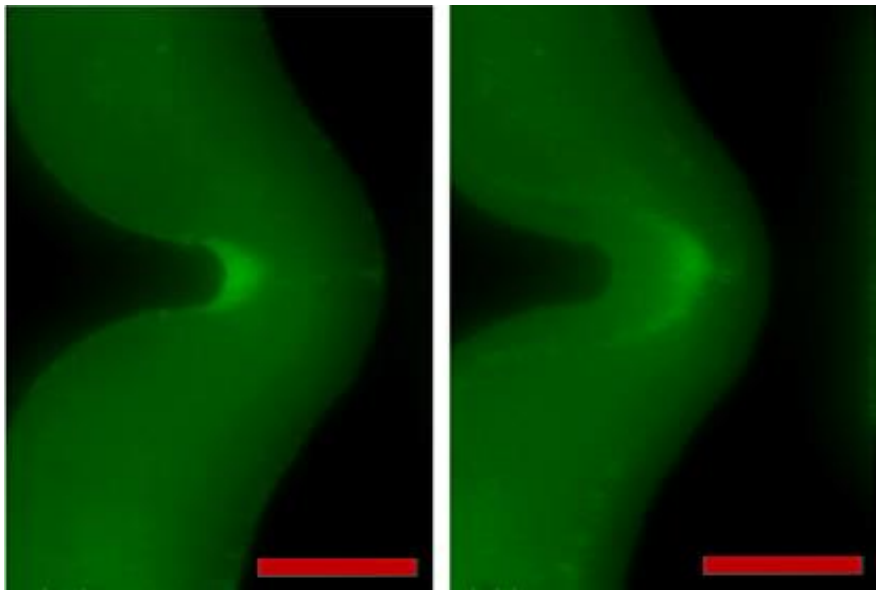

Figure 3.9: Time-lapse images captured through DEP spectroscopy application using the new electrode design with biotinylated PM. The electric field is changed from 10 kHz to 500 kHz with 10 V_{p-p} at) t=0 ms. The images were captured at (Left) t=0 ms and (Right) t=40 ms. The electrode is visible in the darker region. The bright layer visible on the edge of the electrode is formed by the PM. The scale bar represents 50 μm. Methods: Biotinylated PM with 740 nm diameter in 10 μL of 0.01X PBS. For 480 ms before the image (a), a 10 V_{pp} electric field at 10 kHz, which produces positive DEP, was applied to the electrodes. Right after that, the frequency of the electric field increased to 500 kHz.

With this new electrode, the region with a high electric field can be easily acquired through image processing and the PM band moving away from the region with a high electric field due to negative DEP approximately follows an elliptical pattern. We used an image processing algorithm to extract the distribution of the light intensity along with the distance from the convex electrode, in which we integrate all the intensity along an ellipse whose ratio between the major axis and the minor axis is 1.52. These results are shown in figure 3.10 for the case in which the PM is functionalized with single-strand DNA (ssDNA) with sequence 5'-Biotin-TGTTGTGCGA-3'. We

calculated the drift velocity of the PM band by dividing the change of the center of mass of the region with intensity above 2/3 of the peak intensity over the 40 ms interval in which negative DEP was applied. Due to the viscosity of the solution, the DEP force is proportional to the drift velocity of the PM band.

We carried out a sequence of measurements of the drift velocity of a band of PM functionalized with ssDNA with the sequence 5'-Biotin-TGTTGTGCGA-3' and we repeated these measurements with three other almost identical sequences, except that the last nucleotide is replaced with T, C, and G, respectively. These results are shown in figure 3.11 for the frequency range from 1140 kHz to 1285 kHz.

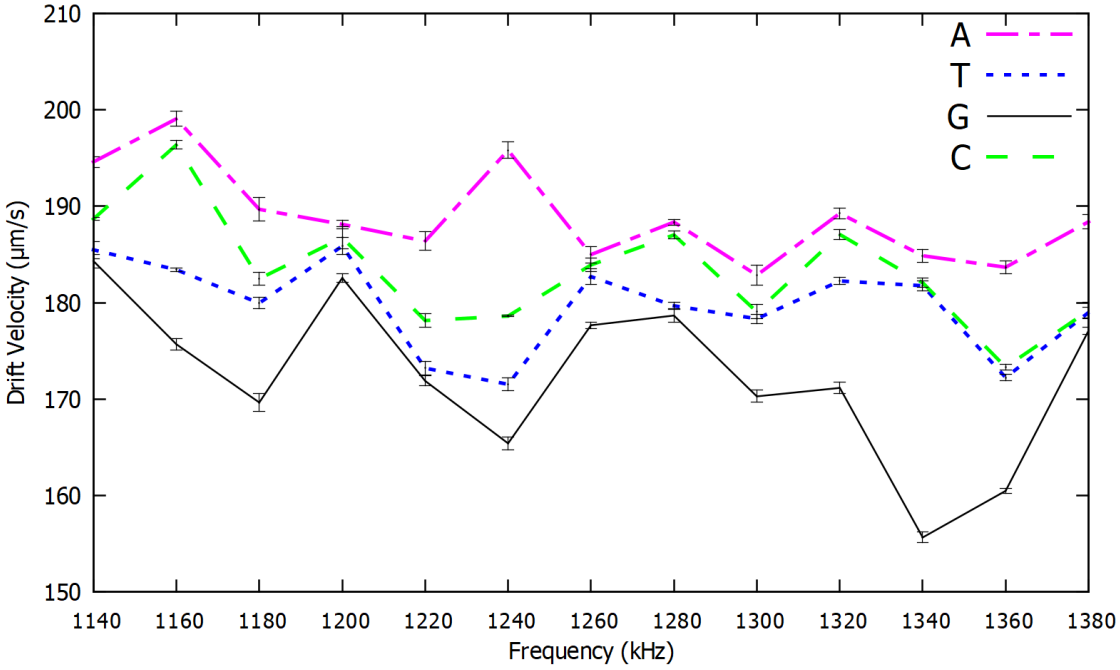

Figure 3.10: Negative DEP Spectrum curves for PM bound to biotinylated ssDNA with 10 nucleotides. The sequence of nucleotides is 5'-Biotin-TGTTGTGCGA-3', 5'-Biotin-TGTTGTGCGT-3', 5'-Biotin-TGTTGTGCGC-3', and 5'-Biotin-TGTTGTGCGG-3'. These sequences only have a difference in the last nucleotide. Methods: PM with 740 nm diameter functionalized with four ssDNA with 10 nucleotides with a difference in the last nucleotide in 10 μL of 0.01X PBS. Each spectral measurement was carried out with all the PM functionalized with one sequence of nucleotides.

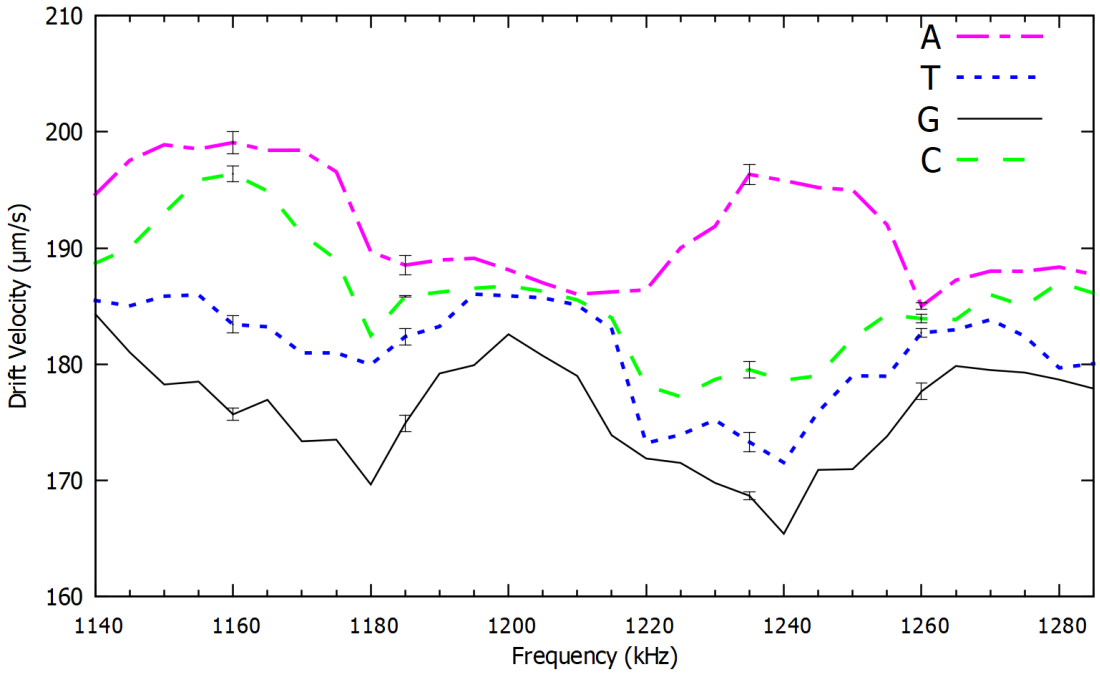

Figure 3.11: High-resolution negative DEP spectra from 1140 kHz to 1285 kHz for the same ssDNA sequences used in figure 3.10.

Each DEP spectrum curve requires only 86 seconds to be obtained during the experiments. We observed a significant difference in the NDEPS when only the last nucleotide in the sequence was changed. The experiment was repeated six times in the frequencies 1160 kHz, 1185 kHz, 1235 kHz, and 1260 kHz to estimate the error in each measurement that was carried out at those frequencies. The error estimated in individual measurements at those frequencies was shown with error bars. A distinct pattern in the NDEPS was observed in the strands of DNA in which only the last nucleotide was changed. The error in individual measurement of the DEP spectrum on those frequencies was significantly lower than the difference in the measurement for different nucleotides. Therefore, the NDEPS is sufficient to determine the last nucleotide in the DNA strands that we investigated.

We used the same image processing algorithm that we applied to obtain the results shown in figure 3.10 to determine the dependence of the NDEPS on the second-to-last nucleotide in a

DNA molecule with 10 nucleotides. One of the DNA molecules was 5'-Biotin-TGTTGTGCAC-3' and two others in which the second-to-last nucleotide A was replaced with the nucleotides T and C. These results are shown in figure 3.12 for the frequency range from 500 kHz to 2000 kHz in steps of 300 kHz and figure 3.13 depicts high-resolution spectra for a frequency range of 1140 kHz to 1285 kHz. Each DEP spectrum curve requires only 86 seconds to be obtained during the experiments.

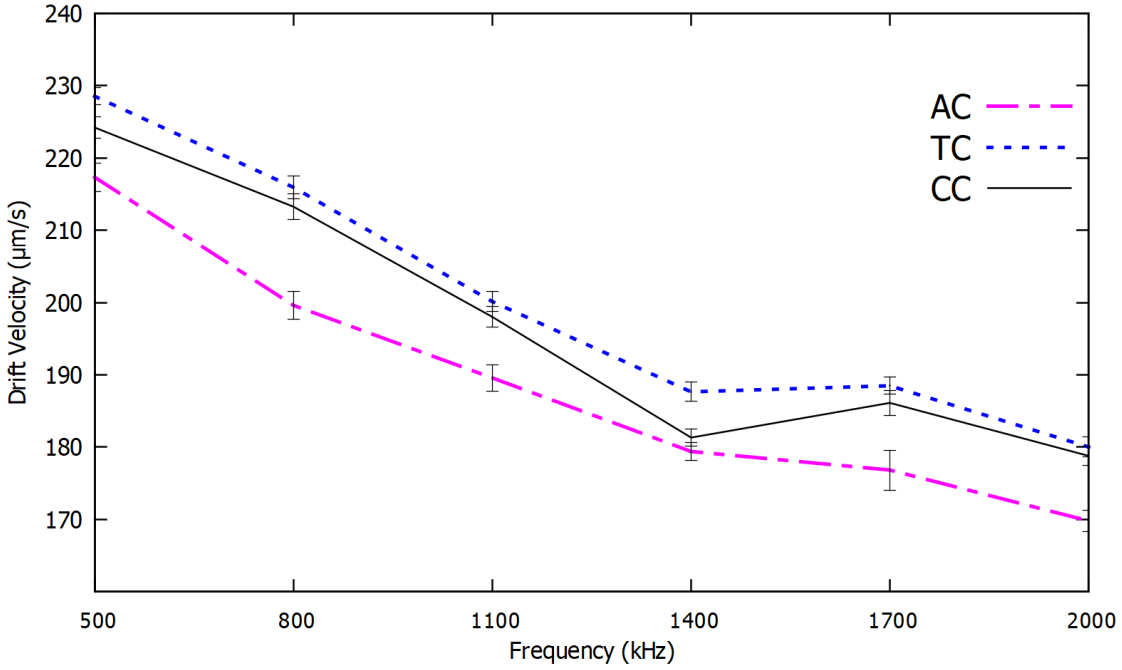

Figure 3.12: Negative DEP Spectrum curves for PM bound to biotinylated ssDNA with 10 nucleotides. The sequence of nucleotides are 5'-Biotin-TGTTGTGCAC-3', 5'-Biotin-TGTTGTGCTC-3', and 5'-Biotin-TGTTGTGCCC-3'. These sequences only have a difference in the second-to-last nucleotide. Methods: PM with 740 nm diameter functionalized with four ssDNA with 10 nucleotides with a difference in the last nucleotide in 10 μL of 0.01X PBS. Each spectral measurement was carried out with all the PM functionalized with one sequence of nucleotides.

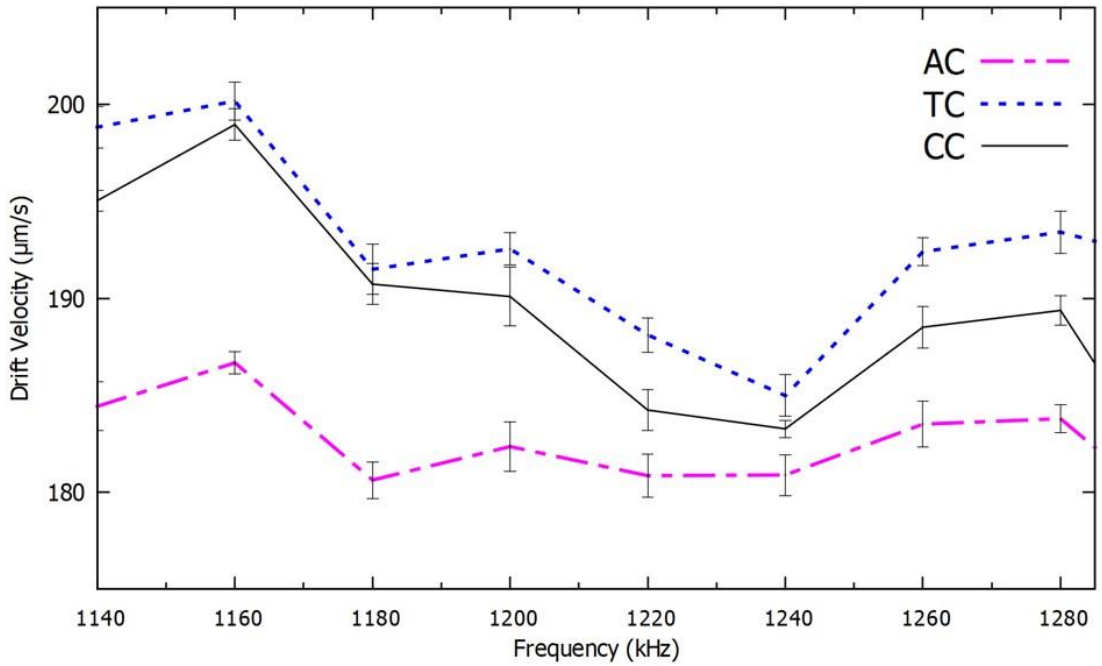

Figure 3.13: High-resolution negative DEP spectra from 1140 kHz to 1285 kHz in steps of 20 kHz for the same ssDNA sequences used in figure 3.12.

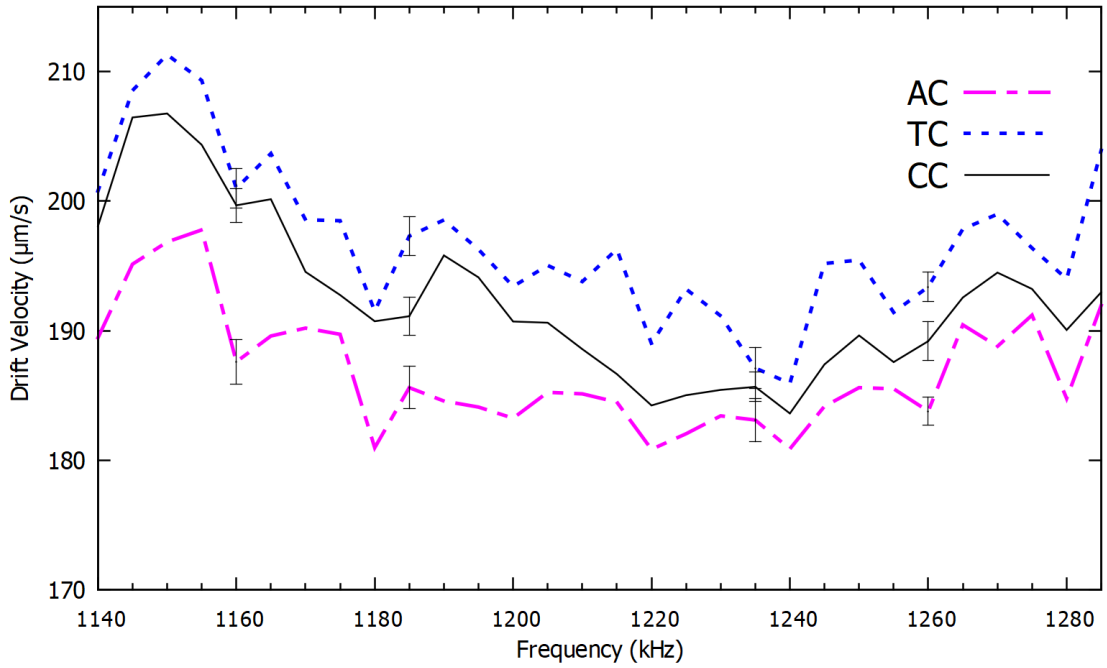

Figure 3.14: High-resolution negative DEP spectra from 1145 kHz to 1285 kHz in steps of 5 kHz for the same ssDNA sequences used in figure 3.12.

We also observed a significant difference in the negative DEP spectrum when the second-to-last nucleotide in the sequence was changed. The error estimated in the frequencies 1160 kHz, 1185 kHz, 1235 kHz, and 1260 kHz were shown with error bars. A distinct pattern in the negative DEP spectrum was also observed in the strands of DNA in which only the second-to-last nucleotide was changed. The error in single measurements of the DEP spectrum is significantly lower than the difference in the DEP spectrum with different nucleotides. Therefore, the NDEPS of these sequences is sufficient to determine the second-to-last nucleotide in the DNA molecules that we investigated.

The DEP spectra are shown in figures 3.5,3.6,3.7,3.10,3.11,3.12,3.13, and 3.14 can be used as the calibration curve for the SNP detection which can pave ways for the diagnosis of genetic variants associated with human diseases.

3.4. Conclusion

We demonstrated that the negative DEP spectroscopy method is an effective transduction method to accurately detect SNPs with which genetic variants causing human diseases can be found. The negative DEP spectrum was measured using a custom-made real-time image processing technique to detect the drift velocity of PM bound to ssDNA in microstructured electrodes since the drift velocity is proportional to the DEP force due to the viscosity of the solution. The frequency-dependent velocity of repulsion due to negative DEP on a set of PM bound to ssDNA, which is a label-free quantity that we measure using image processing, ha a strong dependence on the last and in the second-to-last nucleotides in ssDNA sequences. This technique does not require the use of fluorescent labels, which eliminates the washing step of unbound fluorescent molecules in the preparation process and, consequently, does not requires a careful calibration of the light source and the photodetector sensitivity.

4. DETECTION OF A PROTEIN BIOMARKER BASED ON DIELECTROPHORESIS SPECTROSCOPY[2]

Pancreatic cancer is one of the most fatal forms of cancer malignancies in humans. The surgical procedure remains the only remedial action for this distressing ailment [9]. The average five-year survival rate is 6% with less than one year of average survival time for the patients in the metastasis condition [9], [103]. Hence it is vital to diagnose this condition at its early stage. The fluctuations of the levels of biochemical molecular biomarkers can be nucleic acids, peptides, carbohydrates, or proteins [7].

In our study we examined three potential pancreatic cancer biomarkers namely:

- Carbohydrate antigen (CA) 19-9
- Carbohydrate antigen (CA) 242
- Carcinoembryonic Antigen (CEA)

4.1. Detection of CA 19-9

Carbohydrate antigen (CA) 19-9 is a pancreatic cancer biomarker [104] that received approval by the U.S. Food and Drug Administration (FDA) for the monitoring of pancreatic cancer [22], [105], [106]. A detailed literature review of pancreatic cancer was conducted by [27] and they demonstrated various cutoff levels of CA 19-9 used as a screening tool in asymptomatic patients for the Diagnosis of Pancreatic Cancer. The predictive value of CA 19-9 in the diagnosis of pancreatic cancer rises with its increase in level. Steinberg et al. [107] showed that the

[2] This chapter was extracted from a published article in Chemosensors (F. Dackson Gudagunti, L. Velmanickam, D. Nawarathna, and I. Lima, "Label-Free Biosensing Method for the Detection of a Pancreatic Cancer Biomarker Based on Dielectrophoresis Spectroscopy," Chemosensors, vol. 6, no. 33, pp. 1–10, 2018, doi: 10.3390/chemosensors6030033.). Conceptualization, I. T. Lima and F. D. Gudagunti; Formal analysis, F. D. Gudagunti and L. Velmanickam; Investigation, F. D. Gudagunti and L. Velmanickam; Methodology, F. D. Gudagunti, L. Velmanickam, D. Nawarathna and I. T. Lima; Project administration, I. T. Lima; Writing—original draft, F. D. Gudagunti; Writing—review & editing, L. Velmanickam, D. Nawarathna and I. T. Lima.

percentage of pancreatic cancer incidence level is 72% with CA 19-9 over 37 U/mL. However, when the concentration of CA 19-9 exceeds 1000 U/mL, the probability of incidence of pancreatic cancer rises to more than 97%.

Several techniques have been proposed to detect CA 19-9. Most of the investigative procedures involve CA 19-9 monoclonal antibody 1116-NS-19-9 in recognizing CA 19-9 as an explicit probe [20], [108], [109]. Passerini et al. were the first group to develop a solid-phase radio immunometric sandwich assay that can readily react with a carbohydrate antigenic determinant at low concentrations [108]. This has led to the development of enzyme-linked immunosorbent assay-based techniques using electrochemical assays, photo-electrochemical assays, and fluorescent-based assays [110]. Recent advances have detected CA 19-9 using Raman spectroscopy and surface plasmon resonance [111]. These techniques have drawbacks due to complicated and time-consuming protocols, thus requiring the presence of an expert to handle complex and expensive pieces of equipment. To address the above-mentioned problems, we have developed a biosensor based on DEP to detect CA 19-9. In this chapter, we present a proof of principle of the use of negative dielectrophoresis (DEP) spectroscopy as the transduction mechanism to measure the concentration of CA 19-9 [112].

4.1.1. DEP theory

Exposing a polarizable particle to an electric field will induce electrical charges on the particle. These induced electrical charges will then act upon the dipole to align them parallel to the applied electric field. If this electric field is non-uniform, a net force will be imposed due to uneven Coulomb forces acting upon the dipole. Based on the particle's polarizability in comparison with that of the suspending medium, the particle can move towards or off the region of the applied electric field. This motion is called DEP [56], [113].

Kawabata & Washizu exploited the dependence of the DEP force on the molecular binding on the surface of functionalized PM to separate PM as a function of the molecular binding for alpha-fetoprotein and DNA strands [114]. DEP was also used to concentrate DNA molecules with [115] and without [116] PM.

4.1.2. Materials and methods

4.1.2.1. DEP spectroscopy application

We developed a software application using Microsoft foundation classes in visual C++ for Windows that measures the drift velocity of dielectric particles due to DEP as a function of the frequency of the electric field applied to the interdigitated electrode. The application is integrated with a USB video class (UVC) standard compliant microscope camera, Tektronix AFG series function generators, pearl-shaped interdigitated electrode, OMFL600 low power microscope, and a custom-based optical side illumination technique which is as explained in section 3.2.4.

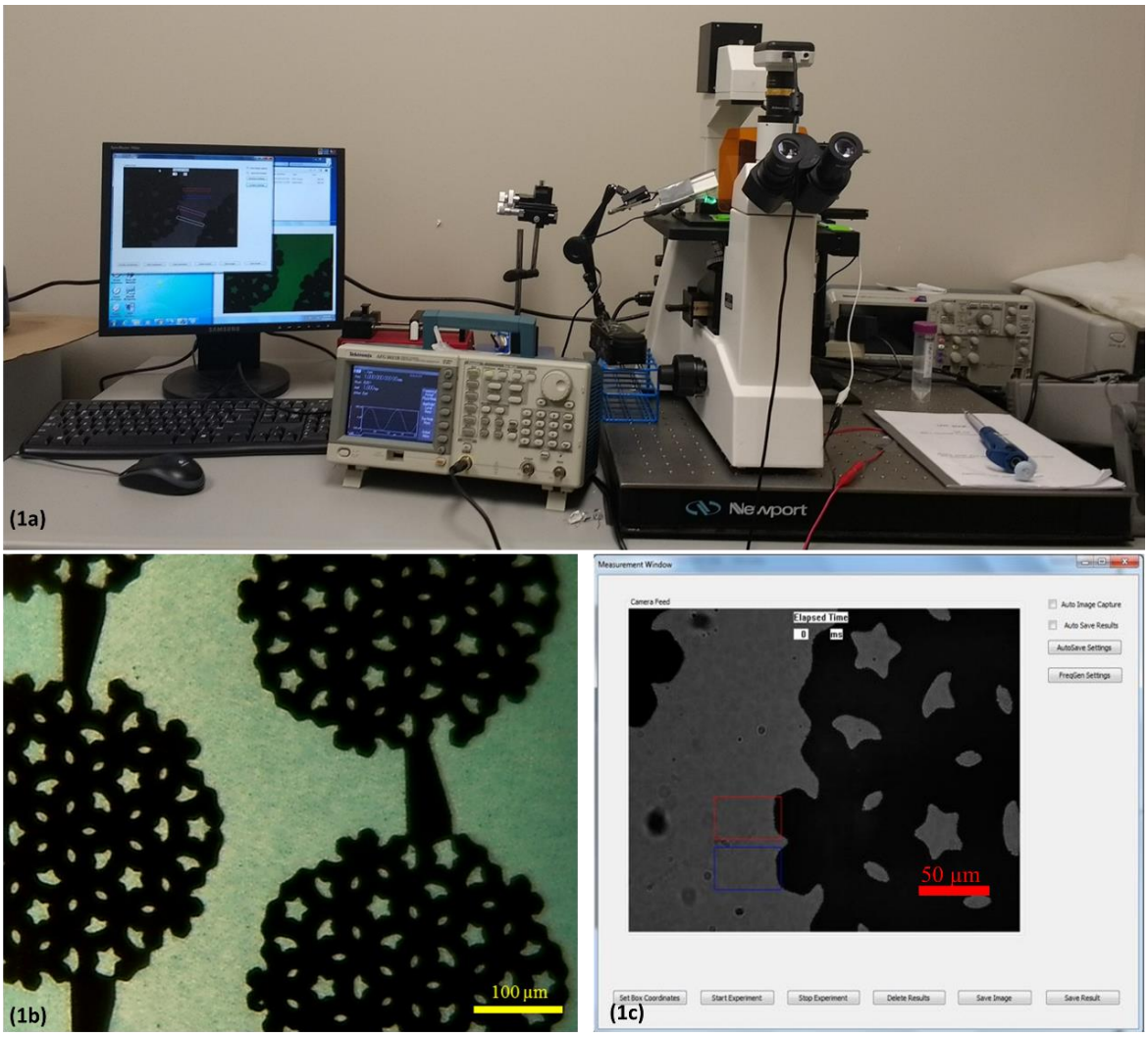

Figure 4.1: (**a**) Experimental setup of the sensor prototype. (**b**) Interdigitated electrodes were used in the experiments. The electrode is visible as the darker region in the picture. Scale bar indicates 100 µm. Multi-colored hollow rectangles depict the regions of interest for measurements and analysis. (**c**) The interface of Microsoft Windows application for dielectrophoresis (DEP) spectroscopy.

4.1.2.2. Sample preparation

The sample preparation consists of the following steps:

- Step 1: Streptavidin attachment to biotinylated PM. Biotinylated PM with 750 nm diameter was purchased from Spherotech Inc. The first step in the preparation of samples consists of binding the biotinylated PM with the antigen Streptavidin purchased from Vector Labs Inc. Biotin acts as a conjugate to the protein Streptavidin

and forms a strong bond with very high affinity. This process is done first by adding a 3 μL Streptavidin solution into a 10 μL biotinylated PM solution in a centrifuge tube to have a 100% binding, according to the manufacturer's recommendation. The total volume was set to 400 μL by adding 0.01× phosphate-buffered saline (PBS) solution with a conductivity of 0.01 S/m. Then, the sample was uniformly mixed using a vortex machine and left on a shaker for 20 min for the Streptavidin–biotin-binding process. After 20 min, the tube was centrifuged at 5000 rpm for 14 min to remove the unbound Streptavidin molecules and the buffer.

- Step 2: Biotinylated CA 19-9 antibody attachment to the biotinylated PM + Streptavidin. Each Streptavidin molecule can bind up to 4 biotin molecules. One binding site of each Streptavidin molecule is used to bind that Streptavidin molecule with the PM. The remaining three Streptavidin binding sites bind with three biotinylated CA 19-9 antibodies. First, 3 μL of biotinylated CA 19-9 antibody was added into 397 μL of 0.01× PBS to have 100% binding of the biotinylated antibodies with all the Streptavidin molecule binding sites, according to the manufacturer requirement. Then this sample was added into the solution with Streptavidin–biotin PM and uniformly mixed using a vortex machine. After that, the sample was kept on a shaker for 20 min for the biotinylated CA 19-9 antibodies to bind with the Streptavidin molecules of the PM. After 20 min, the tube was centrifuged at 5000 rpm for 14 min to remove the unbound biotinylated CA 19-9 antibody molecules and the buffer.
- Step 3: CA 19-9 Antigen attachment to the PM + Streptavidin + CA 19-9 antibody.

  For this process, different concentrations of CA 19-9 Antigen, including 18 U/mL and 37 U/mL, were prepared in a total volume of 400 μL 0.01× PBS buffer. Then, this

sample was added to the centrifuged CA 19-9 antibody-bound PM and mixed uniformly using a vortex machine. After that, the sample was kept on a shaker for 30 min and the sample was centrifuged at 5000 rpm for 14 min to remove the unbound CA 19-9 antigen molecules and the buffer. Finally, 200 µL of 0.01× PBS buffer was added to the centrifuge tube and mixed uniformly.

A schematic representation of the three steps used in the sample preparation is shown in figure 4.2.

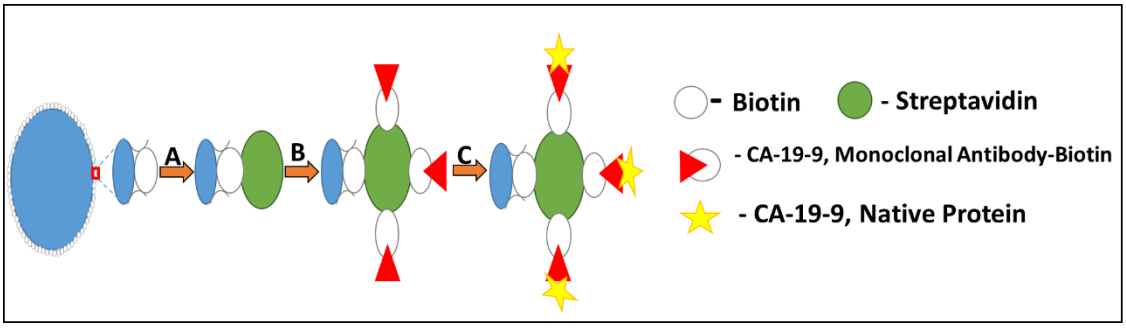

Figure 4.2: Schematic representation of the sample preparation (Biotinylated polystyrene microspheres (PM) + Streptavidin + Biotinylated CA 19-9 Monoclonal Antibody) with the antigen Native Protein CA 19-9, assuming binding in all the available sites of the antibody.

4.1.2.3. Pearl-shaped interdigitated electrode

In the experiments, we used a pearl-shaped interdigitated electrode that was designed and fabricated at North Dakota State University [117]. The electrode was designed and drawn to scale in AutoCAD, validated in COMSOL Multiphysics, and fabricated on commercially available glass wafer using photolithography, metal sputtering, and lift-off procedures using 1000 Å thick gold film in the microfabrication facilities at North Dakota State University. Our electrode can generate a maximum electric field of 1.8×10^4 V/m and gradients as high as 3×10^{12} V^2/m^2, which is sufficient to produce strong DEP forces to dielectric particles with a few hundred nanometers of diameter. It was observed that the root mean square of the electric field and the electric field gradient produced by this electrode do not vary with the frequency from tens of kHz to several

MHz. This ensures the sample is subjected to the same electric field gradient in all frequencies of interest, which makes DEP behavior depend only on the value of the real part of the Clausius–Mossotti factor [118].

4.1.2.4. Illumination setup

An interdigitated electrode, an OMFL600 low power microscope, a Tektronix AFG series function generator, and a custom-built green LED lamp illuminating with 45° of incidence were used in the experiment. This angle of incidence reduces the amount of light collected by the camera that does not result from light scattering from the PM, which is an implementation of dark field microscopy. When 10 µL of the assay was pipetted on the surface of the electrode, a portion of the light scattered from the antigen-bound PM is collected by the objective of the microscope, resulting in a sharp image of the antigen-bound PM. Since the diameter of the antigen-bound PM is of the same order as the wavelength of the green LED (565 nm), the antigen-bound PM appears bright on a dark background due to Mie scattering. Therefore, this is a label-free method, since no fluorescence markers to the target molecules need to be used for the transduction and, consequently, there is no need for a washing procedure to remove the unbound fluorescent markers.

4.1.2.5. Frequency sweep and image processing

Before the drift velocity due to the DEP force can be measured for any frequency, a positive DEP force needs to be applied to attract the PM to the edges of the electrode. Then, negative DEP is applied for a frequency in the frequency range of the spectrum used in the experiment. The software sets the function generator to scan through a set of electrical frequencies. For the experiments that we present here, the lowest frequency was set to 500 kHz, the frequency step was

set to 300 kHz, and the highest frequency was 2 MHz for negative DEP. The peak-to-peak voltage value was set by to10 V.

The time interval for positive DEP was set to 2000 ms and the time interval for negative DEP was set to 80 ms per frequency measurement. The choice of these time intervals was determined after conducting a series of preliminary experiments. In the case of positive DEP, the experiment starts with a certain start frequency f_{pDEP} that induces a positive DEP effect for the specified time interval to collect the PM to a region near the electrode. Then, the frequency is automatically changed to the frequency $f_{\mathrm{nDEP},1}$ that induces a negative DEP effect for the specified time interval, and two images are obtained to measure the center of mass of the PM as they are being repelled from the electrode. Then, the cycle repeats with the waveform generator changing the frequency back to f_{pDEP} to attract the PM to a region near the electrode. After that, the frequency is switched to the next frequency that produces negative DEP $f_{\mathrm{nDEP},2}$. This cycle goes on until f_{nDEP} reaches the stop frequency. The frequency switching by the function generator is done automatically by our application.

The spectrum measurement could also have been designed to measure the drift velocity due to positive DEP as a function of the frequency. However, positive DEP has a narrower frequency range for the dielectric particles that we are using. Moreover, it was easier to automate the measurement of the drift velocity due to negative DEP because the dielectric particles start drifting from the same region near the edge of the electrode at the onset of negative DEP.

4.1.3. Results

We validated our sensing method by carrying out DEP spectroscopy experiments with our image-processing software for observation and recording of the results during the experiments. The validation of the method is shown in figure 4.3. Initially, the software automatically sets the

function generator to the frequency 10 kHz to establish positive DEP. Low-frequency electric fields (<50 kHz) produce positive DEP whereas high-frequency electric fields (>250 kHz) produce negative DEP force to the PM that we use in this study. The positive DEP force results in the attraction of the PM towards the edge of the electrode. A clear PM layer can be seen forming at the edge of the electrode in figure 4.3. Once the PM forms a layer at the edge of the electrode, our software automatically switches the frequency to a preset frequency that produces negative DEP. The negative DEP force pushes the PM from the edge of the electrode. The repulsion of the PM by the electrode is tracked and recorded using our custom-made software. Using this system, we calculated the drift velocity of the PM layer repulsed from the electrode, which is proportional to the DEP force, as they move away from the electrode edge using image processing.

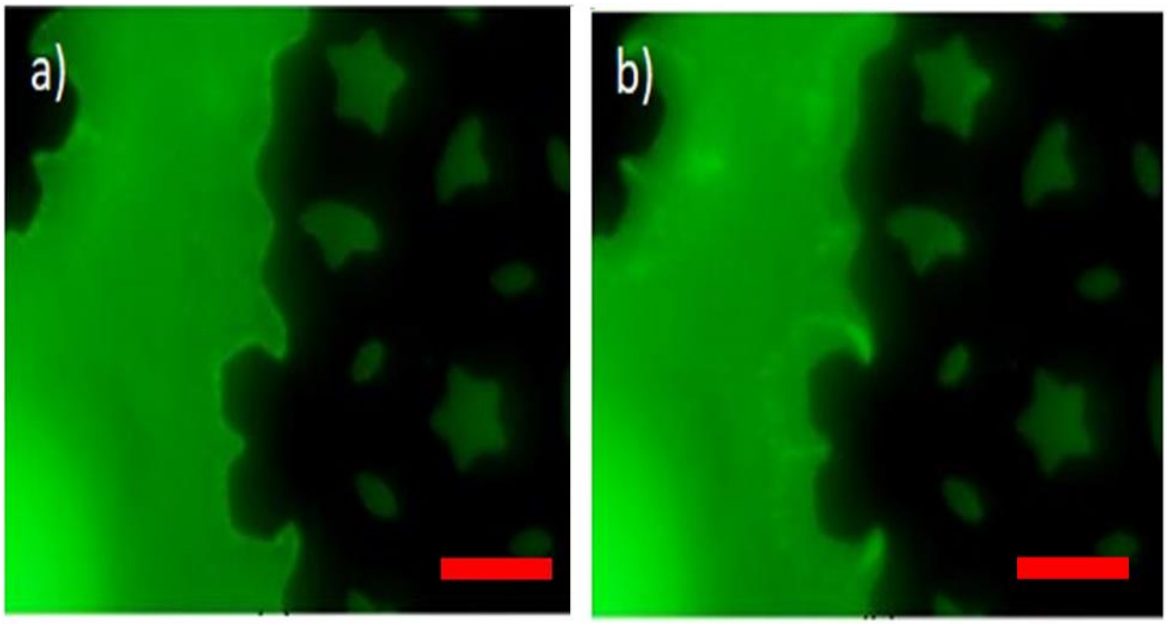

Figure 4.3: Demonstration of negative DEP effect through time-lapse images captured through the DEP spectroscopy application (Assuming $t = 0$ when electric field frequency is changed to induce negative DEP): (**a**) $t = 0$ ms and (**b**) $t = 80$ ms. The concentration of CA 19-9 in this solution is 37 U/mL. The interdigitated electrode is visible as a darker region in the picture. The bright layer visible on the edge of the electrode is formed by the accumulation of the sample. As the frequency is changed to induce negative DEP the antigen-bound PM is repelled from the electrode. For 60 s before the image (**a**), a 10 V peak-to-peak electric field at 10 kHz, which produces positive DEP, was applied to the electrodes. Then, the frequency of the electric field increased to 500 kHz, producing negative DEP. The scale bar on both figures indicates 50 µm.

The system tracks the variation of the light intensity along the major axis of the box enclosing the region of interest, which is shown in figure 4.1a, at different time intervals, as shown in figure 4.4 for 37 U/mL in 10 µL. The center of mass of the light intensity observed in the image corresponds to the average location of the PM. We process two images to calculate the speed of repulsion: The first image is captured shortly after negative DEP is applied and the second image is captured 80 ms later. The center of the mass of the light intensity is calculated for both images and is used to calculate the speed of the repulsion due to negative DEP.

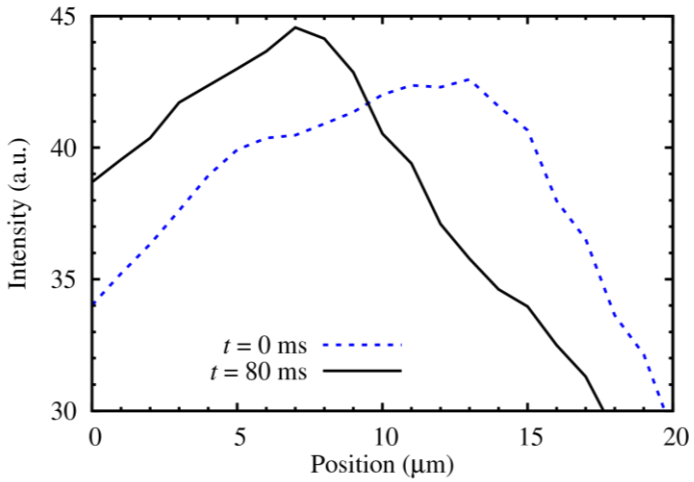

Figure 4.4: Light intensity versus pixel position at t = 0 ms, when negative DEP is applied, and at t = 80 ms for the 37 U/mL in 10 µL. The electrode is located on the right side of the PM layer, as shown in figure 4.3.

We observed a relationship between the speeds of repulsion of the PM functionalized with CA 19-9 antibody as a function of both the frequency and the concentrations of the target CA 19-9 that we considered. As we switched to higher frequency electric fields from our software, we observed a clear dependence of the negative DEP spectrum on the concentration of the target CA 19-9 in the sample. While switching the frequency, we maintained all other experiment parameters and conditions constant. The obtained DEP spectroscopy results are shown in figure 4.5. In this figure, we show the drift velocity of the center of mass of the PM layer as a function of the

frequency for a single measurement. We also show error bars with the standard deviation obtained in six measurements, which is an indication of the confidence interval in each measurement. Since there is very little overlap between the confidence intervals of these curves, only one measurement of the DEP spectrum is needed in each experiment to accurately determine the cutoff level of CA 19-9. These results indicate that this label-free method has the potential to be used as the transduction mechanism to measure the cutoff levels of CA 19-9 that can be used for the diagnosis and monitoring of pancreatic cancer. Therefore, figure 4.5 can be used as the calibration curve for the diagnosis of pancreatic cancer in the early stage and the disease monitoring during treatment.

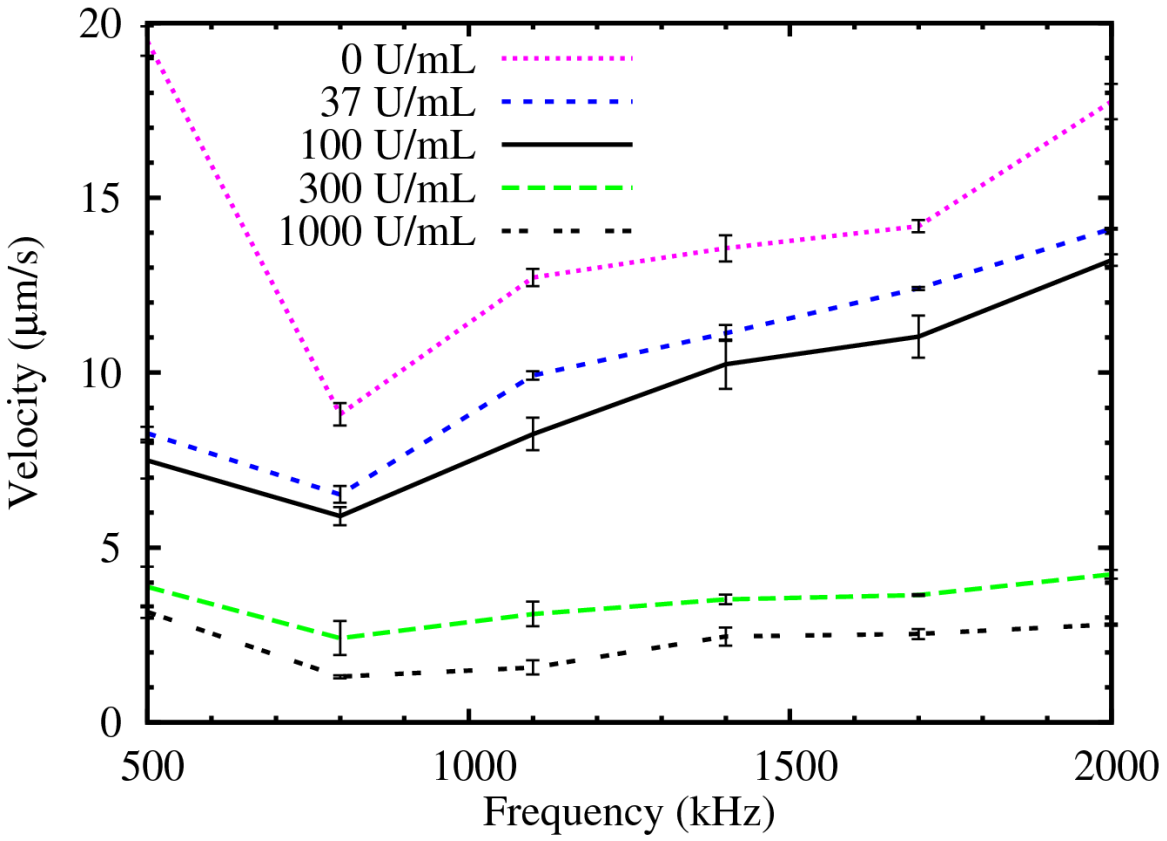

Figure 4.5: Negative DEP spectrum curves for cutoff levels of CA 19-9 for the detection of pancreatic cancer at 0 U/mL, 37 U/mL,100 U/mL, 300 U/mL, and 1000 U/mL. The error bars show the confidence interval in each measurement that was calculated using six measurements per frequency.

In Figure 4.6, we show the results of the drift velocity due to negative DEP as a function of the concentration of CA 19-9 for three different frequencies. We observed that that the drift velocity due to DEP is strongly dependent on both the frequency and the concentration of CA 19-9 in the cutoff levels that are useful in the prognosis of pancreatic cancer.

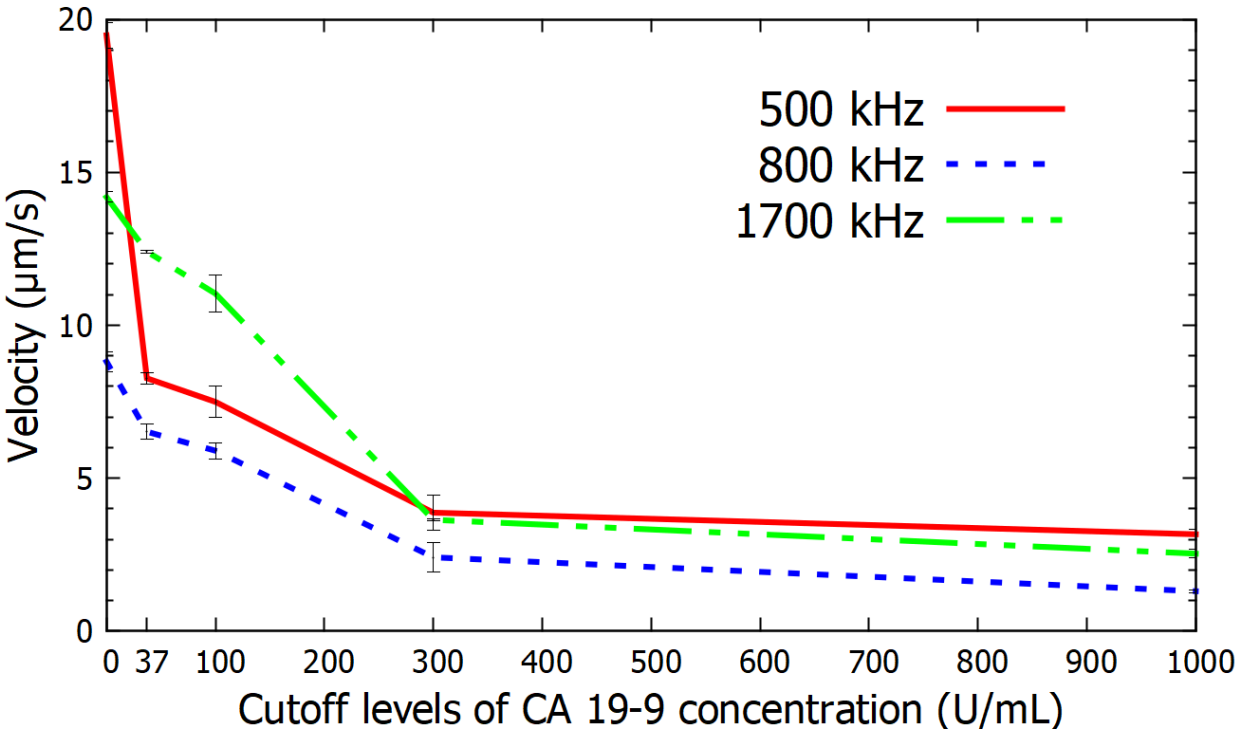

Figure 4.6: Variation of the drift velocity due to negative DEP with the cut-off levels of concentration of CA 19-9 for the frequency range at 500 kHz, 800 kHz, and 1700 kHz.

4.1.4. Discussion

In this chapter, we demonstrated that negative DEP spectroscopy can be used as the transduction mechanism to accurately detect the concentration of CA 19-9, which is a pancreatic cancer biomarker. We measured the negative DEP spectrum using real-time image processing to detect the velocity in which dielectric spheres functionalized with monoclonal antibody to CA 19-9 are repelled by an interdigitated electrode array due to DEP as a function of the frequency. We showed that DEP spectroscopy has sufficient sensitivity to detect the various cutoff levels of CA

19-9 that can enable this method to be used in the diagnosis and the monitoring of pancreatic cancer. The drift velocity due to negative DEP was calculated for the frequency range from 500 kHz to 2000 kHz. PM with 750 nm diameter was imaged using a side illumination technique to detect the Mie scattering produced by the PM. The change in the DEP spectrum with the binding of even a small concentration of CA 19-9 to the conjugated antibody binding sites on the PM arose from the changes in the distribution of the ions from the solution close to the PM surfaces in the presence of the target molecules. Therefore, there is no need to use fluorescent labels conjugated to CA 19-9 to detect the presence of the target molecules. The use of fluorescent labels, on the other hand, not only requires a washing phase to remove the unbound fluorescent molecules, but the quantification of the concentration with that method also requires a careful calibration of the light source and the photodetector sensitivity. Since the measurement using negative DEP spectroscopy is based on the drift velocity of the particles due to DEP as a function of the frequency of the external electric field, this measurement does not depend on the light intensity, the number of PM, and the sensitivity of the camera, as long as the experimental setup enables the calculation of the center of mass of the PM.

We demonstrated that DEP spectroscopy is an effective label-free transduction mechanism for the detection of the cutoff levels of the pancreatic cancer biomarker CA 19-9 in PBS buffer. The velocity of repulsion due to DEP on a set of PM functionalized to a monoclonal antibody to CA 19-9 was measured at 0 U/mL, 37 U/mL,100 U/mL, 300 U/mL, and 1000 U/mL concentration cutoff levels of CA 19-9 at the frequency range from 0.5 to 2 MHz. The proposed method is an effective transduction mechanism for the detection of the cutoff levels of CA 19-9, which can be used in the early-stage diagnosis and the prognosis of pancreatic cancer.

4.2. Detection of Carcinoembryonic Antigen

4.2.1. Introduction

Carcinoembryonic antigen (CEA) [119], [120], a tumor marker, is expressed in normal mucosal cells and overexpressed in adenocarcinoma, especially in pancreatic cancer and colorectal cancer. Although CEA alone cannot be used as a potential biomarker, it complements well with the other FDA-approved biomarkers such as Carbohydrate antigen (CA) 19-9. With the combination of detecting CA 19-9, CEA, and CEA, the specificity of the combined test is at 90%. In this study, we demonstrate a transduction mechanism using negative dielectrophoresis spectroscopy to detect the levels of CEA in serum that are relevant in the diagnosis of pancreatic cancer.

4.2.2. Materials and methods

4.2.2.1. Sample preparation

The sample preparation involved attaching Streptavidin to biotinylated PM. To this, the biotinylated CEA antibody was attached and later the native protein of CEA was attached based on the assumptions of binding all the available sites of the antibody. For this study, we spiked the concentrations of CEA using Bovine Albumin serum (BSA). The BSA was diluted using DI water at a concentration of 0.1 g/L. With 20U/ml being the cutoff levels for the early detection of CEA we choose to prepare the concentration levels at 10 U/ml, 20 U/mL, 40 U/mL, and 0 U/mL. The 0 U/mL is a control group sample without the native antigen of CEA attached.

The antibody and antigen of CEA were commercially purchased from MyBioSource. From the datasheet, we found the concentration of the sample was at 15k U/mL.

- Step 1: Streptavidin attachment to biotinylated PM. Biotinylated PM with 750 nm diameter was purchased from Spherotech Inc. The first step in the preparation of

samples consists of binding the biotinylated PM with the antigen Streptavidin purchased from Vector Labs Inc. Biotin acts as a conjugate to the protein Streptavidin and forms a strong bond with very high affinity. This process is done first by adding a 3 μL Streptavidin solution into a 10 μL biotinylated PM solution in a centrifuge tube to have a 100% binding, according to the manufacturer's recommendation. The total volume was set to 400 μL by adding 0.1× BSA solution. Then, the sample was uniformly mixed using a vortex machine and left on a shaker for 20 min for the Streptavidin–biotin-binding process. After 20 min, the tube was centrifuged at 5000 rpm for 14 min to remove the unbound Streptavidin molecules and the buffer.

- Step 2: Biotinylated CEA antibody attachment to the biotinylated PM + Streptavidin. Each Streptavidin molecule can bind up to 4 biotin molecules. One binding site of each Streptavidin molecule is used to bind that Streptavidin molecule with the PM. The remaining three Streptavidin binding sites bind with three biotinylated CEA antibodies. First, 3 μL of biotinylated CEA antibody was added into 397 μL of 0.01× BSA to have 100% binding of the biotinylated antibodies with all the Streptavidin molecule binding sites, according to the manufacturer requirement. Then this sample was added into the solution with Streptavidin–biotin PM and uniformly mixed using a vortex machine. After that, the sample was kept on a shaker for 20 min for the biotinylated CEA antibodies to bind with the Streptavidin molecules of the PM. After 20 min, the tube was centrifuged at 5000 rpm for 14 min to remove the unbound biotinylated CEA antibody molecules and the buffer.

- Step 3: CEA Antigen attachment to the PM + Streptavidin + CEA antibody.

  For this process, different concentrations of CEA Antigen, including 18 U/mL and 37 U/mL, were prepared in a total volume of 400 μL 0.01× BSA buffer. Then, this sample was added to the centrifuged CEA antibody-bound PM and mixed uniformly using a vortex machine. After that, the sample was kept on a shaker for 30 min and the sample was centrifuged at 5000 rpm for 14 min to remove the unbound CEA antigen molecules and the buffer. Finally, 200 μL of 0.01× BSA buffer was added to the centrifuge tube and mixed uniformly.

4.2.2.2. Interdigitated microelectrode

The direction of movement for the dielectric particle due to DEP depends upon the relative polarizability of the particle and the medium and on the presence of a large gradient of the electric field intensity produced by electrodes. In this experiment, we used the second-generation electrode that was designed and fabricated at North Dakota State University.

Using PIDE electrodes, we observed no variation on the root mean square of the electric field and the electric field gradient produced by this electrode for a frequency ranging from several kHz to a few MHz. One of the drawbacks of using the previously used pearl Shaped Interdigitated Electrode is that the polystyrene microspheres (PM) concentration varies for every cycle of positive and negative DEP. This is because there is gradient applied on each side, thus those PM which experiences the negative DEP may not be repelled back for the positive DEP completely.

The new electrode is designed in such a way that there is always a concave electrode edge, which produces a low electric field gradient near the electrode edge, on the opposite side of the convex electrode edge, which produces a high electric field gradient. Therefore, most of the PM exposed to the electric field gradient will be concentrated near the same convex edge of the

electrode in every cycle in which positive DEP is applied. The new electrode is designed in such a way that on one side of the array there is the electrode edge and on the opposite side, there is a concave structure with no sharp edges. With no sharp edges, the concave structure would have very minimal or no DEP acting on it. With the new electrode, the PM that experiences the positive DEP would attract on the edge of the electrode, and during the negative DEP, it will be repelled away from the edge of the electrode. In the next cycle of frequency, the same set of PMs will be attracted back to the edge of the electrode as there is no or very minimal gradient on the concave structure. This made the lab experiments more robust, helped maintain uniformity, and also optimized the experiment time.

A depiction of the electrode design using AUTOCAD is shown in figure 4.7.

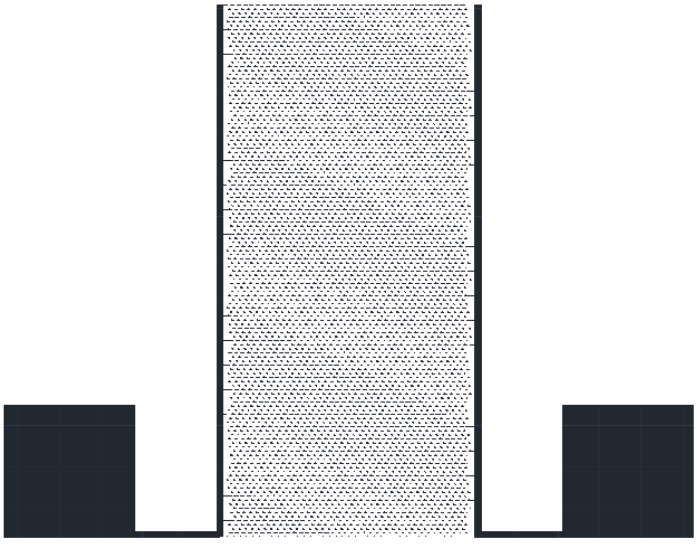

Figure 4.7: Dimensions of the designed electrode (a) 2x3 electrode

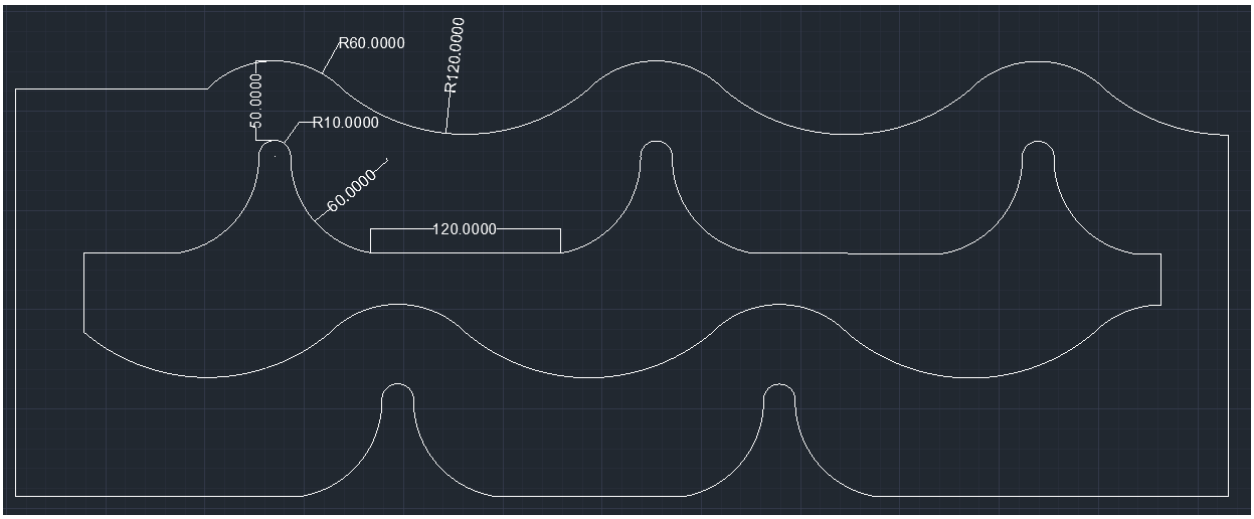

Figure 4.8: Dimensions of the designed electrode (a) 2x3 electrode

The electrode array has a $25 \times 25 = 625$ region of interest so that most of the PM exposed to the electric field gradient will be concentrated near the same convex edge of the electrode in every cycle in which positive DEP is applied.

The electrode tip has a radius of curvature of 10 μm. The distance between the edges of the electrode to the tip of the concave surface is 50 μm. The base of the electrode tip curves at a radius of 60 μm. The base of the electrodes is separated by 120 μm. The curvature of the concave surface is 60 μm. The concave surface is separated by each other by a curvature whose radius is 120 μm. Five electrodes were designed to fit within the wafer of diameter 100 mm which is as shown in figure 4.9.

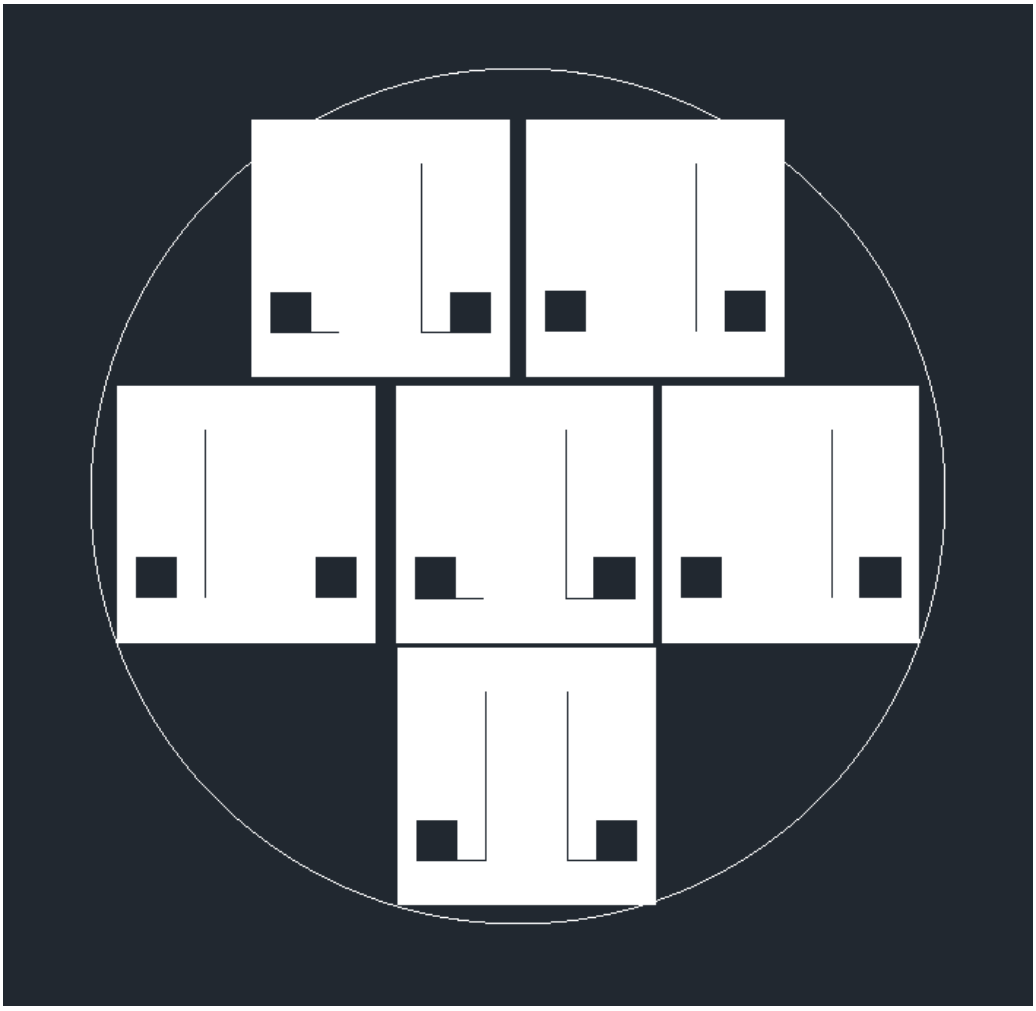

Figure 4.9: Five electrodes designed to fit within a 100 mm wafer.

Using COMSOL we verified that this electrode produces electric field intensities as high as 10^4 V/m and a gradient of the electric field intensity as high 10^{16} V^2/m^3, which is enough to produce strong DEP forces to dielectric particles with a few hundred nanometers of diameter. It was observed that the root mean square of the electric field and the electric field gradient produced by this electrode do not vary with the frequency from tens of kHz to several MHz. This ensures the sample is subjected to the same electric field gradient in all frequencies of interest, which makes DEP behavior depend only on the value of the real part of the Clausius–Mossotti factor [121].

The electric field gradient was measured using a 2D model of COMSOL. The initial design was drawn using AUTOCAD in .dfx file format as shown in figure 4.8 and then imported into COMSOL 2D simulation. The module used for the simulation was AC/DC with a submodule of electric current (EC). The measurement was set to micrometers in the geometry tab. The boundary was set by drawing a rectangle around the electrode design. Using the materials section Gold and Glass were selected on the electrode. Water was used as the surrounding medium with conductivity set to 0.005 S/m and permeability set to 83. Respectively the conductivity of Gold was set to 4.10 $\times 10^7$ and copper to 5.96 $\times 10^7$. The potential is set to be 10 V and is set to the inner array of the electrode, and the ground is set to the outer array of the electrode. We selected extremely fine in the mesh section to improve our modeling workflow. The study frequency was set to 120 kHz. The magnitude of the electric field gradient was calculated using the following formula using the variable *ec.normE* in COMSOL:

$$|\nabla \boldsymbol{E}| = \sqrt{\left(\frac{d(ec.normE^2)}{dx}\right)^2 + \left(\frac{d(ec.normE^2)}{dy}\right)^2}.$$

The electric field gradient was calculated at 1×10^{16} V/m^3 which is good enough to produce strong DEP forces to dielectric particles with a few hundred nanometers of diameter. The simulation results are as shown in figure 4.10.

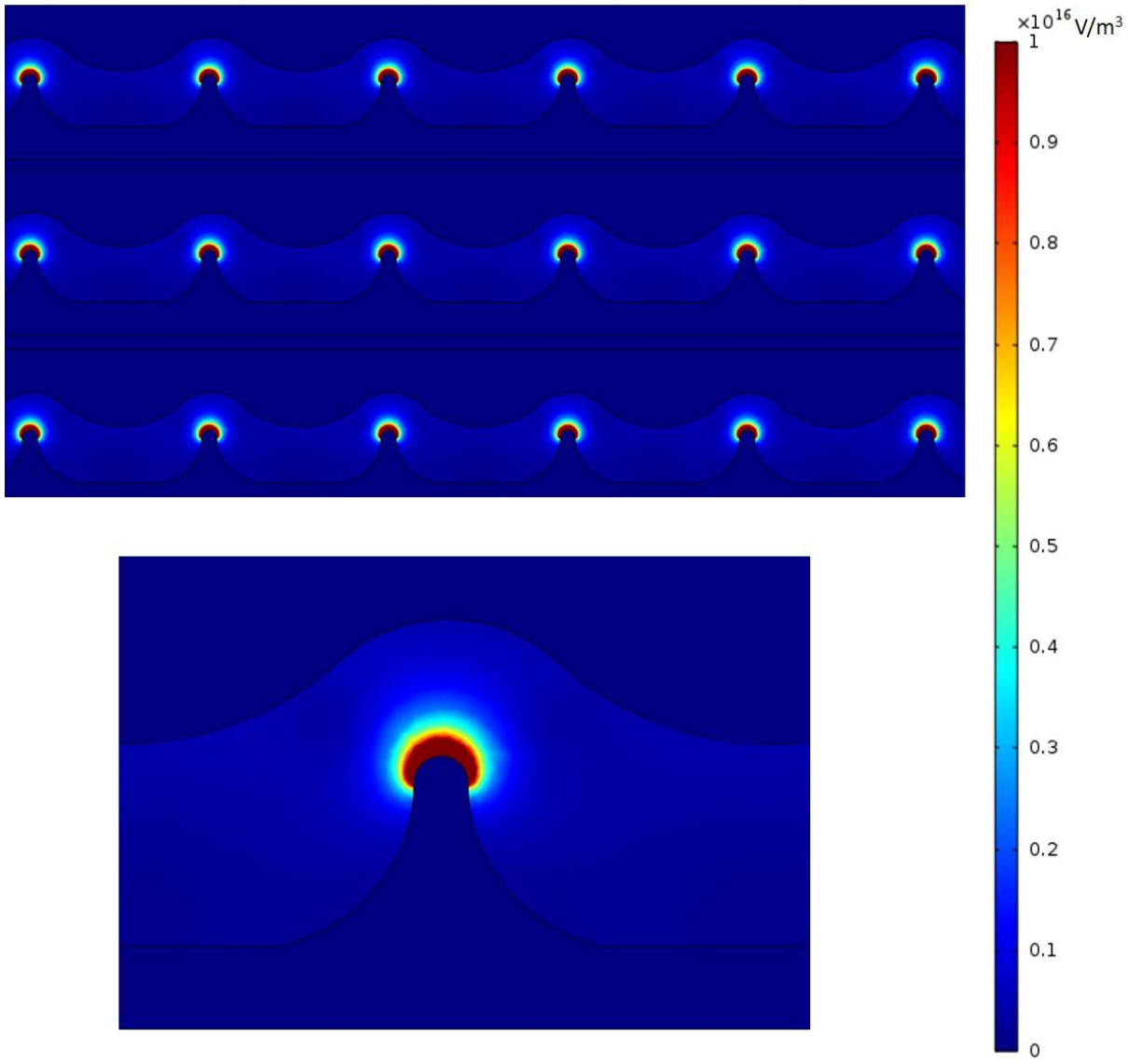

Figure 4.10: (a) Electric field gradient on the array of the electrodes (b) Electric field gradient on the single electrode.

The application of positive DEP attracted the PM on the edge of the electrodes and the application of negative DEP repelled the PM away from the electrode edge. Figure 3.a shows the PM lining on the edge of the electrode with positive DEP acting on it up to 0 ms until negative DEP is applied. Figures 3.b and 3.c depict the repulsion of the PM away from the electrode due to negative DEP at 40 ms and 80 ms.

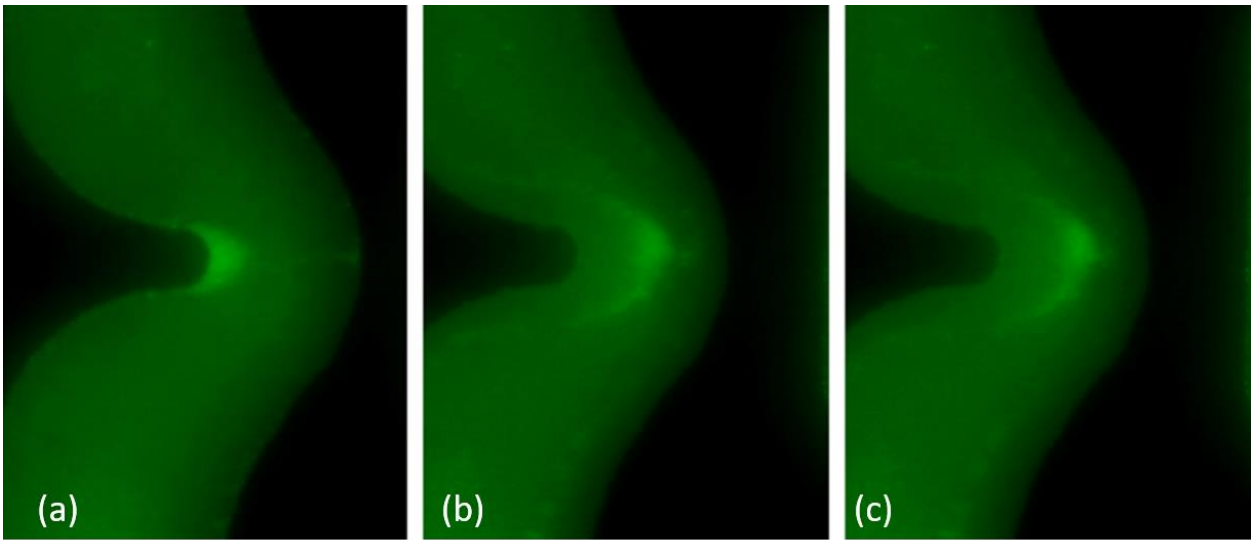

Figure 4.11: Experimental Demonstration of negative DEP effect through time-lapse images captured through DEP spectroscopy application. The electric field is changed from 10 kHz to 500 kHz with 10 Vp-p at t = 0 ms. (a) t = 0 ms and (b) t = 40 ms. (c) t = 80 ms. The interdigitated electrode is visible as a darker region in the picture. The bright layer visible on the edge of the electrode is formed by the accumulation of the sample.

The distribution of the PM traces the shape of an ellipse. The PM accumulation and repulsion forces are higher at the major axis (b1 and b2 as shown in figure 4) in comparison to the accumulation and repulsion at the minor axis (a1 and a2 as shown in figure 4). This is explained in figure 4. The software developed using Microsoft foundation classes in Visual C++ for Microsoft operating system measures the drift velocity of dielectric particles due to DEP as a function of the frequency of the electric field applied to the interdigitated electrode. In the previous version, the raster scan happens for each row and column of the region of interest. With the new electrode as we observed the PM tracing the shape of an ellipse the software scan pattern will be radial.

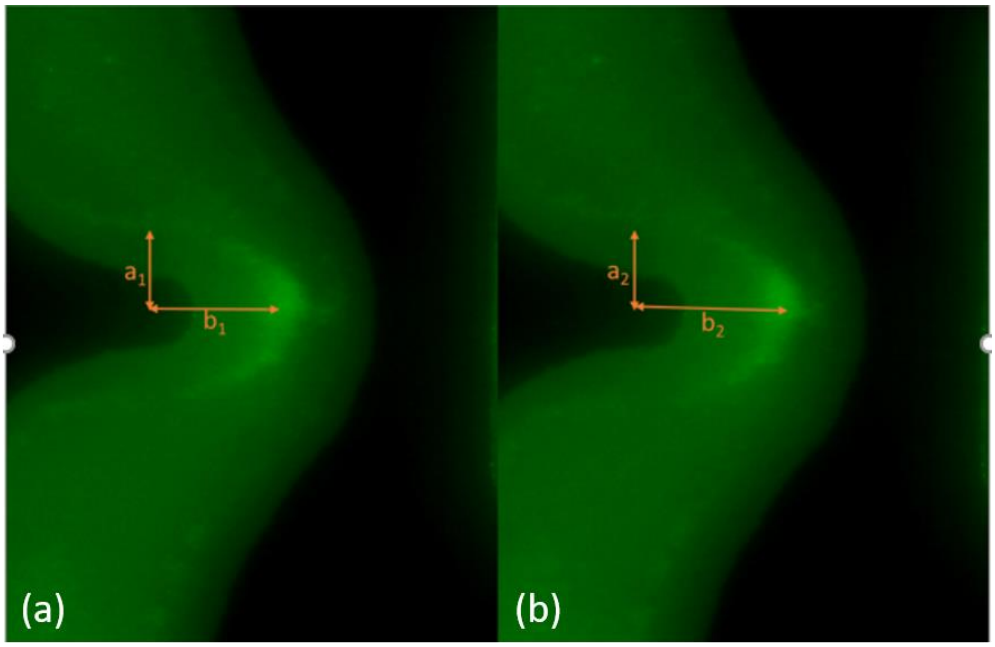

Figure 4.12: Pm distribution pattern tracing the shape of an ellipse. b1 is the major axis and a1 being the minor axis. (a) at t = 40 ms. (b) at t = 80 ms.

4.2.2.3. Frequency sweep and image processing

To measure the drift velocity of the PM functionalized with antibody to CEA as a function of the frequency of the electric field due to DEP, we developed a software application based on Microsoft foundation classes in C++.

In the previous version, the raster scan happened for each row and column of the region of interest. With the new electrode as we observed the PM tracing the shape of an ellipse the software scan pattern will be radial. The application, frequency sweep, and image processing methods are the same as used in section 4.2.1.3.

4.2.3. Results

We observed a relationship between the speed of repulsion of the PM functionalized with CEA antibody as a function of both the frequency and the concentrations of the target CEA that we considered.

While switching the frequency, we maintained all other experiment parameters and conditions constant. The DEP spectroscopy results obtained are shown in figure 4.13. In this figure, we show the drift velocity of the center of mass of the PM layer as a function of the frequency for a single measurement.

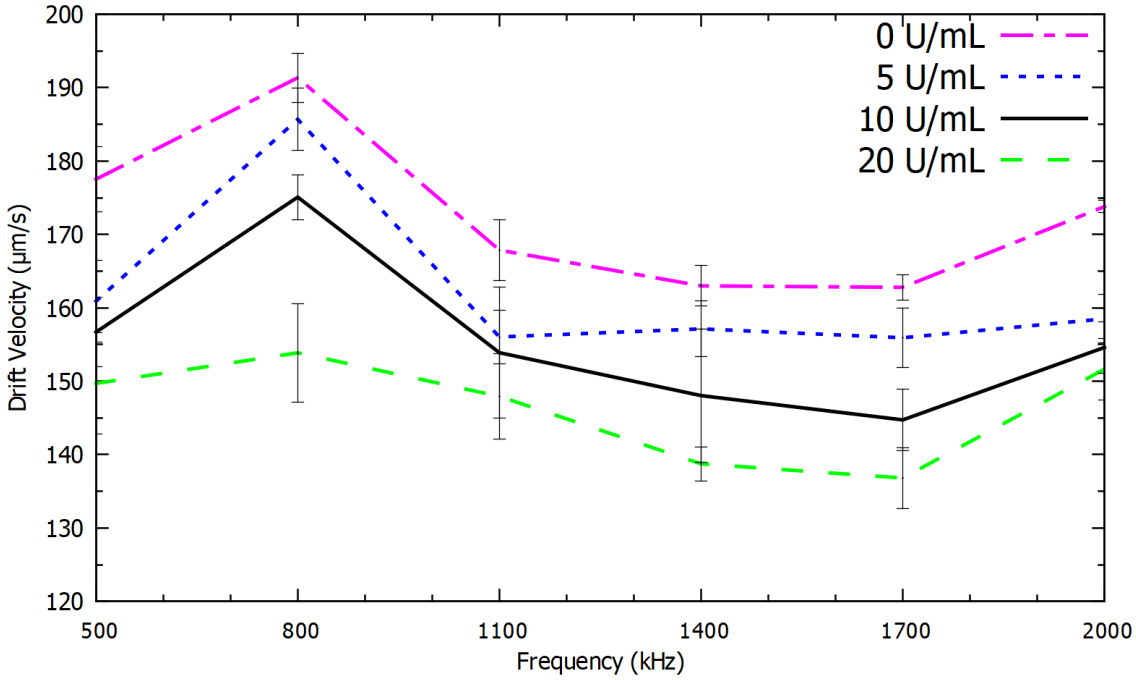

Figure 4.13: Negative DEP spectrum for the various concentration levels of CEA.

We also show error bars with the standard deviation obtained in six measurements, which is an indication of the confidence interval in each measurement. Since there is very little overlap between the confidence intervals of these curves, only one measurement of the DEP spectrum was needed in each experiment to accurately determine the cutoff level of CEA. These results indicate that this label-free method has the potential to be used as the transduction mechanism to measure the cutoff levels of CEA that can be used as an additional detection for the diagnosis and monitoring of pancreatic cancer.

4.3. Detection of CA 242

4.3.1. Introduction

Carbohydrate antigen (CA) 242 is a potential biomarker complementing FDA approved biomarker, CA 242 in the early detection of pancreatic cancer. Cancer Antigen (CA) 242 is a complementary protein biomarker of pancreatic cancer.

The diagnostic rate of pancreatic cancer increases by detecting the combination of CA 19-9, CA 242, and CEA. Table 4.1 shows the sensitivity and specificity for the combination of pancreatic cancer biomarker tests. In this section, the details of the detection of CA 242 are explained.

Table 4.1: Sensitivity and specificity for the combination of pancreatic cancer biomarker test [122].

Biomarkers	Sensitivity (%)	Specificity (%)
Parallel Combination		
CA19-9+CA242	89	75
CA19-9+CEA	85	71
CA242+CEA	76	71
CA19-9+CA242+CEA	90	64
Serial combination		
CA19-9+CA242	66	87
CA19-9+CEA	52	80
CA242+CEA	58	89
CA19-9+CA242+CEA	50	93

The optimal cut-off levels of CA 242 in the serum that can be used in the early detection of pancreatic cancer is 20 U/mL [123]. The sensitivity and specificity for this biomarker are at 81%. CA 242 when detected with CA 19-9 the specificity increases to 87%.

4.3.2. Materials and methods

4.3.2.1. Sample preparation

The sample preparation involved attaching Streptavidin to biotinylated PM. To this, the biotinylated CA 242 antibody was attached and later the native protein of CA 242 was attached based on the assumptions of binding all the available sites of the antibody. For this study, we spiked the concentrations of CA 242 using Bovine Albumin serum (BSA). The BSA was diluted using DI water at a concentration of 0.1 g/L. With 20U/ml being the cutoff levels for the early detection of CA 242 we choose to prepare the concentration levels at 10 U/ml, 20 U/mL, 40 U/mL, and 0 U/mL. the 0 U/mL is a control group sample without the native antigen of CA 242 attached.

The antibody and antigen of CA 242 were commercially purchased from MyBioSource. From the datasheet, we found the concentration of the sample was at 15k U/mL.

- Step 1: Streptavidin attachment to biotinylated PM. Biotinylated PM with 750 nm diameter was purchased from Spherotech Inc. The first step in the preparation of samples consists of binding the biotinylated PM with the antigen Streptavidin purchased from Vector Labs Inc. Biotin acts as a conjugate to the protein Streptavidin and forms a strong bond with very high affinity. This process is done first by adding a 3 μL Streptavidin solution into a 10 μL biotinylated PM solution in a centrifuge tube to have a 100% binding, according to the manufacturer's recommendation. The total volume was set to 400 μL by adding 0.1× BSA solution. Then, the sample was uniformly mixed using a vortex machine and left on a shaker for 20 min for the Streptavidin–biotin-binding process. After 20 min, the tube was centrifuged at 5000 rpm for 14 min to remove the unbound Streptavidin molecules and the buffer.

- Step 2: Biotinylated CA 242 antibody attachment to the biotinylated PM + Streptavidin. Each Streptavidin molecule can bind up to 4 biotin molecules. One binding site of each Streptavidin molecule is used to bind that Streptavidin molecule with the PM. The remaining three Streptavidin binding sites bind with three biotinylated CA 242 antibodies. First, 3 μL of biotinylated CA 242 antibody was added into 397 μL of 0.01× BSA to have 100% binding of the biotinylated antibodies with all the Streptavidin molecule binding sites, according to the manufacturer requirement. Then this sample was added into the solution with Streptavidin–biotin PM and uniformly mixed using a vortex machine. After that, the sample was kept on a shaker for 20 min for the biotinylated CA 242 antibodies to bind with the Streptavidin molecules of the PM. After 20 min, the tube was centrifuged at 5000 rpm for 14 min to remove the unbound biotinylated CA 242 antibody molecules and the buffer.
- Step 3: CA 242 Antigen attachment to the PM + Streptavidin + CA 242 antibody. For this process, different concentrations of CA 242 Antigen, including 18 U/mL and 37 U/mL, were prepared in a total volume of 400 μL 0.01× BSA buffer. Then, this sample was added to the centrifuged CA 242 antibody-bound PM and mixed uniformly using a vortex machine. After that, the sample was kept on a shaker for 30 min and the sample was centrifuged at 5000 rpm for 14 min to remove the unbound CA 242 antigen molecules and the buffer. Finally, 200 μL of 0.01× BSA buffer was added to the centrifuge tube and mixed uniformly.

A schematic representation of the three steps used in the sample preparation is shown in figure 4.14.

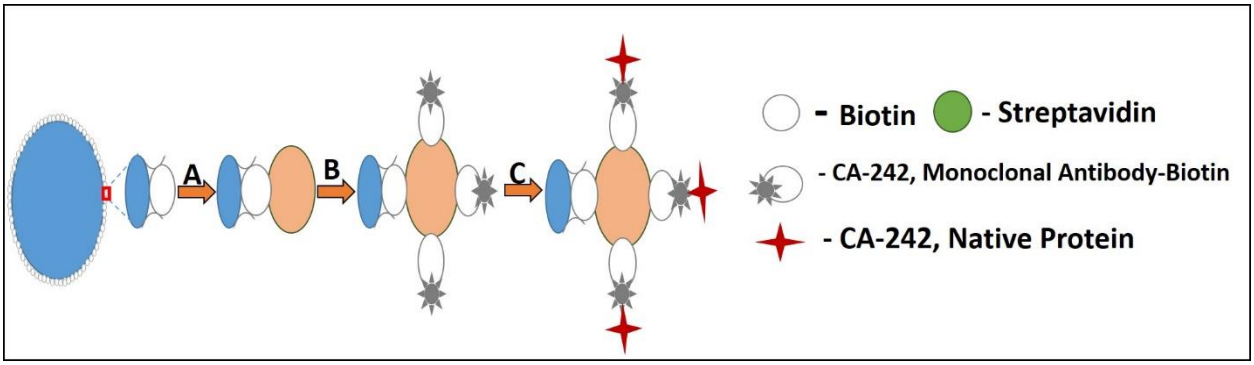

Figure 4.14: Schematic representation of the sample preparation (Biotinylated polystyrene microspheres (PM) + Streptavidin + Biotinylated CA 242 Monoclonal Antibody) with the antigen Native Protein CA 242, assuming binding in all the available sites of the antibody.

4.3.2.2. Interdigitated microelectrode

The direction of movement for the dielectric particle due to DEP depends upon the relative polarizability of the particle and the medium and on the presence of a large gradient of the electric field intensity produced by electrodes. In this experiment, we used the third generation electrode that was designed and fabricated at North Dakota State University.

The third-generation electrode was designed to accommodate one droplet of the sample on top of it. We measured the dimensions of the sample droplet at 6.44 mm x 4.65. The average dimension per side is 5.55 mm.

In the third-generation electrode, there are be an average of 25 hot spots per droplet, as opposed to 861, which is a 97% reduction in the number of hot spots, in addition to the reduction in the current in the remaining portion of the electrode due to the wider separation between adjacent electrodes. This new electrode array was designed to carry out experiments with a single droplet for several minutes before the droplet dries out.

The electrode was designed and drawn to scale in AutoCAD, validated in COMSOL Multiphysics, and fabricated on a commercially available glass wafer using photolithography,

metal sputtering, and lift-off procedures using 1000 Å thick gold film in the microfabrication facilities at North Dakota State University.

The electrode tip has a radius of curvature of 20 μm. The distance between the edges of the electrode to the tip of the concave surface is 50 μm. The base of the electrode tip curves at a radius of 658 μm. The base of the electrodes is separated by 1356 μm. The curvature of the concave surface is 80 μm. The concave surface is separated by each other by a curvature whose radius is 320 μm. Thirty electrodes were designed to fit within the wafer of diameter 100 mm which is as shown in figure 4.15.

The depiction of the electrode designed using AutoCAD is as shown in figure 4.15.

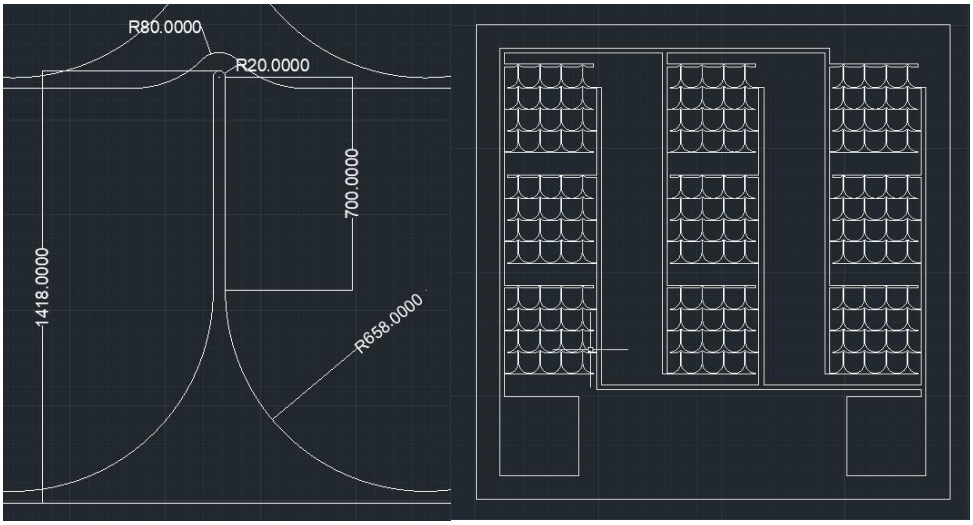

Figure 4.15: Dimensions of the electrode

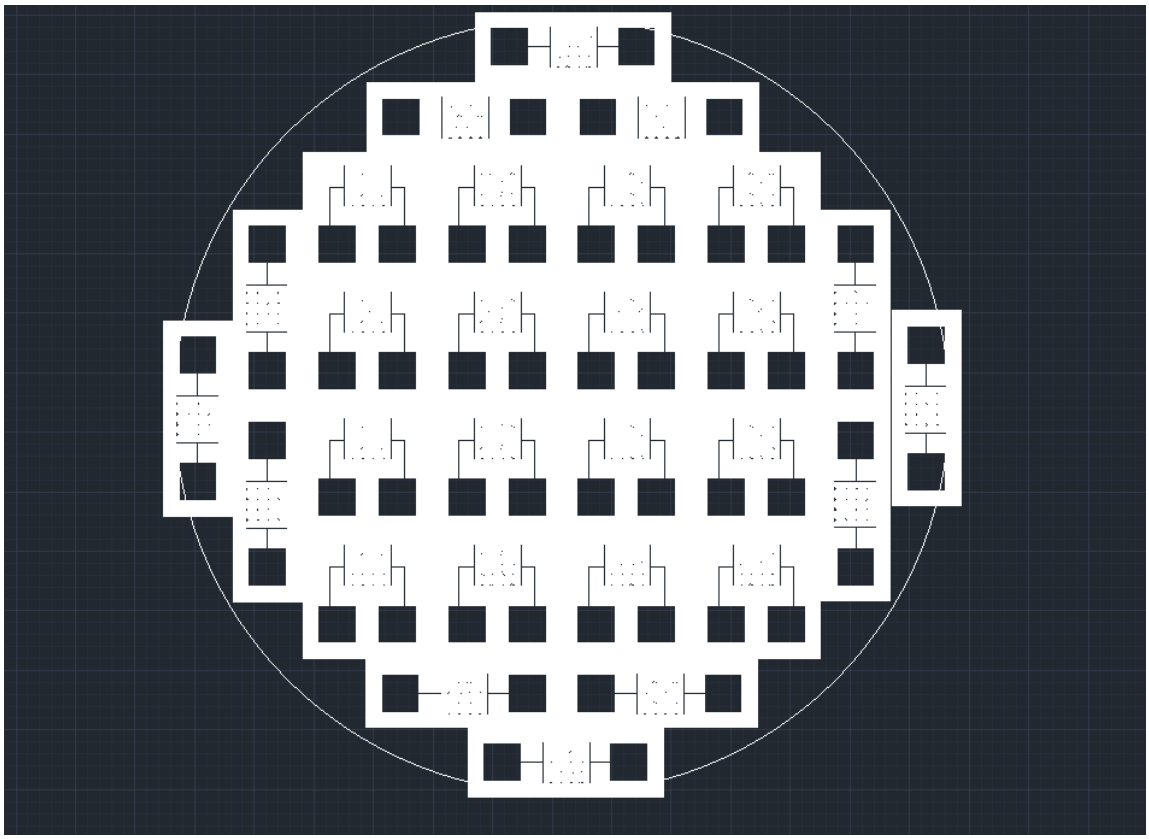

Figure 4.16: Thirty electrodes designed to fit within a 100 mm wafer.

Using COMSOL we verified that this electrode produces electric field intensities as high as 10^4 V/m and gradient of the electric field intensity as high 10^{16} V^2/m^3, which is enough to produce strong DEP forces to dielectric particles with a few hundred nanometers of diameter. This study was done with the collaboration of Sharmin Afrose. It was observed that the root mean square of the electric field and the electric field gradient produced by this electrode do not vary with the frequency from tens of kHz to several MHz. This ensures the sample is subjected to the same electric field gradient in all frequencies of interest, which makes DEP behavior depend only on the value of the real part of the Clausius–Mossotti factor [121].

The electric field gradient was measured using a 2D model of COMSOL. The initial design was drawn using AUTOCAD in .dfx file format as shown in figure 4.15 and then imported into COMSOL 2D simulation. The module used for the simulation was AC/DC with a submodule of

electric current (EC). The measurement was set to micrometers in the geometry tab. The boundary was set by drawing a rectangle around the electrode design. Using the materials section Gold and Glass were selected on the electrode. Water was used as the surrounding medium with conductivity set to 0.005 S/m and permeability set to 83. Respectively the conductivity of Gold was set to 4.10 $\times 10^7$ S/m and copper to 5.96 $\times 10^7$ S/m. The potential is set to be 10 V and is set to the inner array of the electrode, and the ground is set to the outer array of the electrode. We selected extremely fine in the mesh section to improve our modeling workflow. The study frequency was set to 120 kHz. The magnitude of the electric field gradient was calculated using the following formula using the variable *ec.normE* in COMSOL:

$$|\nabla \boldsymbol{E}| = \sqrt{\left(\frac{d(ec.normE^2)}{dx}\right)^2 + \left(\frac{d(ec.normE^2)}{dy}\right)^2}.$$

The electric field gradient was calculated at 1×10^{16} V/m^3 which is good enough to produce strong DEP forces to dielectric particles with a few hundred nanometers of diameter. The simulation results are as shown in figure 4.17.

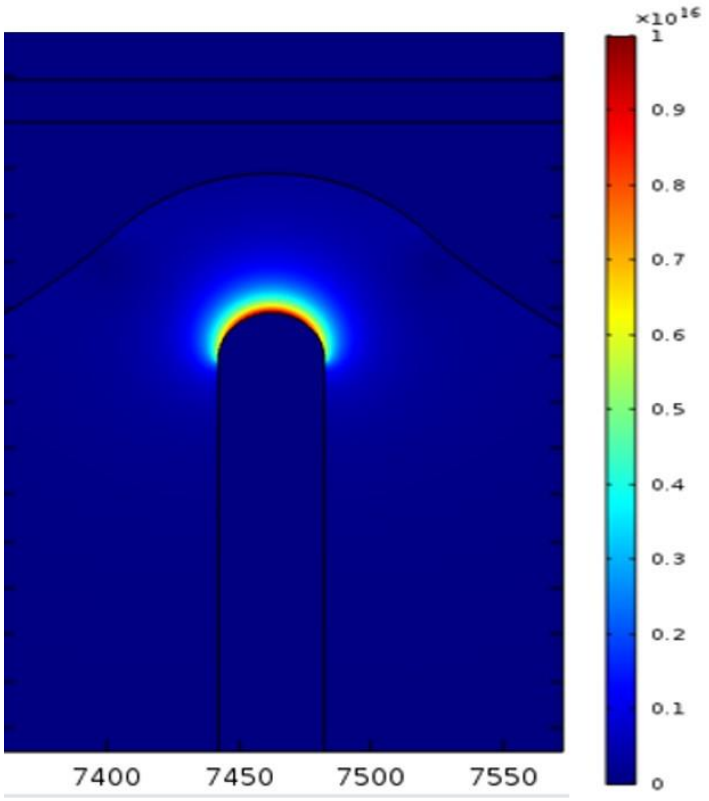

Figure 4.17: Electric field gradient on the single electrode.

One of the drawbacks of the third-generation electrodes is the high thermal conductivity acting upon the electrode due to DEP and hydrolysis. To address this issue, we deposited a thin SiO_2 layer on the electrodes. This process was done at the Minnesota Nano Center using the Savannah ALD system. The temperature was maintained at 150℃ to achieve a thickness of 200 Ang of ALD SiO_2 film. Later, the thickness was measured using Gaetner ellipsometer. Two of the wafers had SiO_2 thickness of 215 Ang deposited and the other two wafers had SiO_2 thickness of 230 Ang deposited on them.

4.3.2.3. Fabrication of interdigitated electrodes

The electrode was fabricated on a commercially available glass wafer with standard fabrication procedures involving photolithography, metal sputtering, and lift-off procedures using

1000 Å thick gold film in the microfabrication facilities at North Dakota State University. The details are explained below.

The following steps were used to fabricate the interdigitated electrodes.

- Wafers: Commercially available Borofloat 33 Glass Wafer with 100 mm diameter was purchased at UniversityWafer, Inc.
- Chrome Photomask: The chrome photomask was developed from FineLineImaging laser imaged phototooling. The CAD design was converted to checkplot and later developed into the photomask. The checkplot is as shown in figure 4.18.

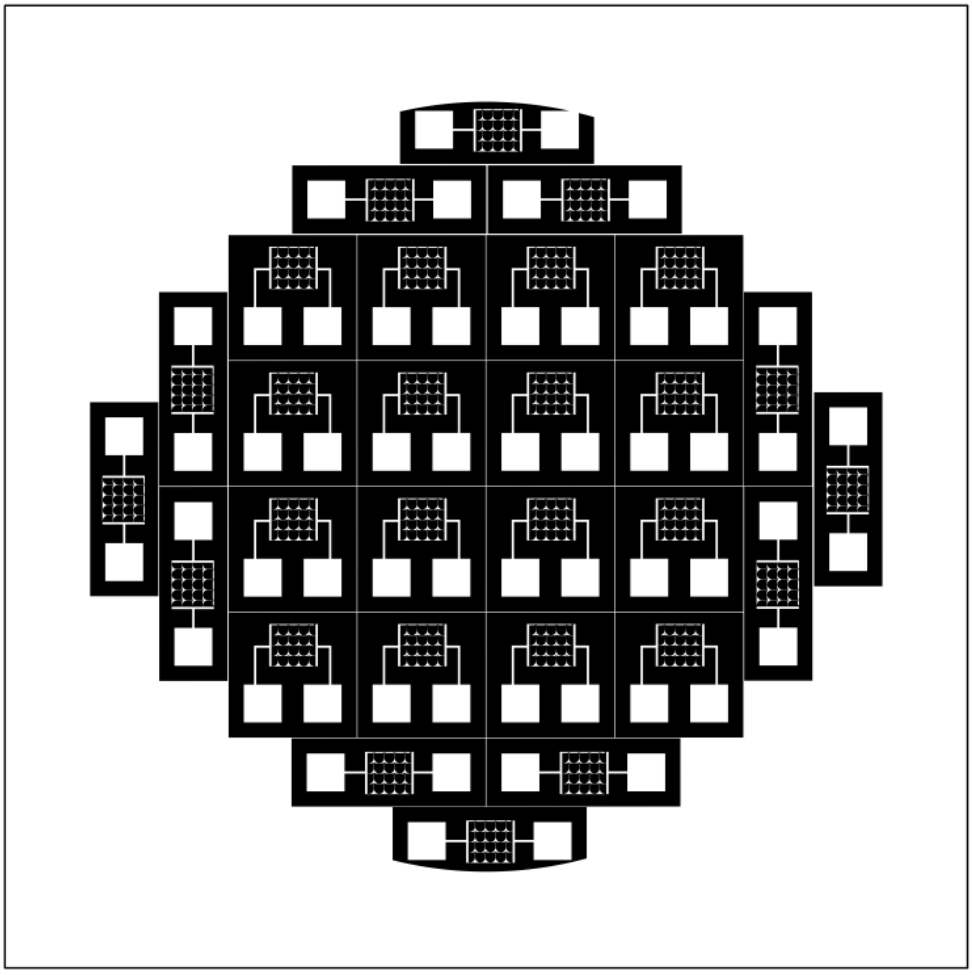

Figure 4.18: Checkplot obtained from the CAD design of the electrode.

- Piranha: The clean wafers were subjected to the Piranha cleaning solution for ten minutes at 50℃ using an acid sink to remove any organic materials.
- Rinse: The wafers are then rinsed twice using ultrapure deionized water for 30 seconds at the dump rinser to ensure complete contaminant removal from the wafer.
- Drying: The wafers are dried using a Semitool spin rinse dryer.
- Bake: The wafers are dried in Yamato-2 oven for 2 minutes at 120℃.
- HMDS: The wafers are kept in a YES oven to make the wafer hydrophobic.
- Coat: The mask is fixed o the wafer. The print face of the mask is kept on top, which is on the opposite side of the glass. The spin speed is set to 1000 rpm and spun using Suss Microtec rc8-ms3 spin coater.
- Soft bake: The wafers transferred for contact bake into the resist oven for 60 seconds at 90˚C.
- Expose: The wafers are put on the contact aligner MA8. This system utilizes 1X contact lithography to transfer photomask patterns onto substrates.
- Develop and rinse/dry: The wafers are rinsed and dried at the solvent sink for 60 seconds.
- Inspection: The wafers are checked using an Olympus Wafer Inspection & Imaging System (MX50) for cleared resist and checked for shorting bubbles.
- Metal deposition: Gold and chrome deposition on the wafers was done using a Lesker CMS 18 Deposition System. The deposition time for 100 nm of gold is set to 397 seconds and for 10 angstroms of chromium, the deposition time is set to 47 seconds.
- Liftoff: The wafers are submerged in acetone. The scribe metal is used to speed up the lift-off process. This is followed by an ultrasonic bath.

- Inspection: The wafers are inspected using an Olympus Wafer Inspection & Imaging System (MX50) to confirm that there are no short circuits in the electrode arrays.
- Dicing: The wafers are diced using ADT dicing saw.

4.3.2.4. DEP spectroscopy application

The DEP application, frequency sweep, and image processing are the same as that used in section 4.1.2.5.

For the experiments that we present here, the lowest frequency was set to 500 kHz, the frequency step was set to 300 kHz, and the highest frequency was 2 MHz for negative DEP. The peak-to-peak voltage value was set by to10 V. The time interval for positive DEP was set to 2000 ms and the time interval for negative DEP was set to 80 ms per frequency measurement.

4.3.2.5. Results

We validated our sensing method by carrying out DEP spectroscopy experiments with our image-processing software for observation and recording of the results during the experiments. The validation of the method is shown in figure 3. Initially, the software automatically sets the function generator to the frequency 10 kHz to establish positive DEP. Low-frequency electric fields (<50 kHz) produce positive DEP whereas high-frequency electric fields (>250 kHz) produce negative DEP force to the PM that we use in this study. The positive DEP force results in the attraction of the PM towards the edge of the electrode. A clear PM layer can be seen forming at the edge of the electrode in figure 4.19. Once the PM forms a layer at the edge of the electrode, our software automatically switches the frequency to a preset frequency that produces negative DEP. The negative DEP force pushes the PM from the edge of the electrode. The repulsion of the PM by the electrode is tracked and recorded using our custom-made software. Using this system,

we calculated the drift velocity of the PM layer repelled from the electrode, which is proportional to the DEP force, as they move away from the electrode edge using image processing.

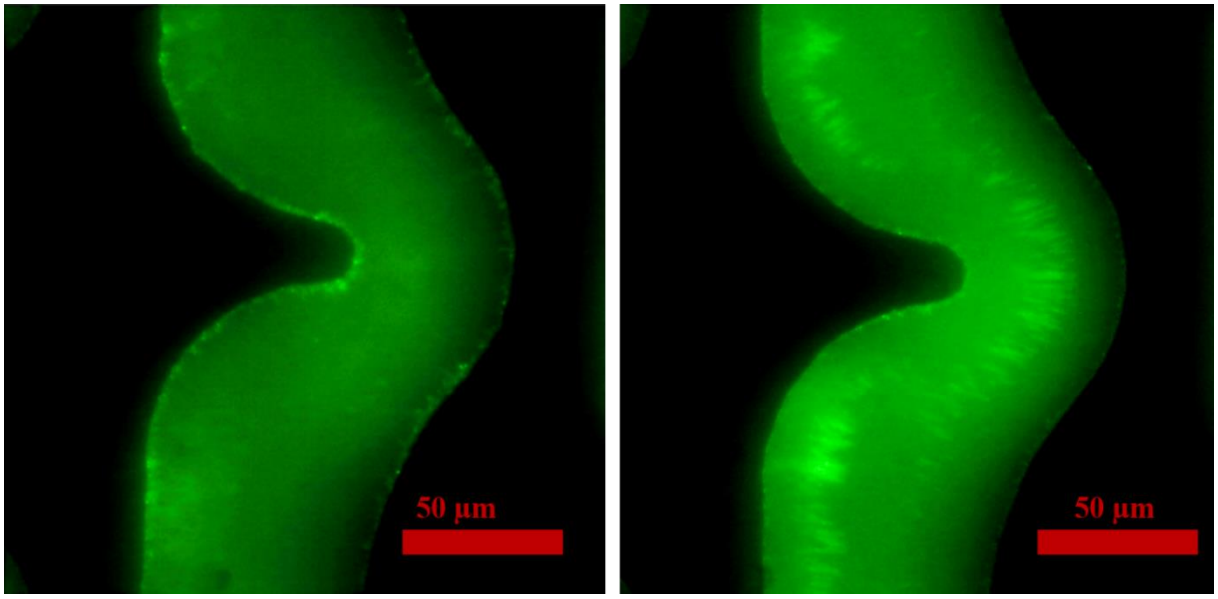

Figure 4.19: Demonstration of negative DEP effect through time-lapse images captured through the DEP spectroscopy application (Assuming t = 0 when electric field frequency is changed to induce negative DEP): (**a**) t = 0 ms and (**b**) t = 40 ms. The concentration of CA 242 in this solution is 37 U/mL. The interdigitated electrode is visible as a darker region in the picture. The bright layer visible on the edge of the electrode is formed by the accumulation of the sample. As the frequency is changed to induce negative DEP the antigen-bound PM is repelled from the electrode. For 60 s before the image (**a**), a 10 V peak-to-peak electric field at 10 kHz, which produces positive DEP, was applied to the electrodes. Then, the frequency of the electric field increased to 500 kHz, producing negative DEP. The scale bar on both figures indicates 50 µm.

We observed a relationship between the speed of repulsion of the PM functionalized with the CA 242 antibody as a function of both the frequency and the concentrations of the target CA 242 that we considered. As we switched to higher frequency electric fields with our software, we observed a clear dependence of the negative DEP spectrum on the concentration of the target CA 242 in the sample. While switching the frequency, we maintained all other experiment parameters and conditions constant. The obtained DEP spectroscopy results are shown in figure 4.20. In this figure, we show the drift velocity of the center of mass of the PM layer as a function of the frequency for a single measurement. We also show error bars with the standard deviation obtained

in six measurements, which is an indication of the confidence interval in each measurement. Since there is very little overlap between the confidence intervals of these curves, only one measurement of the DEP spectrum is needed in each experiment to accurately determine the cutoff level of CA 242. These results indicate that this label-free method has the potential to be used as the transduction mechanism to measure the cutoff levels of CA 242 that can be used for the diagnosis and monitoring of pancreatic cancer. Therefore, figure 4.20 can be used as the calibration curve for the diagnosis of pancreatic cancer in the early stage and for disease monitoring during treatment.

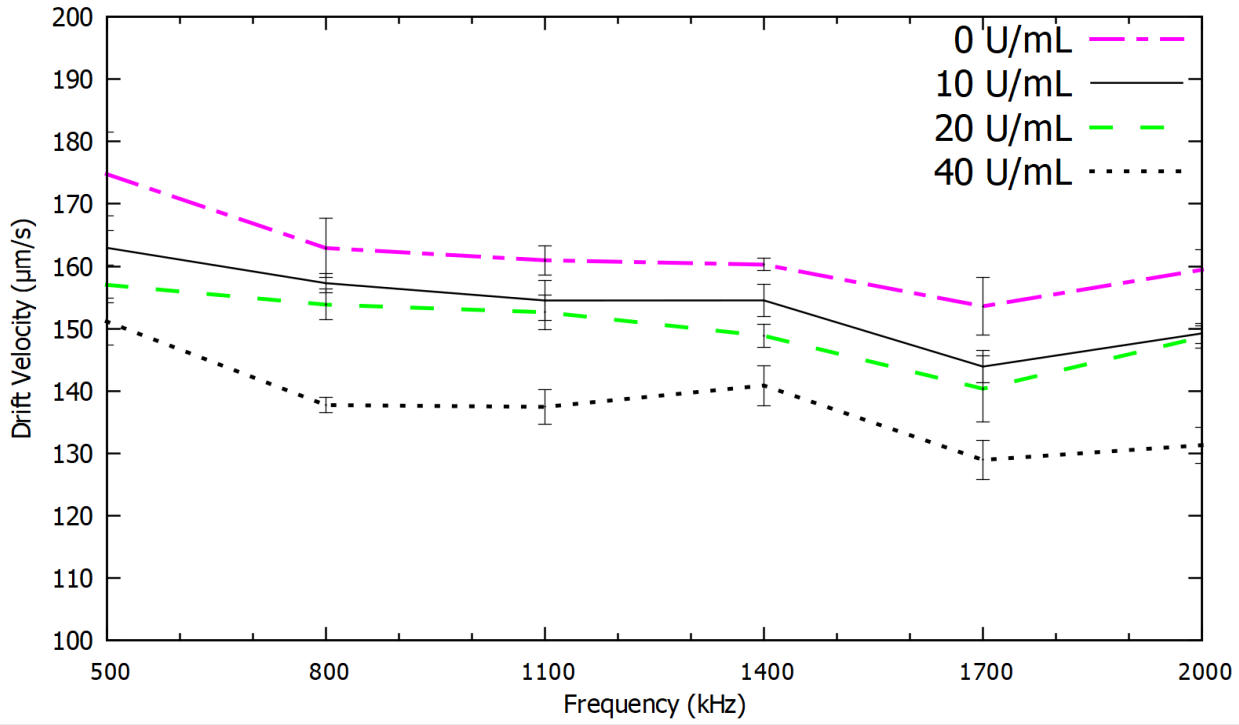

Figure 4.20: Negative DEP spectrum curves for cutoff levels of CA 242 for the detection of pancreatic cancer at 10 U/ml, 20 U/mL, 40 U/mL, and 0 U/mL. The 0 U/mL is a control group sample without the native antigen of CA 242 attached. The error bars show the confidence interval in each measurement that was calculated using six measurements per frequency.

4.4. Conclusion

In this chapter, we demonstrated that DEP spectroscopy is an effective label-free transduction mechanism for the detection of the cutoff levels of pancreatic cancer biomarkers such

as CA 19-9, CA 242, and CEA in serum. The velocity of repulsion due to DEP on a set of PM functionalized to a monoclonal antibody to CA 19-9 was measured at 0 U/mL, 37 U/mL,100 U/mL, 300 U/mL, and 1000 U/mL, CA 242 at 0 U/mL, 10 U/mL, 20 U/mL, 40 U/mL and CEA at 0 ng/mL, 5 ng/mL, 10 ng/mL and 20 ng/mL concentration cutoff levels at the frequency range from 0.5 to 2 MHz. The 0 U/mL is a control group sample without the native antigen attached. The proposed method is an effective transduction mechanism for the detection of the cutoff levels of pancreatic cancer protein biomarkers, which can be used in the early-stage diagnosis and the prognosis of pancreatic cancer.

5. BIOSENSING FOR THE CHARACTERIZATION OF GENE EXPRESSION IN CELLS[3]

5.1. Introduction

In any living organism, messenger ribonucleic acid is a vital and functional constituent in the DNA present in cells. Messenger RNA (mRNA) serves as a sensitive biomarker in the prognosis and diagnosis of diseases as it holds a key connection between genome and proteome as it carries the information from the DNA to initiate the protein synthesis [41]. Some of the cell regulatory pathways are controlled by mRNAs such as cell cycles, chromatin modifications, and cell adhesions, [124], and these regulatory pathways can be affected by different mRNA expression caused by activation mRNA degradation, point mutation, among others, leading to cause several diseases including cancer [41], [43], [125].

Some of the examples of mRNA correlated with diseases are Cyclin D1 and TS mRNA's correlated with breast cancer, altered levels of TERT, and EGFR mRNA [126], [127], correlated with lung cancer, and FAM134B mRNA expression correlated with colon adenocarcinoma and esophageal squamous cell carcinoma [128]. mRNA expression profiling can be used as a potential disease biomarker [129]. Previous studies have shown that the prognosis and drug response to cancer can be achieved by screening and quantifying the mRNA levels [129], [130].

Gene expression profiling determines what genes are expressed in a cell at any given time and it's level of expression (number of corresponding mRNA copies) [131]–[133]. Transcription

[3] This chapter was extracted from a published article in Chemosensors (F. D. Gudagunti, V. Jayasooriya, S. Afrose, D. Nawarathna, and I. T. Lima, "Biosensor for the characterization of gene expression in cells," Chemosensors, vol. 7, no. 4, 2019, doi: 10.3390/chemosensors7040060). Conceptualization, I. T. Lima and F. D. Gudagunti; Formal analysis, F. D. Gudagunti and V. Jayasooriya; Investigation, F. D. Gudagunti and V. Jayasooriya; Methodology, F. D. Gudagunti, V. Jayasooriya, D. Nawarathna and I. T. Lima; Project administration, I. T. Lima; Writing—original draft, F. D. Gudagunti; Writing—review & editing, V. Jayasooriya, S. Afrose, D. Nawarathna and I. T. Lima.

is the first step of gene expression, in which a segment of DNA is copied into RNA by the enzyme RNA polymerase [134].

Gene expression, up-regulation of genes, or downregulation of genes is used to diagnose cancer and other diseases [135]. There are several methods such as polymerase chain reaction (PCR), sequencing, and microarrays available for gene expression profiling. These methods typically transcribe the RNA into complementary DNA by reverse transcriptase reaction. Since in these methods each mRNA molecule produces one DNA molecule to initiate the PCR process, any degradation of mRNA before the PCR process causes large errors in the calculation of the gene expression levels using these methods. To produce higher complementary DNA yields pure RNA extraction is important. Thus, there is a need for a technique that can detect mRNA without any RNase activity that degrades the mRNA strands.

The commonly used methods to detect mRNA are the same as the nucleic acid detection techniques such as quantitative reverse transcription PCR (qRT-PCR), RNA sequencing method, and microarrays [136], [137]. Although these methods are reliable it comes with a drawback of enzymatic amplification and high-cost equipment. These methods demand the reverse transcription of the mRNA into complementary DNA (cDNA), leading to a decrease in the accuracy due to partial amplification and template switching of the sample sequence. Gel electrophoresis and fluorescence intensity are used as external readouts, which contribute to the high cost and complexity of this method. Due to these limitations, the nucleic acid detection methods are non-suitable for point of care applications [138].

Other popular methods to detect mRNA are electrochemical and optical readouts [139], [140]. These methods had shown potential due to their high sensitivity and cost-effectiveness [141]–[144]. These sensors require complex fabrication techniques and they also use electroactive

ligands that require modifications with the target sample that can interfere with the sensor effectiveness. Therefore, there is a need for amplification-free, label-free, high-sensitive, high throughput, and cost-effective methods to detect mRNA from cells.

We recently demonstrated a label-free biosensing method for the detection of the pancreatic cancer biomarker CA 19-9 based on dielectrophoresis spectroscopy [145]. We demonstrated earlier that this method can detect a concentration of as little as 13 aM per polystyrene microsphere [146]. In this study, we show that DEP spectroscopy is a rapid, low-cost, and label-free-transduction mechanism for biosensors to measure mRNA expression levels in living cells.

5.2. Materials and Methods

5.2.1. Sample preparation

- Cell culturing: CRL 1764 (rat fetus fibroblast) adherent cells were purchased from ATCC and cultured at 37°C in a 5% CO_2 incubator. This cell line was selected as a model to verify the effectiveness of the gene expression biosensor that we developed. The cells were subcultured on time so that the cells are in log phase by the time they were being taken to experiments. Cells were taken into the experiment when they are 75% confluent (approximately 1×10^6 cells). First, the cell culture media was removed and the cells were washed thrice with ice-cold RNAse free Phosphate-buffered saline (PBS). Then, PBS was removed from the culture flask and 1 mL of RNAse free ice-cold lysis buffer was added. Then the lysate was carefully removed from the flask and centrifuged at 14000 rpm at 4°C for 10 minutes. After carefully removing the supernatant from the pellet, the supernatant was kept in ice before the hybridization procedure. Based on data available in the Human Protein Atlas database

(https://www.proteinatlas.org/), each CRL 1764 cell contains an average of 105 to 228 β-actin mRNAs, 149 to 265 GAPDH mRNAs, and 17 to 37 HPRT mRNAs.

- Hybridization: For detecting β-Actin, GAPDH, and HPRT, mRNA Biotinylated 5′-/5Biosg/ACC GCT CAT TGC CGA TAG TGA TGA-3′, Biotinylated 5′-/5 Biosg/TGA CTC TAC CCA CGG CAA GTT CAA-3′ and Biotinylated 5′-/5Biosg/CTG CCT ACA GGC TCA TAG TGC AAA-3′ were used, respectively, as the complementary DNA primers. In the experiment, 25 µL of 100 µM mRNA binding primer was added to a 25 µL of the cell lysate and hybridized using PCR with the following cycle protocol: 5 min at 95°C, 2 mins at 68°C, and cooled down at room temperature for 1 hour. This protocol was obtained with series of control experiments regarding the standard procedure [147]. For detecting the mRNA levels in varying cell concentrations, the cell lysate was diluted before the hybridization, as shown in figure 5.1.

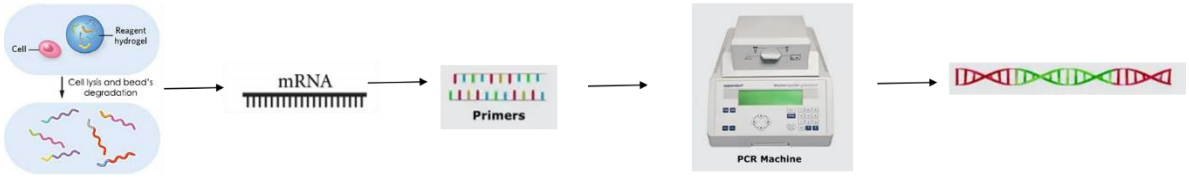

Figure 5.1: Procedure used to hybridize the primers with the mRNA molecules.

Before the experiments, SYBR green was used to verify the hybridization. The presence of hybridized mRNA was confirmed by bright green fluorescence compared to its prior dark background. After completing the mRNA hybridization with the biotinylated mRNA binding primers, the sample was mixed with avidin functionalized polystyrene microspheres (APM) to the ratio of 1:25 (Biotin: APM) by volume, according to the specifications by the supplier. Then the sample was washed three times to remove the unhybridized biotinylated mRNA primers, the lysis buffer, and other unwanted molecules.

5.2.2. DEP spectroscopy application

To carry out the DEP measurement, use used an image processing software that we developed. The software is integrated with a Tektronix AFG series function generator and a USB video class (UVC) standard compliant microscope camera mounted on an OMFL600 low-power microscope. The application controls the function generator to produce DEP force and the software tracks the center of mass of the PM band whose position varies with the strength and type of DEP force. The field of view processed by the software is as shown in figure 5.2. The software calculates the DEP spectrum by tracking the drift velocity of the center of mass of the PM as a function of the applied frequency.

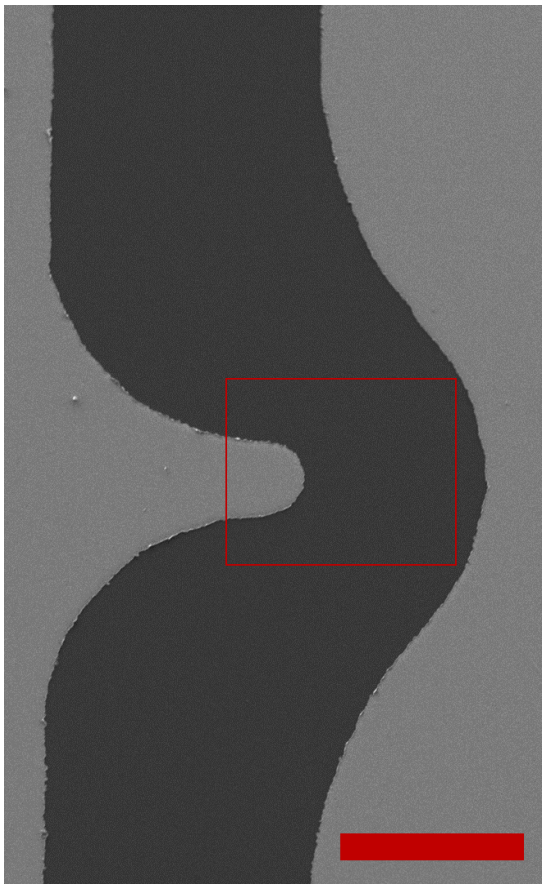

Figure 5.2: The dialog window of the software interface that shows the field of view being processed in the red box. The clear regions correspond to the electrode. The red scale bar indicates 50 µm.

The software application was designed to extract the pixel and color information from the live images captured. Since the goal is to determine the effect of DEP force on the PM in the solution, the system monitors the region of interest in the video where a strong DEP effect is observed. The region of interest is the area in which the electric field gradient and, consequently, the DEP force is the strongest, which consists of the region included in the red rectangle shown in figure 5.2, which form the areas in the field of view of the camera that is processed to calculate the drift velocity due to the DEP force as a function of the frequency of the electric field. The drift velocity is proportional to the friction force and, consequently, is proportional to the DEP force. The desired time interval is set to capture time-lapse images for the drift velocity calculation. The minimum time interval to capture an image or to record a new data value is in the order of 80 ms, which is determined by the frame rate of the video stream and the processing speed of the hardware.

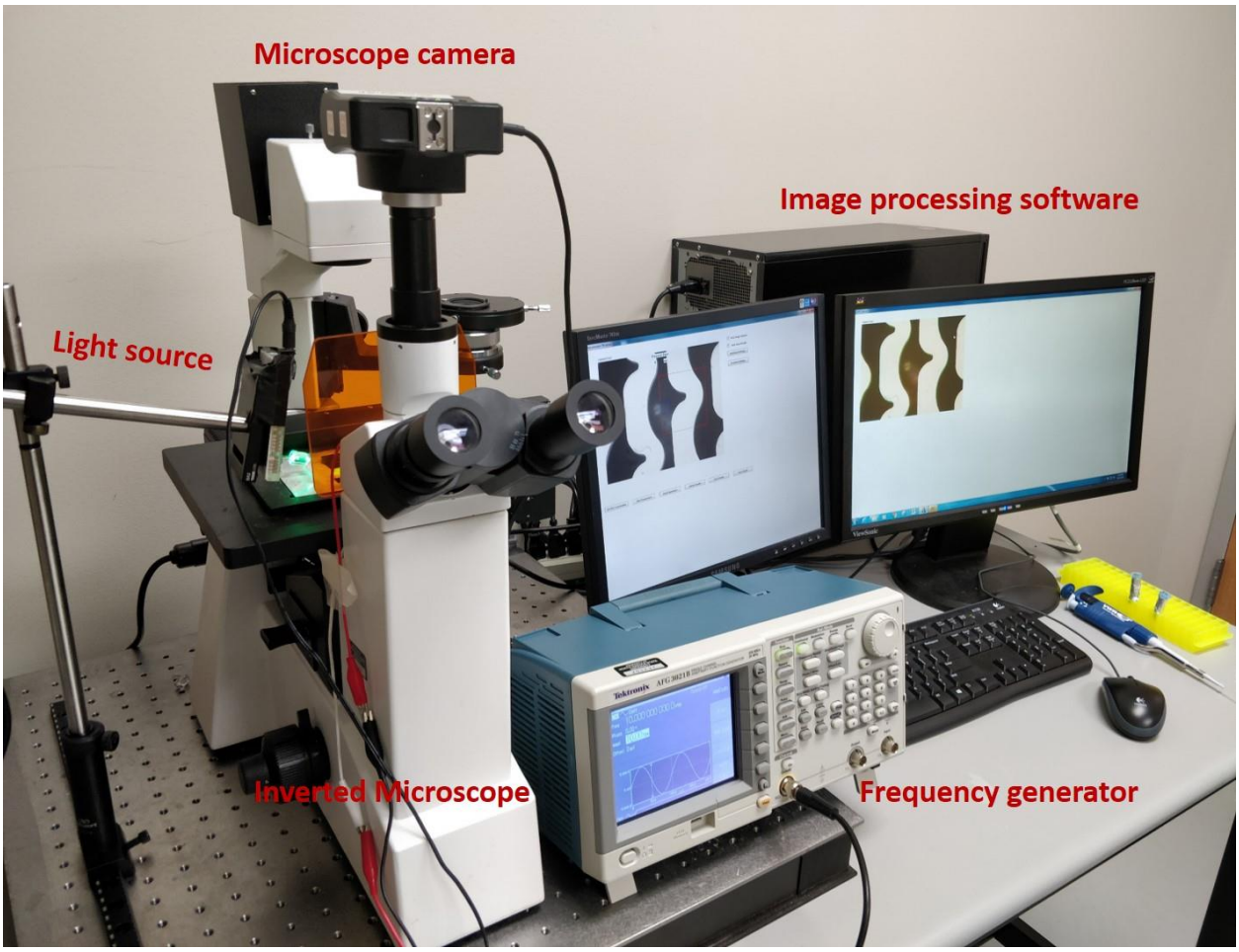

Figure 5.3: Experimental setup

The DEP application, frequency sweep, and image processing are as same as used in section 4.1.2.5. The experimental setup used is shown in figure 5.3.

For the experiments that we present here, the lowest frequency was set to 500 kHz, the frequency step was set to 300 kHz, and the highest frequency was 2 MHz for negative DEP. The peak-to-peak voltage value was set by to10 V. The time interval for positive DEP was set to 2000 ms and the time interval for negative DEP was set to 80 ms per frequency measurement.

5.3. Results and Discussion

We validated our method by carrying out experiments using mRNA-bound PMs with our custom-made real-time image processing software for recording and analyzing the results. Once

the electrode is imaged by the low power microscope and placed in the region in the field of view monitored by the image-processing software, the frequency-sweep process for the DEP spectrum measurement is initiated. Once the application applies 10 kHz at 10 V peak-to-peak using the function generator to establish the positive DEP force, an mRNA-bound PM band is formed near the edge of the electrode as shown in figure 5.4. The software applies this frequency for 400 ms after witching to 0.5 MHz, which produces negative DEP while maintaining the same peak-to-peak voltage. This leads to the repulsion of the mRNA-bound PM from the edge of the electrode. The software captures the images at 25 frames per second from the live capturing of the video. The repulsion of the mRNA-bound PM is tracked along the axis of the electrode within the region of interest. With known positions of the PM at two different times in which negative DEP is applied, we calculate the drift velocity of the mRNA-bound PM layer, which is proportional to the DEP force. This is repeated for five additional electrical frequencies ranging from 0.8 MHz to 2 MHz, which also produce negative DEP. Low-frequency electric fields (<50 kHz) produce positive DEP whereas high-frequency electric fields (> 250 kHz) produce negative DEP force to the mRNA-bound PM that we use in this study.

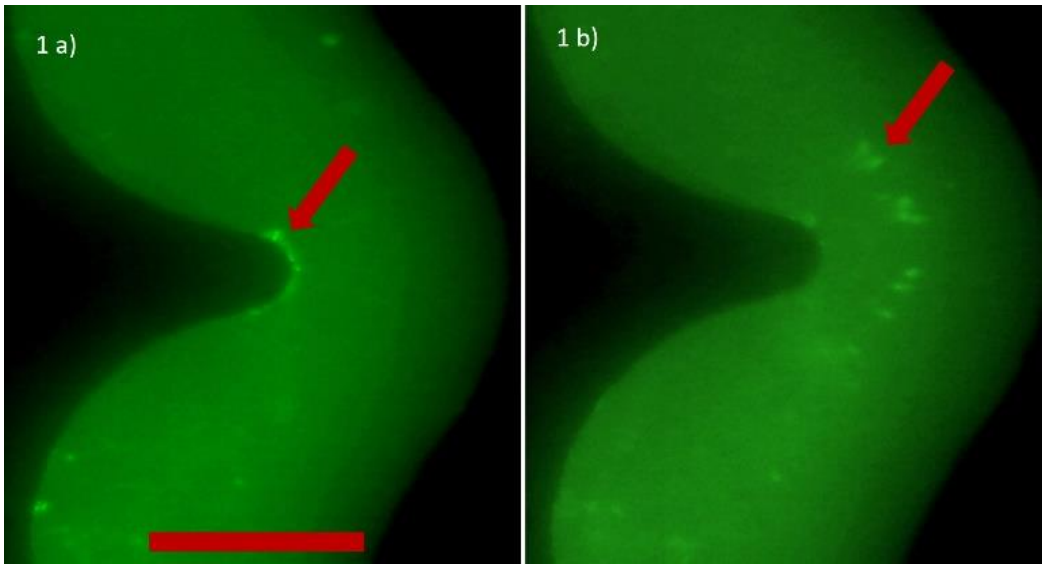

Figure 5.4: Experimental Demonstration of negative DEP force for mRNA bound to the PM at (a) t = 0 ms and (b) t = 40 ms after the frequency 0.5 MHz is applied at 10 Vp-p. The scale bar indicates 50 μm.

Once the images are extracted at the beginning and 40 ms after a frequency that produces negative DEP is applied, we analyzed the light intensity along the axis from the edge of the convex electrode. Both the images are processed to determine the difference between the center of mass of the PM bands so that the drift velocity of the PM band due to negative DEP can be calculated for the applied frequency.

We validated this study to determine the mRNA levels of β-actin, GAPDH, and HPRT from 1,000,000 cells, 100,000 cells, and 10,000 cells. We observed a relationship between the speed of repulsion of the PM functionalized with different mRNA as a function of both the frequency and the number of cells, which is proportional to the number of mRNA molecules. All the parameters for the experiment were maintained constant to optimize the accuracy. The obtained DEP spectroscopy results are shown in figures 5.5, 5.6, and 5.7, each experiment was repeated 6 times to check the precision of the measurements. Figures 5.5, 5.6, and 5.7 show the average of 6 measurements for each frequency. We plotted the standard deviation of the average measurement

calculated with these results using error bars in figures 5.5, 5.6, and 5.7 as the indicator of the confidence levels in each measurement.

There is no overlap between the confidence intervals in several of the frequencies used to describe the spectrum especially for the mRNA levels of β-actin and GAPDH. However, in the quantification of HPRT, which is rare, an increase in the number of spectral measurements is required to achieve the same accuracy level. Even though there is a significant overlap in the DEP spectrum for HPRT mRNA, the results with 10,000 and 100,000 cells are different by more than one standard deviation with applied frequency at 800 kHz. Therefore, the use of this method with six measurements is sufficient to resolve the number of HPRT mRNA in these two cases.

Since the DEP spectrum can accurately determine each of the mRNA concentration levels of β-actin, GAPDH, and HPRT showed in figures 5.5, 5.6, and 5.7. This label-free method has the potential to be used as the transduction mechanism for the measurement of different varieties of mRNA at different expression levels. This method, which does not require the use of mRNA amplification of fluorescence markers, has the potential to be used in the sensing of protein mRNA biomarkers of diseases.

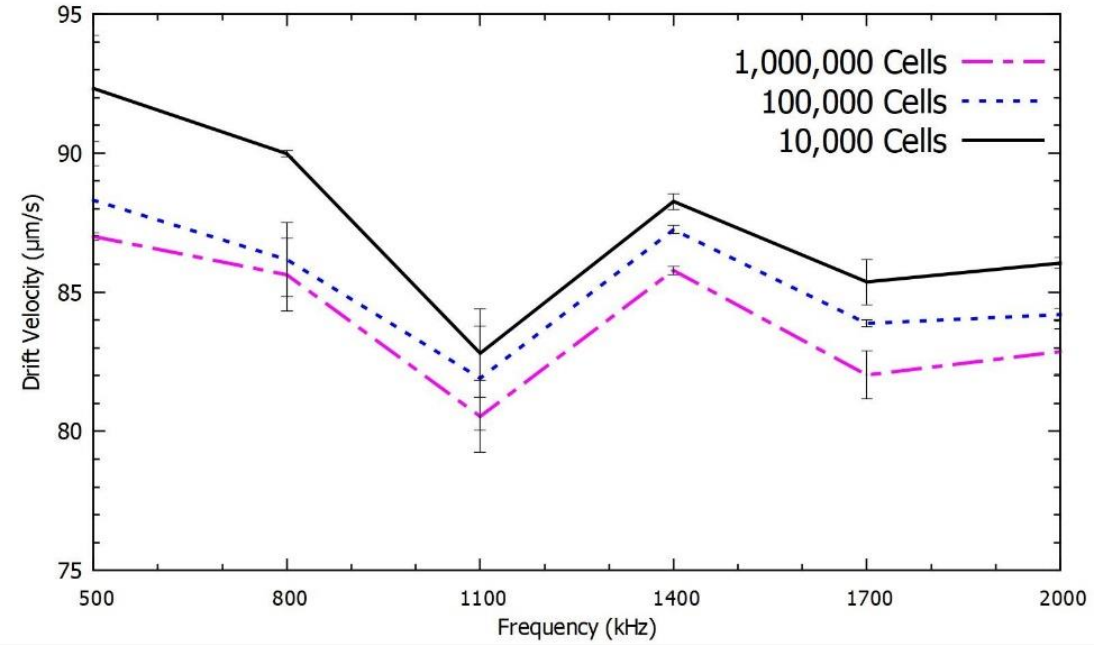

Figure 5.5: Negative DEP spectra of β-actin mRNA species from a range of living cells

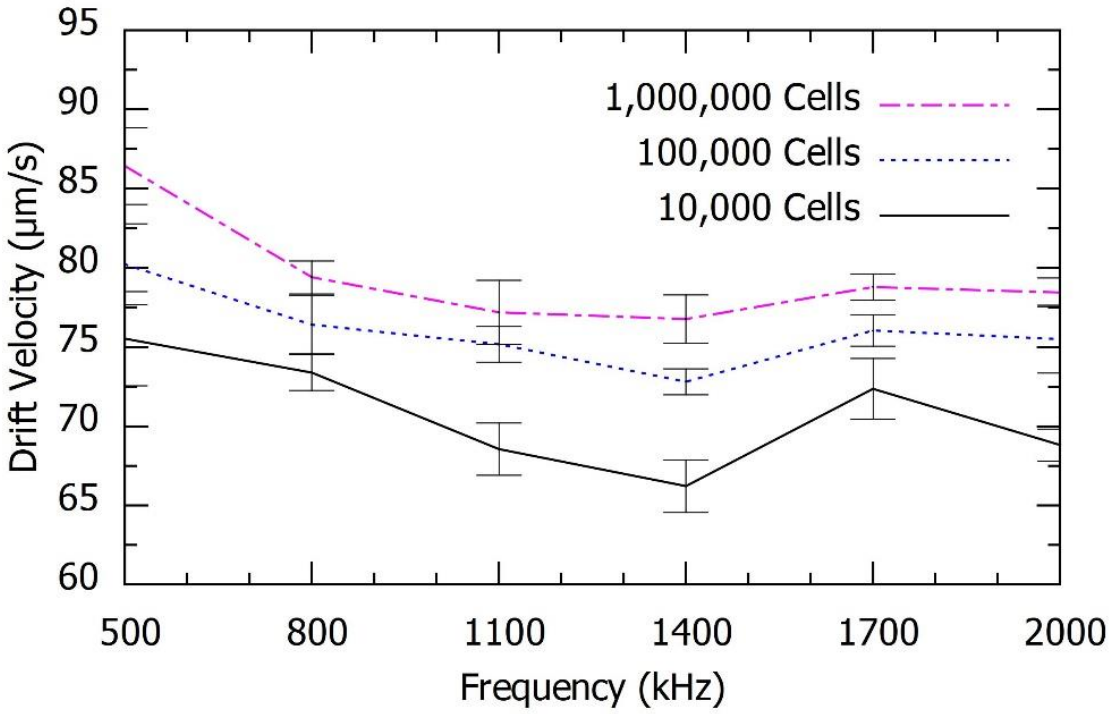

Figure 5.6: Negative DEP spectra of GAPDH mRNA species from a range of living cells

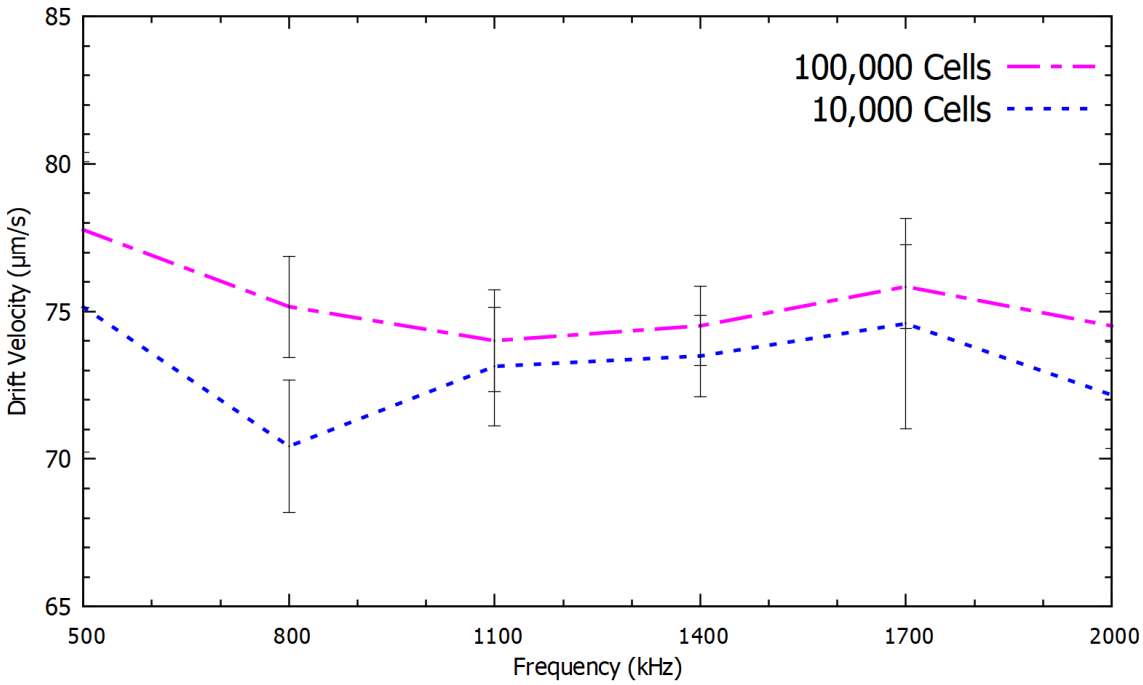

Figure 5.7: Negative DEP spectra of HPRT mRNA species from a range of living cells

5.4. Conclusion

In this chapter, we demonstrated that DEP spectroscopy is an effective transduction mechanism for the extraction and analysis of the genetic expression of β-actin, GAPDH, and HPRT from cells that has the potential to be applied in the genetic expression of proteins that could be used as indicators of cancer or the patient response to drugs during treatment. However, the effectiveness of this method to sense the concentration levels of the protein mRNA biomarkers of those diseases has to be investigated for each case. We carried out a demonstration of this biosensor using three different types of mRNA from as little as 10,000 living cells. This technique is rapid and has high specificity when targeting a given mRNA with the use of proper RNA primers. This technique does not require the use of fluorescent labels, which eliminates the washing step of unbound fluorescent molecules in the preparation process and it does not require careful calibration of the light source and the photodetector sensitivity. The measurement of the negative DEP spectrum does not depend on the light intensity, the number of PM, or the sensitivity of the

microscope camera. This technique is fast, simple, repeatable, and reliable when compared with existing methods for mRNA profiling.

6. CONCLUSION

We demonstrated that negative DEP spectroscopy can be used as the transduction mechanism to accurately detect the concentration of protein and genetic biomarkers in serum. In chapter 1 we explained disease biomarkers, types, and their potential use. We discussed the challenges in detecting those biomarkers in body fluids. In chapter 2, we explained the development of the software application using Microsoft foundation classes in visual C++ for Windows that measures the drift velocity of dielectric particles due to DEP as a function of the frequency of the electric field applied to the interdigitated electrode. The application is integrated with a USB video class (UVC) standard compliant microscope camera, Tektronix AFG series function generators, pearl-shaped interdigitated electrode, OMFL600 low power microscope, and a custom-based optical side illumination technique. The developed application can capture a sequence of video frames from any USB video class standard-compliant microscope camera. Using the acquired images, our system performs real-time image processing to extract the effect of DEP force on the dielectric particles, and, thus, the DEP spectrum can be obtained. A frame rate of 25 frames per second is used in the application for capturing and displaying the live video from the microscope camera.

During the third study discussed in chapter 3, we demonstrated that the negative DEP spectroscopy method is an effective transduction method to accurately detect SNPs with which genetic variants causing human diseases can be found [148]–[150]. The negative DEP spectrum was measured using a custom-made real-time image processing technique to detect the drift velocity of PM bound to ssDNA in microstructured electrodes since the drift velocity is proportional to the DEP force due to the viscosity of the solution. The frequency-dependent velocity of repulsion due to negative DEP on a set of PM bound to ssDNA, which is a label-free

quantity that we measure using image processing, has a strong dependence on the last and in the second-to-last nucleotides in ssDNA sequences.

In the fourth study discussed in chapter 4, we demonstrated that negative DEP spectroscopy can be used as the transduction mechanism to accurately detect the concentration of CA 19-9, CA 242, and CEA which is a pancreatic cancer biomarker [145]. We measured the negative DEP spectrum using real-time image processing to detect the drift velocity in which dielectric microspheres functionalized with monoclonal antibody to CA 19-9, CA 242, and CEA is repelled by an interdigitated electrode array due to DEP as a function of the frequency. We showed that DEP spectroscopy has sufficient sensitivity to detect the various cutoff levels of the pancreatic cancer biomarkers that can enable this method to be used in the diagnosis and the monitoring of pancreatic cancer. The drift velocity due to negative DEP was calculated for the frequency range from 500 kHz to 2000 kHz. PM with 750 nm diameter was imaged using a side illumination technique to detect the Mie scattering produced by the PM. The change in the DEP spectrum with the binding of even a small concentration of these pancreatic cancer biomarkers to the conjugated antibody binding sites on the PM arose from the changes in the distribution of the ions from the solution close to the PM surfaces in the presence of the target molecules. We designed a new set of electrodes (second generation) in such a way that on one side of the array there is the electrode edge and on the opposite side, there is a concave structure with no sharp edges. With no sharp edges, the concave structure would have very minimal or no DEP acting on it. With the new electrode, the PM that experiences the positive DEP would attract on the edge of the electrode, and during the negative DEP, it will be repelled away from the edge of the electrode. In the next cycle of frequency, the same set of PMs will be attracted back to the edge of the electrode as there is no or very minimal gradient on the concave structure. This made the lab experiments more

robust, helped maintain uniformity, and also optimized the experiment time. We later improved the second-generation electrode by designing and fabricating this third-generation electrode. The third-generation electrode has an average of 25 hot spots per droplet, as opposed to 625 as is the case of the second-generation electrode. That represented a 96% reduction in the number of hot spots when compared with the second-generation electrode, in addition to the reduction in the current in the remaining portion of the electrodes of the array due to the wider separation between the adjacent electrodes. This new electrode array was designed to carry out experiments with a single droplet for several minutes before the droplet dries out.

In our fifth study discussed in chapter 5, we demonstrated that DEP spectroscopy is an effective transduction mechanism for the extraction and analysis of the genetic expression of β-actin, GAPDH, and HPRT from cells that has the potential to be applied in the genetic expression of proteins that could be used as indicators of cancer or the patient response to drugs during treatment [151], [152].

We conclude that we have developed a low-cost, automated, high throughput, highly sensitive, label-free, user-friendly technique to detect the disease biomarkers from serum in point-of-care settings.

REFERENCES

[1] R. L. Siegel, K. D. Miller, and A. Jemal, "Cancer statistics, 2020," *CA. Cancer J. Clin.*, vol. 70, no. 1, pp. 7–30, 2020, doi: 10.3322/caac.21590.

[2] J. D. Schiffman, P. G. Fisher, and P. Gibbs, "Early Detection of Cancer : Past , Present , and Future INTRODUCTION TO CANCER SCREENING AND," *ASCO Educ. B.*, 2015.

[3] R. Etzioni *et al.*, "The case for early detection," *Nat. Rev. Cancer*, vol. 3, no. 4, pp. 243–252, 2003, doi: 10.1038/nrc1041.

[4] A. Chan *et al.*, "Validation of biomarkers that complement CA19.9 in detecting early pancreatic cancer," *Clin. Cancer Res.*, vol. 20, no. 22, pp. 5787–5795, 2014, doi: 10.1158/1078-0432.CCR-14-0289.

[5] M. N. Lassere, "The biomarker-surrogacy evaluation schema: A review of the biomarker-surrogate literature and a proposal for a criterion-based, quantitative, multidimensional hierarchical levels of evidence schema for evaluating the status of biomarkers as surrogate endp," *Stat. Methods Med. Res.*, vol. 17, no. 3, pp. 303–340, 2008, doi: 10.1177/0962280207082719.

[6] S. H. Loosen, U. P. Neumann, C. Trautwein, C. Roderburg, and T. Luedde, "Current and future biomarkers for pancreatic adenocarcinoma," *Tumor Biol.*, vol. 39, no. 6, 2017, doi: 10.1177/1010428317692231.

[7] N. L. Henry and D. F. Hayes, "Cancer biomarkers," *Mol. Oncol.*, vol. 6, no. 2, pp. 140–146, 2012, doi: 10.1016/j.molonc.2012.01.010.

[8] F. S. Collins and H. Varmus, "A new initiative on precision medicine," *N. Engl. J. Med.*, vol. 372, no. 9, pp. 793–795, Feb. 2015, doi: 10.1056/NEJMp1500523.

[9] T. Kamisawa, L. D. Wood, T. Itoi, and K. Takaori, “Pancreatic cancer,” *Lancet*, vol. 388, no. 10039, pp. 73–85, 2016, doi: 10.1016/S0140-6736(16)00141-0.

[10] I. Tzoulaki, K. C. M. Siontis, and J. P. A. Ioannidis, “Prognostic effect size of cardiovascular biomarkers in datasets from observational studies versus randomised trials: meta-epidemiology study,” *BMJ*, vol. 343, pp. d6829–d6829, Nov. 2011, doi: 10.1136/bmj.d6829.

[11] S. M. Paul *et al.*, “How to improve R&D productivity: the pharmaceutical industry's grand challenge,” *Nat. Rev. Drug Discov.*, vol. 9, p. 203, Feb. 2010, [Online]. Available: https://doi.org/10.1038/nrd3078.

[12] D. J. Slamon *et al.*, “Numb Er 11 Use of Chemotherapy Plus a Monoclonal Antibody Against Her2,” *English J.*, vol. 344, no. 11, pp. 783–792, 2001, doi: 10.1056/NEJM200103153441101.

[13] E. H. Romond *et al.*, “Trastuzumab plus Adjuvant Chemotherapy for Operable HER2-Positive Breast Cancer,” *N. Engl. J. Med.*, vol. 353, no. 16, pp. 1673–1684, 2005, doi: 10.1056/NEJMoa052122.

[14] E. Van Cutsem *et al.*, “Cetuximab and Chemotherapy as Initial Treatment for Metastatic Colorectal Cancer,” *N. Engl. J. Med.*, vol. 360, no. 14, pp. 1408–1417, 2009, doi: 10.1056/NEJMoa0805019.

[15] V. Degos *et al.*, “An admission bioclinical score to predict 1-year outcomes in patients undergoing aneurysm coiling,” *Stroke*, vol. 43, no. 5, pp. 1253–1259, 2012, doi: 10.1161/STROKEAHA.111.638197.

[16] Y. K. Zheng *et al.*, “Comparison of plasma copeptin and multiple biomarkers for assessing prognosis of patients with aneurysmal subarachnoid hemorrhage,” *Clin. Chim. Acta*, vol. 475, no. September, pp. 64–69, 2017, doi: 10.1016/j.cca.2017.10.009.

[17] “Biomarkers and surrogate endpoints: Preferred definitions and conceptual framework,” *Clin. Pharmacol. Ther.*, vol. 69, no. 3, pp. 89–95, Mar. 2001, doi: 10.1067/mcp.2001.113989.

[18] Z. Zhang and D. W. Chan, “The road from discovery to clinical diagnostics: Lessons learned from the first FDA-cleared in vitro diagnostic multivariate index assay of proteomic biomarkers,” *Cancer Epidemiol. Biomarkers Prev.*, vol. 19, no. 12, pp. 2995–2999, 2010, doi: 10.1158/1055-9965.EPI-10-0580.

[19] R. M. Simon, S. Paik, and D. F. Hayes, “Use of archived specimens in evaluation of prognostic and predictive biomarkers,” *J. Natl. Cancer Inst.*, vol. 101, no. 21, pp. 1446–1452, 2009, doi: 10.1093/jnci/djp335.

[20] K. Baryeh, S. Takalkar, M. Lund, and G. Liu, “Development of quantitative immunochromatographic assay for rapid and sensitive detection of carbohydrate antigen 19-9 (CA 19-9) in human plasma,” *J. Pharm. Biomed. Anal.*, vol. 146, pp. 285–291, 2017, doi: 10.1016/j.jpba.2017.09.004.

[21] J. P. Reilly and C. J. White, “Renal Denervation for Resistant Hypertension,” *Prog. Cardiovasc. Dis.*, vol. 59, no. 3, pp. 295–302, 2016, doi: 10.1016/j.pcad.2016.10.003.

[22] M. J. Duffy *et al.*, “Tumor markers in pancreatic cancer: A European Group on Tumor Markers (EGTM) status report,” *Ann. Oncol.*, vol. 21, no. 3, pp. 441–447, 2009, doi: 10.1093/annonc/mdp332.

[23] Z. Wu, A. I. Kuntz, and R. G. Wadleigh, “CA 19-9 Tumor Marker : Is It Reliable ? A Case Report in a Patient With Pancreatic Cancer,” vol. 11, no. 1, pp. 50–55, 2013.

[24] X. G. Ni *et al.*, “The clinical value of serum CEA, CA19-9, and CA242 in the diagnosis and prognosis of pancreatic cancer,” *Eur. J. Surg. Oncol.*, vol. 31, no. 2, pp. 164–169, 2005, doi: 10.1016/j.ejso.2004.09.007.

[25] U. K. Ballehaninna and R. S. Chamberlain, “Serum CA 19-9 as a Biomarker for Pancreatic Cancer-A Comprehensive Review,” *Indian J. Surg. Oncol.*, vol. 2, no. 2, pp. 88–100, 2011, doi: 10.1007/s13193-011-0042-1.

[26] K. A. Mirkin, C. S. Hollenbeak, and J. Wong, “Prognostic impact of carbohydrate antigen 19-9 level at diagnosis in resected stage I-III pancreatic adenocarcinoma: A U.S. population study,” *J. Gastrointest. Oncol.*, vol. 8, no. 5, pp. 778–788, 2017, doi: 10.21037/jgo.2017.07.04.

[27] K. E. Poruk *et al.*, “The Clinical Utility of CA 19-9 in Pancreatic Adenocarcinoma: Diagnostic and Prognostic Updates,” *Curr. Mol. Med.*, vol. 13, no. 3, pp. 340–351, 2013.

[28] C. Chen *et al.*, “Methods for Identifying SNP Interactions : A Review on Variations of Logic Regression, Random Forest and Bayesian Logistic,” *IEEE/ACM Trans. Comput. Biol. Bioinformatics*, vol. 8, no. August 2017, pp. 1580–1591, 2011, doi: 10.1109/TCBB.2011.46.

[29] W. S. Bush and J. H. Moore, “Chapter 11: Genome-Wide Association Studies,” *PLoS Comput. Biol.*, vol. 8, no. 12, pp. 1–11, 2012, doi: 10.1371/journal.pcbi.1002822.

[30] Y. Shen *et al.*, “A SNP discovery method to assess variant allele probability from next-generation resequencing data,” *Genome Res.*, vol. 20, pp. 273–280, 2010, doi: 10.1101/gr.096388.109.

[31] M. Sato, M. Soma, T. Nakayama, and K. Kanmatsuse, “Dopamine D1 receptor gene polymorphism is associated with essential hypertension.,” *Hypertens. (Dallas, Tex. 1979)*, vol. 36, no. 2, pp. 183–186, Aug. 2000.

[32] M. Koptides *et al.*, “Novel NPR1 polymorphic variants and its exclusion as a candidate gene for medullary cystic kidney disease (ADMCKD) type 1,” *Mol. Cell. Probes*, vol. 15, no. 6, pp. 357–361, 2001, doi: https://doi.org/10.1006/mcpr.2001.0381.

[33] T. Nakayama, S. Asai, N. Sato, and M. Soma, “Genotype and haplotype association study of the STRK1 region on 5q12 among Japanese: A case-control study,” *Stroke*, vol. 37, no. 1, pp. 69–76, 2006, doi: 10.1161/01.STR.0000194961.17292.33.

[34] I. Brænne *et al.*, “Genomic correlates of glatiramer acetate adverse cardiovascular effects lead to a novel locus mediating coronary risk,” *PLoS One*, vol. 12, no. 8, pp. 1–19, 2017.

[35] V. Rusu *et al.*, “Type 2 Diabetes Variants Disrupt Function of SLC16A11 through Two Distinct Mechanisms,” *Cell*, vol. 170, no. 1, pp. 199--212.e20, 2017, doi: 10.1016/j.cell.2017.06.011.

[36] B. Maher, “Personal genomes: The case of the missing heritability,” *Nature*, vol. 456, no. 7218, pp. 18–21, 2008, doi: 10.1038/456018a.

[37] T. T. Toma, Z. Williams, J. Dawson, and D. Adjeroh, “What Can One Chromosome Tell us About Human Biogeographical Ancestry?,” in *Proceedijngs of the 2017 IEEE International Conference on Bioinformatics and Biomedicine (BIBM) What*, 2017, pp. 188–193.

[38] J. He and A. Zelikovsky, “Informative SNP selection methods based on SNP prediction,” *IEEE Trans. Nanobioscience*, vol. 6, no. 1, pp. 60–67, 2007, doi: 10.1109/TNB.2007.891901.

[39] P. Y. Kwok and X. Chen, “Detection of single nucleotide polymorphisms,” *Curr. Issues Mol. Biol.*, vol. 5, no. 2, pp. 43–60, 2003, doi: 10.1016/S0076-6879(02)57664-3.

[40] G. Lear *et al.*, “Methods for the extraction, storage, amplification and sequencing of DNA from environmental samples,” *N. Z. J. Ecol.*, vol. 42, 2018, doi: 10.20417/nzjecol.42.9.

[41] J. A. Ludwig and J. N. Weinstein, “Biomarkers in cancer staging, prognosis and treatment selection,” *Nat. Rev. Cancer*, vol. 5, no. 11, pp. 845–856, 2005, doi: 10.1038/nrc1739.

[42] C. Vogel and E. M. Marcotte, “Insights into the regulation of protein abundance from proteomic and transcriptomic analyses,” *Nat. Rev. Genet.*, vol. 13, no. 4, pp. 227–232, 2012, doi: 10.1038/nrg3185.

[43] T. A. Cooper, L. Wan, and G. Dreyfuss, “RNA and Disease,” *Cell*, vol. 136, no. 4, pp. 777–793, 2009, doi: 10.1016/j.cell.2009.02.011.

[44] D. Dixit, Q. Xie, J. N. Rich, and J. C. Zhao, “Messenger RNA Methylation Regulates Glioblastoma Tumorigenesis,” *Cancer Cell*, vol. 31, no. 4, pp. 474–475, 2017, doi: 10.1016/j.ccell.2017.03.010.

[45] Y. Sato and K. Hishida, “Electrokinetic effects on motion of submicron particles in microchannel,” *Fluid Dyn. Res.*, vol. 38, no. 11, pp. 787–802, 2006, doi: 10.1016/j.fluiddyn.2006.04.003.

[46] M. P. Hughes, “AC electrokinetics: Applications for nanotechnology,” *Nanotechnology*, vol. 11, no. 2, pp. 124–132, 2000, doi: 10.1088/0957-4484/11/2/314.

[47] L. Tang, “Fundamentals of Nanotechnology (Hornyak, G.I., et al.) [Book reviews],” *IEEE Nanotechnol. Mag.*, vol. 3, no. 3, pp. 26–27, 2009, doi: 10.1109/mnano.2009.934215.

[48] S.-J. Park and M.-K. Seo, “Chapter 1 - Intermolecular Force,” in *Interface Science and Composites*, vol. 18, S.-J. Park and M.-K. B. T.-I. S. and T. Seo, Eds. Elsevier, 2011, pp. 1–57.

[49] P. R. C. Gascoyne and J. Vykoukal, “Particle separation by dielectrophoresis,” *Electrophoresis*. 2002, doi: 10.1002/1522-2683(200207)23:13<1973::AID-ELPS1973>3.0.CO;2-1.

[50] M. P. Hughes and N. G. Green, “The influence of Stern layer conductance on the dielectrophoretic behavior of latex nanospheres,” *J. Colloid Interface Sci.*, vol. 250, no. 1, pp. 266–268, 2002, doi: 10.1006/jcis.2002.8324.

[51] P. R. C. Gascoyne and S. Shim, “Isolation of circulating tumor cells by dielectrophoresis,” *Cancers (Basel).*, vol. 6, no. 1, pp. 545–579, 2014, doi: 10.3390/cancers6010545.

[52] H. A. Pohl, “The motion and precipitation of suspensoids in divergent electric fields,” *J. Appl. Phys.*, vol. 22, no. 7, pp. 869–871, 1951, doi: 10.1063/1.1700065.

[53] A. Belkin, A. Bezryadin, L. Hendren, and A. Hubler, “Recovery of alumina nanocapacitors after high voltage breakdown,” *Sci. Rep.*, vol. 7, no. 1, pp. 1–8, 2017, doi: 10.1038/s41598-017-01007-9.

[54] E. Thoms, P. Sippel, D. Reuter, M. Weiß, A. Loidl, and S. Krohns, “Dielectric study on mixtures of ionic liquids,” *Sci. Rep.*, vol. 7, no. 1, pp. 1–9, 2017, doi: 10.1038/s41598-017-07982-3.

[55] K. Khoshmanesh, S. Nahavandi, S. Baratchi, A. Mitchell, and K. Kalantar-zadeh, “Dielectrophoretic platforms for bio-microfluidic systems,” *Biosens. Bioelectron.*, vol. 26, no. 5, pp. 1800–1814, 2011, doi: 10.1016/j.bios.2010.09.022.

[56] R. Pethig, “Dielectrophoresis: Status of the theory, technology, and applications,” *Biomicrofluidics*, vol. 4, no. 2, pp. 1–35, 2010, doi: 10.1063/1.3456626.

[57] N. G. Green and H. Nili, “Dielectrophoresis BT - Encyclopedia of Nanotechnology,” B. Bhushan, Ed. Dordrecht: Springer Netherlands, 2012, pp. 534–543.

[58] M. Dimaki and P. Bøggild, “Dielectrophoresis of carbon nanotubes using microelectrodes: A numerical study,” *Nanotechnology*, 2004, doi: 10.1088/0957-4484/15/8/039.

[59] G. Gonga and B. Li, “Dielectric properties of bionanocomposites,” in *Polymer Nanocomposites for Dielectrics*, 2017.

[60] T. Honegger, K. Berton, E. Picard, and D. Peyrade, “Determination of Clausius-Mossotti factors and surface capacitances for colloidal particles,” *Appl. Phys. Lett.*, 2011, doi: 10.1063/1.3583441.

[61] A. T. J. Kadaksham, P. Singh, and N. Aubry, “Dielectrophoresis of nanoparticles,” *Electrophoresis*, 2004, doi: 10.1002/elps.200406092.

[62] C. Zhang, K. Khoshmanesh, A. Mitchell, and K. Kalantar-Zadeh, “Dielectrophoresis for manipulation of micro/nano particles in microfluidic systems,” *Analytical and Bioanalytical Chemistry*. 2010, doi: 10.1007/s00216-009-2922-6.

[63] A. D. Goater and R. Pethig, “Electrorotation and dielectrophoresis.,” *Parasitology*, 1998, doi: 10.1017/S0031182099004114.

[64] H. A. Pohl, “The motion and precipitation of suspensoids in divergent electric fields,” *J. Appl. Phys.*, vol. 22, no. 7, pp. 869–871, 1951, doi: 10.1063/1.1700065.

[65] A. Mortadi, A. El Melouky, E. G. Chahid, R. El Moznine, and O. Cherkaoui, “Studies of the clausius–Mossotti factor,” *J. Phys. Stud.*, 2016.

[66] M. Urdaneta and E. Smela, “Multiple frequency dielectrophoresis,” *Electrophoresis*, 2007, doi: 10.1002/elps.200600786.

[67] Y. J. Lo, Y. Y. Lin, U. Lei, M. S. Wu, and P. C. Yang, “Measurement of the Clausius-Mossotti factor of generalized dielectrophoresis,” *Appl. Phys. Lett.*, 2014, doi: 10.1063/1.4866344.

[68] B. C. Gierhart, D. G. Howitt, S. J. Chen, R. L. Smith, and S. D. Collins, “Frequency dependence of gold nanoparticle superassembly by dielectrophoresis,” *Langmuir*, 2007, doi: 10.1021/la701472y.

[69] P. Ehrlich, “Dielectric properties of teflon from room temperature to 314-degrees-C and from frequencies of 10_2 to 10_5 c/s,” *J. Res. Natl. Bur. Stand. (1934).*, 1953, doi: 10.6028/jres.051.024.

[70] Y. Hwang, H. Sohn, A. Phan, O. M. Yaghi, and R. N. Candler, “Dielectrophoresis-assembled zeolitic imidazolate framework nanoparticle-coupled resonators for highly sensitive and selective gas detection,” *Nano Lett.*, 2013, doi: 10.1021/nl4027692.

[71] E. Salimi, K. Braasch, M. Butler, D. J. Thomson, and G. E. Bridges, “Dielectric model for Chinese hamster ovary cells obtained by dielectrophoresis cytometry,” *Biomicrofluidics*, 2016, doi: 10.1063/1.4940432.

[72] C. F. Chou *et al.*, “Electrodeless dielectrophoresis of single- and double-stranded DNA,” *Biophys. J.*, 2002, doi: 10.1016/S0006-3495(02)73977-5.

[73] L. Cui, D. Holmes, and H. Morgan, “The dielectrophoretic levitation and separation of latex beads in microchips,” *Electrophoresis*, vol. 22, no. 18, pp. 3893–3901, 2001, doi: 10.1002/1522-2683(200110)22:18<3893::AID-ELPS3893>3.0.CO;2-2.

[74] R. Pethig, “Publisher’s Note: ‘Review Article—Dielectrophoresis: Status of the theory, technology, and applications’ [Biomicrofluidics 4, 022811 (2010)],” *Biomicrofluidics*, 2010, doi: 10.1063/1.3474458.

[75] N. Abd Rahman, F. Ibrahim, and B. Yafouz, “Dielectrophoresis for Biomedical Sciences Applications: A Review,” *Sensors (Basel).*, vol. 17, no. 3, p. 449, Mar. 2017, doi: 10.3390/s17030449.

[76] Y. Qiang, J. Liu, and E. Du, “Dielectrophoresis Testing of Nonlinear Viscoelastic Behaviors of Human Red Blood Cells,” *Micromachines* , vol. 9, no. 1. 2018, doi: 10.3390/mi9010021.

[77] I. H. Su *et al.*, “Dielectrophoresis System for Testing Antimicrobial Susceptibility of Gram-Negative Bacteria to β-Lactam Antibiotics,” *Anal. Chem.*, vol. 89, no. 8, pp. 4635–4641, 2017, doi: 10.1021/acs.analchem.7b00220.

[78] E. O. Adekanmbi, M. W. Ueti, B. Rinaldi, C. E. Suarez, and S. K. Srivastava, “Insulator-based dielectrophoretic diagnostic tool for babesiosis,” *Biomicrofluidics*, vol. 10, no. 3, pp. 1–12, 2016, doi: 10.1063/1.4954196.

[79] E. S. Elvington, A. Salmanzadeh, M. A. Stremler, and R. V. Davalos, “Label-free isolation and enrichment of cells through contactless dielectrophoresis,” *J. Vis. Exp.*, no. 79, pp. 1–10, 2013, doi: 10.3791/50634.

[80] A. LaLonde, M. F. Romero-Creel, M. A. Saucedo-Espinosa, and B. H. Lapizco-Encinas, “Isolation and enrichment of low abundant particles with insulator-based dielectrophoresis,” *Biomicrofluidics*, vol. 9, no. 6, pp. 1–13, 2015, doi: 10.1063/1.4936371.

[81] P. S. Williams, L. R. Moore, P. Joshi, M. Goodin, M. Zborowski, and A. Fleischman, "Microfluidic chip for graduated magnetic separation of circulating tumor cells by their epithelial cell adhesion molecule expression and magnetic nanoparticle binding," *J. Chromatogr. A*, vol. 1637, p. 461823, 2021, doi: https://doi.org/10.1016/j.chroma.2020.461823.

[82] N. Zhu, B. Zhang, and Q. Yu, "Genetic Engineering-Facilitated Coassembly of Synthetic Bacterial Cells and Magnetic Nanoparticles for Efficient Heavy Metal Removal," *ACS Appl. Mater. Interfaces*, vol. 12, no. 20, pp. 22948–22957, May 2020, doi: 10.1021/acsami.0c04512.

[83] Z. Lin *et al.*, "Rapid Assessment of Surface Markers on Cancer Cells Using Immuno-Magnetic Separation and Multi-frequency Impedance Cytometry for Targeted Therapy," *Sci. Rep.*, vol. 10, no. 1, p. 3015, 2020, doi: 10.1038/s41598-020-57540-7.

[84] B. D. Plouffe, S. K. Murthy, and L. H. Lewis, "Fundamentals and application of magnetic particles in cell isolation and enrichment: a review," *Rep. Prog. Phys.*, vol. 78, no. 1, p. 16601, Jan. 2015, doi: 10.1088/0034-4885/78/1/016601.

[85] Y. Yasukochi *et al.*, "Two novel susceptibility loci for type 2 diabetes mellitus identified by longitudinal exome-wide association studies in a Japanese population," *Genomics*, vol. 111, no. 1, pp. 34–42, 2019, doi: 10.1016/j.ygeno.2017.12.010.

[86] J. Roy and B. Mallick, "Altered gene expression in late-onset Alzheimer's disease due to SNPs within 3′UTR microRNA response elements," *Genomics*, vol. 109, no. 3–4, pp. 177–185, 2017, doi: 10.1016/j.ygeno.2017.02.006.

[87] T. LaFramboise, “Single nucleotide polymorphism arrays: A decade of biological, computational and technological advances,” *Nucleic Acids Res.*, vol. 37, no. 13, pp. 4181–4193, 2009, doi: 10.1093/nar/gkp552.

[88] A. K. Talukder, S. Gandham, H. A. Prahalad, and N. P. Bhattacharyya, “Cloud-MAQ: The Cloud-enabled Scalable Whole Genome Reference Assembly Application,” *2010 7th Int. Conf. Wirel. Opt. Commun. Networks, WOCN2010*, pp. 0–4, 2010, doi: 10.1109/WOCN.2010.5587308.

[89] R. Li *et al.*, “SNP detection for massively parallel whole-genome resequencing.-ppt,” *Genome Res.*, vol. 19, no. 6, pp. 1124–32, 2009, doi: 10.1101/gr.088013.108.

[90] Y. H. Cheng, C. N. Kuo, and C. M. Lai, “Effective natural PCR-RFLP primer design for SNP genotyping using teaching-learning-based optimization with elite strategy,” *IEEE Trans. Nanobioscience*, vol. 15, no. 7, pp. 657–665, 2016, doi: 10.1109/TNB.2016.2597867.

[91] J. G. Hall *et al.*, “Sensitive detection of DNA polymorphisms by the serial invasive signal amplification reaction.,” *Proc. Natl. Acad. Sci. U. S. A.*, vol. 97, no. 15, pp. 8272–8277, Jul. 2000, doi: 10.1073/pnas.140225597.

[92] D. Schmalzing *et al.*, “Microchip electrophoresis: a method for high-speed SNP detection.,” *Nucleic Acids Res.*, vol. 28, no. 9, p. E43, May 2000, doi: 10.1093/nar/28.9.e43.

[93] P. Ross, L. Hall, I. Smirnov, and L. Haff, “High level multiplex genotyping by MALDI-TOF mass spectrometry.,” *Nat. Biotechnol.*, vol. 16, no. 13, p. 1347,1351, [Online]. Available: http://search.proquest.com/docview/70114951/.

[94] U. Landegren, R. Kaiser, J. Sanders, and L. Hood, “A ligase-mediated gene detection technique.,” *Science*, vol. 241, no. 4869, p. 1077,1080, [Online]. Available: http://search.proquest.com/docview/78398475/.

[95] D. Y. Wu and R. B. Wallace, “The ligation amplification reaction (LAR)—Amplification of specific DNA sequences using sequential rounds of template-dependent ligation,” *Genomics*, vol. 4, no. 4, pp. 560–569, May 1989, doi: 10.1016/0888-7543(89)90280-2.

[96] V. O. Tobe, S. L. Taylor, and D. A. Nickerson, “Single-well genotyping of diallelic sequence variations by a two-color ELISA-based oligonucleotide ligation assay.,” *Nucleic Acids Res.*, vol. 24, no. 19, pp. 3728–3732, Oct. 1996, doi: 10.1093/nar/24.19.3728.

[97] Y. S. Huh, A. J. Lowe, A. D. Strickland, C. A. Batt, and D. Erickson, “Surface-enhanced Raman scattering based ligase detection reaction.,” *J. Am. Chem. Soc.*, vol. 131, no. 6, pp. 2208–2213, Feb. 2009, doi: 10.1021/ja807526v.

[98] Y. Xu, N. B. Karalkar, and E. T. Kool, “Nonenzymatic autoligation in direct three-color detection of RNA and DNA point mutations,” *Nat. Biotechnol.*, vol. 19, no. 2, pp. 148–152, 2001, doi: 10.1038/84414.

[99] S. Sando, H. Abe, and E. T. Kool, “Quenched Auto-Ligating DNAs: Multicolor Identification of Nucleic Acids at Single Nucleotide Resolution,” *J. Am. Chem. Soc.*, vol. 126, no. 4, pp. 1081–1087, Feb. 2004, doi: 10.1021/ja038665z.

[100] N. M. GREEN, “Avidin. 3. the Nature of the Biotin-Binding Site.,” *Biochem. J.*, vol. 89, pp. 599–609, 1963, doi: 10.1042/bj0890599.

[101] W. C. Mundy, J. A. Roux, and A. M. Smith, “Mie scattering by spheres in an absorbing medium*,” *J. Opt. Soc. Am.*, vol. 64, no. 12, pp. 1593–1597, 1974, doi: 10.1364/JOSA.64.001593.

[102] S. A. M. Kirmani, F. D. Gudagunti, L. Velmanickam, D. Nawarathna, and I. T. Lima, "Negative dielectrophoresis spectroscopy for rare analyte quantification in biological samples," *J. Biomed. Opt.*, vol. 22, no. 3, 2017, doi: 10.1117/1.JBO.22.3.037006.

[103] T. Muniraj, P. A. Jamidar, and H. R. Aslanian, "Pancreatic cancer: A comprehensive review and update," *Disease-a-Month*, vol. 59, no. 11, pp. 368–402, 2013, doi: 10.1016/j.disamonth.2013.08.001.

[104] B. C. Del Villano *et al.*, "Radioimmunometric assay for a monoclonal antibody-defined tumor marker, CA 19-9," *Clin. Chem.*, vol. 29, no. 3, pp. 549–552, 1983.

[105] J. C. Chang and M. Kundranda, "Novel Diagnostic and Predictive Biomarkers in Pancreatic Adenocarcinoma," *Int. J. Mol. Sci.*, vol. 18, no. 3, p. 667, Mar. 2017, doi: 10.3390/ijms18030667.

[106] M. Distler, E. Pilarsky, S. Kersting, and R. Grützmann, "Preoperative CEA and CA 19-9 are prognostic markers for survival after curative resection for ductal adenocarcinoma of the pancreas – A retrospective tumor marker prognostic study," *Int. J. Surg.*, vol. 11, no. 10, pp. 1067–1072, Feb. 2018, doi: 10.1016/j.ijsu.2013.10.005.

[107] W. Steinberg, "The Clinical Utility of the CA 19-9 Tumor-Associated Antigen," *Am. J. Gastroenterol.*, vol. 85, no. 4, pp. 350–355, 1990, doi: 0002-9270/90/8504-0350.

[108] R. Passerini *et al.*, "The pitfalls of CA19-9: Routine testing and comparison of two automated immunoassays in a reference oncology center," *Am. J. Clin. Pathol.*, vol. 138, no. 2, pp. 281–287, 2012, doi: 10.1309/AJCPOPNPLLCYR07H.

[109] Y. Yang, M. Ozsoz, and G. Liu, "Gold nanocage-based lateral flow immunoassay for immunoglobulin G," *Mikrochim. Acta*, vol. 184, no. 7, pp. 2023–2029, Jul. 2017, doi: 10.1007/s00604-017-2176-5.

[110] T. Wu *et al.*, “Label-free photoelectrochemical immunosensor for carcinoembryonic antigen detection based on g-C3N4 nanosheets hybridized with Zn0.1Cd0.9S nanocrystals,” *Sensors Actuators B Chem.*, vol. 256, pp. 812–819, 2018, doi: https://doi.org/10.1016/j.snb.2017.10.023.

[111] J. W. Chung, R. Bernhardt, and J. C. Pyun, “Additive assay of cancer marker CA 19-9 by SPR biosensor,” *Sensors Actuators, B Chem.*, vol. 118, no. 1–2, pp. 28–32, 2006, doi: 10.1016/j.snb.2006.04.015.

[112] I. T. Lima Jr., D. Nawarathna, F. D. Gudagunti, and L. Velmanickam, “Method for Detecting and Quantifying Biological Molecules using Dielectrophoresis,” *Provisional US Patent, Ser. No 62/622,508*, 2018.

[113] K. Khoshmanesh, S. Nahavandi, S. Baratchi, A. Mitchell, and K. Kalantar-zadeh, “Dielectrophoretic platforms for bio-microfluidic systems,” *Biosens. Bioelectron.*, vol. 26, no. 5, pp. 1800–1814, 2011, doi: 10.1016/j.bios.2010.09.022.

[114] T. Kawabata and M. Washizu, “Dielectrophoretic detection of molecular bindings,” *IEEE Trans. Ind. Appl.*, vol. 37, no. 6, pp. 1625–1633, 2001, doi: 10.1109/28.968170.

[115] J. Ramón-Azcón, T. Yasukawa, and F. Mizutani, “Sensitive and spatially multiplexed detection system based on dielectrophoretic manipulation of DNA-encoded particles used as immunoreactions platform,” *Anal. Chem.*, vol. 83, no. 3, p. 1053, 2011, doi: 10.1021/ac102854z.

[116] M. Viefhues, J. Regtmeier, and D. Anselmetti, “Fast and continuous-flow separation of DNA-complexes and topological DNA variants in microfluidic chip format,” *Analyst*, vol. 138, no. 1, pp. 186–196, 2012, doi: 10.1039/c2an36056j.

[117] L. Velmanickam, D. Laudenbach, and D. Nawarathna, “Dielectrophoretic label-free immunoassay for rare-analyte quantification in biological samples,” *Phys. Rev. E - Stat. Nonlinear, Soft Matter Phys.*, vol. 94, no. 4, pp. 1–6, 2016, doi: 10.1103/PhysRevE.94.042408.

[118] R. Pethig and S. Smith, *Introductory Bioelectronics for Engineers and Physical Scientists*. West Sussex: Willey, 2013.

[119] F. Asad-Ur-Rahman and M. W. Saif, “Elevated Level of Serum Carcinoembryonic Antigen (CEA) and Search for a Malignancy: A Case Report,” *Cureus*, vol. 8, no. 6, pp. 8–11, 2016, doi: 10.7759/cureus.648.

[120] F. Asad-Ur-Rahman *et al.*, “Serum CA 19-9 and CEA levels as a prognostic factor in pancreatic adenocarcinoma,” *Cureus*, vol. 8, no. 6, pp. 643–649, 2016, doi: 10.3349/ymj.2013.54.3.643.

[121] T. B. Jones, “Basic Theory of Dielectrophoresis and Electrorotation,” *IEEE Eng. Med. Biol. Mag.*, vol. 22, no. 6, pp. 33–42, 2003, doi: 10.1109/MEMB.2003.1304999.

[122] Y. Zhang, J. Yang, H. Li, Y. Wu, H. Zhang, and W. Chen, “Tumor markers CA19-9, CA242 and CEA in the diagnosis of pancreatic cancer: A meta-analysis,” *Int. J. Clin. Exp. Med.*, vol. 8, no. 7, pp. 11683–11691, 2015.

[123] C. Haglund, J. Lundin, P. Kuusela, and P. J. Roberts, “CA 242, a new tumour marker for pancreatic cancer: A comparison with CA 19-9, CA 50 and CEA,” *Br. J. Cancer*, vol. 70, no. 3, pp. 487–492, 1994, doi: 10.1038/bjc.1994.332.

[124] C. Vogel and E. M. Marcotte, “Insights into the regulation of protein abundance from proteomic and transcriptomic analyses,” *Nat. Rev. Genet.*, vol. 13, no. 4, pp. 227–232, 2012, doi: 10.1038/nrg3185.

[125] D. Dixit, Q. Xie, J. N. Rich, and J. C. Zhao, “Messenger RNA Methylation Regulates Glioblastoma Tumorigenesis,” *Cancer Cell*, vol. 31, no. 4, pp. 474–475, 2017, doi: 10.1016/j.ccell.2017.03.010.

[126] V. Rusu *et al.*, “Type 2 Diabetes Variants Disrupt Function of SLC16A11 through Two Distinct Mechanisms,” *Cell*, vol. 170, no. 1, pp. 199-212.e20, 2017, doi: 10.1016/j.cell.2017.06.011.

[127] N. Miura *et al.*, “Clinical usefulness of serum telomerase reverse transcriptase (hTERT) mRNA and epidermal growth factor receptor (EGFR) mRNA as a novel tumor marker for lung cancer,” *Cancer Sci.*, vol. 97, no. 12, pp. 1366–1373, 2006, doi: 10.1111/j.1349-7006.2006.00342.x.

[128] K. Kasem, V. Gopalan, A. Salajegheh, C. T. Lu, R. A. Smith, and A. K. Y. Lam, “The roles of JK-1 (FAM134B) expressions in colorectal cancer,” *Exp. Cell Res.*, vol. 326, no. 1, pp. 166–173, 2014, doi: 10.1016/j.yexcr.2014.06.013.

[129] S. Mehta *et al.*, “Predictive and prognostic molecular markers for cancer medicine,” *Ther. Adv. Med. Oncol.*, vol. 2, no. 2, pp. 125–148, 2010, doi: 10.1177/1758834009360519.

[130] S. Volinia and C. M. Croce, “Prognostic microRNA/mRNA signature from the integrated analysis of patients with invasive breast cancer,” *Proc. Natl. Acad. Sci. U. S. A.*, vol. 110, no. 18, pp. 7413–7417, 2013, doi: 10.1073/pnas.1304977110.

[131] N. A. Fonseca, J. Marioni, and A. Brazma, “RNA-Seq gene profiling - A systematic empirical comparison,” *PLoS One*, vol. 9, no. 9, 2014, doi: 10.1371/journal.pone.0107026.

[132] F. Finotello and B. Di Camillo, “Measuring differential gene expression with RNA-seq: challenges and strategies for data analysis.,” *Brief. Funct. Genomics*, vol. 14, no. 2, pp. 130–42, 2015, doi: 10.1093/bfgp/elu035.

[133] G. Chen, T. Shi, and L. Shi, “Characterizing and annotating the genome using RNA-seq data,” *Sci. China Life Sci.*, vol. 60, no. 2, pp. 116–125, 2017, doi: 10.1007/s11427-015-0349-4.

[134] A. Metsis *et al.*, “Whole-genome expression profiling through fragment display and combinatorial gene identification.,” *Nucleic Acids Res.*, vol. 32, no. 16, 2004, doi: 10.1093/nar/gnh126.

[135] S. Narrandes and W. Xu, “Gene expression detection assay for cancer clinical use,” *J. Cancer*, vol. 9, no. 13, pp. 2249–2265, 2018, doi: 10.7150/jca.24744.

[136] Z. Wang and B. Sun, “Annular multiphase flow behavior during deep water drilling and the effect of hydrate phase transition,” *Pet. Sci.*, vol. 6, no. 1, pp. 57–63, 2009, doi: 10.1007/s12182-009-0010-3.

[137] W. Etienne, M. H. Meyer, J. Peppers, and R. A. Meyer, “Comparison of mRNA gene expression by RT-PCR and DNA microarray,” *Biotechniques*, vol. 36, no. 4, pp. 618–626, 2004.

[138] M. Haider, T. Haselgrübler, A. Sonnleitner, F. Aberger, and J. Hesse, “A Double-Hybridization Approach for the Transcription- and Amplification-Free Detection of Specific mRNA on a Microarray,” *Microarrays*, vol. 5, no. 1, p. 5, 2016, doi: 10.3390/microarrays5010005.

[139] K. M. Koo, L. G. Carrascosa, M. J. A. Shiddiky, and M. Trau, “Poly(A) Extensions of miRNAs for Amplification-Free Electrochemical Detection on Screen-Printed Gold

Electrodes," *Anal. Chem.*, vol. 88, no. 4, pp. 2000–2005, 2016, doi: 10.1021/acs.analchem.5b04795.

[140] C. Pöhlmann and M. Sprinzl, "Electrochemical detection of micrornas via gap hybridization assay," *Anal. Chem.*, vol. 82, no. 11, pp. 4434–4440, 2010, doi: 10.1021/ac100186p.

[141] K. Mukumoto, T. Nojima, S. Sato, M. Waki, and S. Takenaka, "Direct modification of mRNA by ferrocenyl carbodiimide and its application to electrochemical detection of mRNA," *Anal. Sci.*, vol. 23, no. 1, pp. 115–119, 2007, doi: 10.2116/analsci.23.115.

[142] X. Mao *et al.*, "Ultrasensitive electrochemical detection of mRNA using branched DNA amplifiers," *Electrochem. commun.*, vol. 10, no. 12, pp. 1847–1850, 2008, doi: 10.1016/j.elecom.2008.09.028.

[143] S. Sato, S. Fujii, K. Yamashita, M. Takagi, H. Kondo, and S. Takenaka, "Ferrocenyl naphthalene diimide can bind to DNA·RNA hetero duplex: Potential use in an electrochemical detection of mRNA expression," *J. Organomet. Chem.*, vol. 637–639, pp. 476–483, 2001, doi: 10.1016/S0022-328X(01)00951-2.

[144] E. Vasilyeva, B. Lam, Z. Fang, M. D. Minden, E. H. Sargent, and S. O. Kelley, "Direct genetic analysis of ten cancer cells: Tuning sensor structure and molecular probe design for efficient mRNA capture," *Angew. Chemie - Int. Ed.*, vol. 50, no. 18, pp. 4137–4141, 2011, doi: 10.1002/anie.201006793.

[145] F. Dackson Gudagunti, L. Velmanickam, D. Nawarathna, and I. Lima, "Label-Free Biosensing Method for the Detection of a Pancreatic Cancer Biomarker Based on Dielectrophoresis Spectroscopy," *Chemosensors*, vol. 6, no. 33, pp. 1–10, 2018, doi: 10.3390/chemosensors6030033.

[146] S. A. M. Kirmani, F. D. Gudagunti, L. Velmanickam, D. Nawarathna, and I. T. Lima Jr., "Negative dielectrophoresis spectroscopy for rare analyte quantification in biological samples," *J. Biomed. Opt.*, vol. 22, no. 3, pp. 037006–1 to 7, 2017, doi: 10.1117/1.JBO.22.3.037006.

[147] S. C. Kogan, M. Doherty, and J. Gitschier, "An improved method for prenatal diagnosis of genetic diseases by analysis of amplified DNA sequences: Application to hemophilia A," *Obstetrical and Gynecological Survey*, vol. 43, no. 4. pp. 236–238, 1988, doi: 10.1097/00006254-198804000-00016.

[148] F. D. Gudagunti, L. Velmanickam, D. Nawarathna, and I. T. Lima, "Nucleotide identification in DNA using dielectrophoresis spectroscopy," *Micromachines*, vol. 11, no. 1, 2020, doi: 10.3390/mi11010039.

[149] F. D. Gudagunti, L. Velmanickam, D. Nawarathna, and I. T. Lima, "Detection of nucleotide polymorphisms using dielectrophoresis," 2019, doi: 10.1109/RAPID.2019.8864400.

[150] F. D. Gudagunti, L. Velmanickam, D. Nawarathna, and I. T. Lima Jr, "Label-Free DNA Identification Using Light Scattering from Microbeads and Dielectrophoresis Spectroscopy," in *IEEE Photonics Conference*, 2017, pp. 1–2.

[151] F. D. Gudagunti, V. Jayasooriya, S. Afrose, D. Nawarathna, and I. T. Lima, "Biosensor for the characterization of gene expression in cells," *Chemosensors*, vol. 7, no. 4, 2019, doi: 10.3390/chemosensors7040060.

[152] F. D. Gudagunti, V. Jayasooriya, D. Nawarathna, and I. T. Lima, "Image processing method for rapid messenger RNA profiling from living cells," 2019, doi: 10.1109/RAPID.2019.8864307.